

Neutrino Oscillations in Long Baseline Experiments

Adam Lister

A dissertation presented for the degree of
Master of Science



Centre for Particle Theory
Department of Mathematical Sciences
University of Durham
England
September 2014

Neutrino Oscillations in Long Baseline Experiments

Adam Lister

Submitted for the degree of Master of Science
September 2014

Abstract

Neutrino oscillations are now well documented with an impressive amount of literature on the topic. Oscillation experiments have an important place at the forefront of high energy physics, with opportunities for both precision studies of the Standard Model and to discover new physics, allowing us to further explore our understanding of the universe. This dissertation provides the mathematical framework of neutrino oscillations, both in vacuum and in matter, for the unphysical 2ν case and the realistic 3ν case. Precision studies of the future Long Baseline Neutrino Experiment are carried out using the GLoBES simulation software, with particular attention paid to resolving the three big questions in oscillation physics: what is the true mass hierarchy? Is CP violated in the leptonic sector? What is the octant of the θ_{23} mixing angle? These simulations demonstrate the ability of LBNE to break the eight-fold degeneracy that plagues neutrino oscillation physics, and therefore constrain the parameters associated with oscillations.

Declaration

The work in this dissertation is based on research carried out at the Centre for Particle Theory, the Department of Mathematical Sciences, England. No part of this dissertation has been submitted elsewhere for any other degree or qualification and it is all my own work unless referenced to the contrary in the text.

Copyright © 2014 by Adam Lister.

“The copyright of this dissertation rests with the author. No quotations from it should be published without the author’s prior written consent and information derived from it should be acknowledged”.

Contents

Abstract	ii
Declaration	iii
1 Introduction	1
1.1 A Brief History of Neutrinos	1
1.2 The Standard Model Neutrino	2
1.3 Neutrinos beyond the Standard Model	4
1.4 Outline of this Dissertation	6
2 Neutrino Oscillations	9
2.1 Theory of Oscillations	9
2.1.1 The Standard Derivation of Neutrino Oscillations Using the Plane Wave Approximation	9
2.1.2 Quantum Field Theory of Flavour States in the Plane-Wave Approximation	13
2.1.3 Wave-Packet treatment	15
2.1.4 CP, T and CPT transformations	19
2.2 Vacuum Oscillations	20
2.2.1 2- ν Oscillations in Vacuum	21
2.2.2 3- ν Oscillations in Vacuum	21
Varying δ_{CP}	23
Varying the mass-squared differences	24
Varying the mixing angles	25
2.3 Matter Effects in ν Oscillations	27
2.3.1 Derivation of the Matter Potential	28
2.3.2 2- ν Oscillations in Matter	31
2.3.3 3- ν Oscillations in Matter	34
Matter Effects in the Determination of δ_{CP}	39

Varying the Matter Potential	41
2.4 Degeneracies	42
2.4.1 Hierarchy Degeneracy	43
2.4.2 Intrinsic Degeneracy	44
2.4.3 Octant Degeneracy	45
3 Oscillation Experiments	47
3.1 Experiments	48
3.1.1 Solar and Atmospheric Experiments	48
3.1.2 Short Baseline Experiments	49
3.1.3 Long Baseline Experiments	49
3.1.4 Neutrino Factories	50
3.1.5 SuperBeams	51
3.1.6 Beta-Beams	51
3.2 Current Oscillation Parameters	52
4 Statistical Overview	53
4.1 Likelihoods, Bins and Priors	53
4.2 Mass Hierarchy Statistics	55
4.2.1 Simple Frequentist Hypothesis Testing	55
4.2.2 Application to the Neutrino Mass Hierarchy	56
4.3 CP Violation Statistics	57
4.4 θ_{23} Octant Statistics	58
5 Precision study of LBNE	59
5.1 LBNE Experimental Setup	59
5.1.1 Initial Setup	60
5.1.2 Final Setup	61
5.2 Study of Oscillation Probabilities	62
5.3 LBNE Simulation Event Numbers	63
5.4 Study of LBNE	65
5.4.1 Allowed Regions	68
5.4.2 Study of the Mass Hierarchy	69
5.4.3 Study of δ_{CP}	73
5.4.4 Study of the Octant of θ_{23}	79
6 Summary and Conclusions	83
Appendices	85

A Finite Normalisation Volume Method	85
B Probability Calculations	87
B.1 One Mass-Squared Dominance	87
B.2 Asano-Minakata Probability	88
B.2.1 Example Calculation of an S-Matrix Element	91
C GLoBES Statistics	95

List of Figures

1.1	CC and NC interaction channels	4
2.1	Oscillation probability - baseline plot for 2ν in vacuum	22
2.2	$\nu_e \rightarrow \nu_\mu$ transition plots for $\delta_{CP} = 0, \frac{\pi}{2}, \pi, \frac{3\pi}{2}$	24
2.3	$\nu_e \rightarrow \nu_\mu$ transition probabilities with variable Δm_{21}^2	25
2.4	$\nu_e \rightarrow \nu_\mu$ transition probabilities with variable Δm_{31}^2	25
2.5	$\nu_e \rightarrow \nu_\mu$ transition probabilities with variable θ_{12}	26
2.6	$\nu_e \rightarrow \nu_\mu$ transition probabilities with variable θ_{13}	26
2.7	$\nu_e \rightarrow \nu_\mu$ transition probabilities with variable θ_{23}	27
2.8	Oscillation probability - baseline plot for 2ν in matter	34
2.9	Comparison of the Cervera et al. probability and the Asano-Minakata probability against the true probability	40
2.10	CP asymmetry in L-E plane for vacuum and in matter.	41
2.11	Oscillation probability - Matter potential plot for $\delta_{CP} = 0, \frac{\pi}{2}, \pi, \frac{3\pi}{2}$	42
2.12	Energy eigenvalues against the matter potential	43
2.13	Contour plots for the 3ν case in the $L - V_{cc}$ and $E - V_{cc}$ planes	43
2.14	Graphical representation of NH and IH	44
4.1	Gaussian probability distribution	56
5.1	3ν transition probabilities for the three channels	62
5.2	ν oscillation probability plots in the normal/inverted hierarchies for $\delta_{CP} = 0, \frac{\pi}{2}, \pi, \frac{3\pi}{2}$	63
5.3	ν oscillation probability plots in the normal/inverted hierarchies for $\delta_{CP} = 0, \frac{\pi}{2}, \pi, \frac{3\pi}{2}$	63
5.4	E-L and CP asymmetry contour plots for LBNE	64
5.5	χ^2 plots for the oscillation parameters with no priors	66
5.6	χ^2 plots for the oscillation parameters with 1σ priors	67
5.7	Allowed regions in the $\delta_{CP} - \sin^2(\theta_{13})$ plane	70
5.8	Allowed regions in the $\delta_{CP} - \sin^2(\theta_{23})$ plane	71

5.9	Sensitivity to the mass hierarchy in the (a) normal and (b) inverted hierarchies. Here the lower octant of θ_{23} has been assumed. The top band represents sensitivities achieved for the 35 kt setup, whilst the bottom band represents sensitivities for the 10 kt setup. The width of each band represents reduction in error and improvements to the beamline. This simulation assumes 3 + 3 years of running for $\nu/\bar{\nu}$	72
5.10	MH sensitivity for LBNE initial setup with largest uncertainties, for varying values of θ_{23}	72
5.11	MH sensitivity dependence upon knowledge of θ_{13} . All priors are included in this plot.	73
5.12	Plot of the $\Delta\chi^2_{CPV}$ test statistic as defined in equation 5.2, for the LBNE initial setup (1.2 MW, 80 GeV neutrino beam incident upon a 10 kt detector for 6 years), for the normal (a) and inverted (b) hierarchy.	74
5.13	The test statistic of equation 5.2 for varying fractions of $\nu/\bar{\nu}$. These plots are calculated for the LBNE initial setup using oscillation parameters in the normal hierarchy. The percentages denote how much time of the 6 years are spent running neutrinos or antineutrinos.	75
5.14	The test statistic of equation 5.2 for varying fractions of $\nu/\bar{\nu}$. Plots are calculated for the LBNE initial setup using oscillation parameters in the inverted hierarchy.	76
5.15	Variation in the sensitivity of LBNE to differing values of θ_{13} . Normal hierarchy is assumed, and priors on the other parameters are taken to be their 1σ values.	76
5.16	The χ^2_{CPV} test statistic for varying values of θ_{23} which are assumed to be known to infinite precision, allowing 1σ priors for all other parameters. Normal hierarchy is assumed.	77
5.17	Sensitivity of LBNE to δ_{CP} . The blue band represents the sensitivities LBNE is capable of with a 10 kt detector, and the grey band represents the sensitivities with a 35 kt detector. The widths of the bands represent variation in the beamline setup and varying amounts of error on the signal and background normalisations. These simulations assume that no near detector is used, and that neutrinos and anti-neutrinos are each ran for 3 years.	78
5.18	The same setup as figure 5.17, but with 5 year running times for $\nu/\bar{\nu}$. . .	79
5.19	A typical study of octant determination with no priors. The significance for each θ_{23}^{true} determines to what significance the wrong hierarchy can be ruled out. This simulation is performed with systematics only.	80

5.20	The effect of knowledge of θ_{13} on the determination of the octant of θ_{23} . No priors are used other than those placed upon θ_{13} .	81
5.21	Sensitivities for octant sensitivity in (a) the normal hierarchy and (b) the inverted hierarchy. Each band represents variation in the beamline design and signal and background normalisation errors. The top band is for the 35 kt detector and the bottom band is for the initial 10 kt detector.	81
C.1	Plots showing number of events against binned energy data for the true parameters (a) and hypothesised parameters with a different value of δ_{CP} (b).	96
C.2	χ^2 distribution for $\delta_{CP}^{True} = \frac{\pi}{2}$ for both a Neyman's χ^2 , labelled as "without systematic uncertainties", and the full $\Delta\chi^2$. As can be seen, a 3σ allowed region for delta can be constructed between $\delta_{CP} \approx 78^\circ$ and $\delta_{CP} \approx 100^\circ$.	97

List of Tables

1.1	Fundamental fermions contained in the SM	5
3.1	Current oscillation parameters	52
5.1	Initial LBNE reference values	61
5.2	Final LBNE reference values	61
5.3	Number of events for the $\nu_\mu \rightarrow \nu_e$ transition.	64
5.4	Number of events for the $\bar{\nu}_\mu \rightarrow \bar{\nu}_e$ transition.	65

Chapter 1

Introduction

Neutrino particle physics is a vibrant area of research with far reaching consequences in many areas of physics including particle physics, nuclear physics, cosmology, and astrophysics. Within the Standard Model of particle physics (SM) — developed in the 1970s — neutrinos are assumed to be massless as right handed neutrinos (ν_R) are not included. However, this was shown to be inaccurate when evidence published in the late 1990s showed that neutrinos change *flavour* (ν_e , ν_μ , ν_τ), implying that neutrinos have mass on the scale of eVs and mix. Although dark matter has been hinted at, it has not been experimentally verified, and so flavour oscillations are considered to be the first evidence of physics beyond the Standard Model (BSM). For the case in which there are three flavours of neutrino, neutrino oscillations can be characterised by three mixing angles (θ_{12} , θ_{13} , θ_{23}), two mass-squared differences (Δm_{12}^2 and Δm_{13}^2) and a CP violating phase (δ_{CP}). The aim of neutrino oscillation experiments is to constrain these values in order gain a fuller understanding of the underlying theory. Results from Daya Bay in 2013 confirmed to 5σ that θ_{13} is non-zero meaning that all of the mixing angles, along with the mass-squared differences, have now been measured with precision. The remaining unknown parameters are the mass hierarchy (the sign of Δm_{13}), the octant of θ_{23} , and the value of δ_{CP} . Should it be found that $\delta_{CP} \neq 0, \pi$, then this would be evidence for charge-parity violation in the leptonic sector, which may be associated with the baryon asymmetry of the universe.

1.1 A Brief History of Neutrinos

β decay experiments performed in the years prior to 1930 found that electrons were emitted with a continuous velocity distribution rather than a discreet value as had previously been predicted. That β decays appeared to violate the principle of energy conservation — a historically important conservation law — naturally generated a huge amount of inter-

est and inspired a wealth of proposals on how to formulate a theory of β decay in which this could be avoided. Apologetically, Wolfgang Pauli proposed something which he considered to be impossible to experimentally verify — a neutrally charged, spin-half particle with a mass satisfactorily small such that experiments of the time could not have detected them [1]. This was not considered seriously until Enrico Fermi published his theory of β decay, unifying Pauli’s neutrino and Dirac’s positron in to a single theory [2]. Being apparently unverifiable did not deter experimental physicists from attempting to detect the neutrino, even when an analysis of the neutrino cross section by Bethe and Peierls suggested that it would have been almost undetectable using current technology [3]. Fortunately, the advent of nuclear fission in the following decades provided an intense source of anti-neutrinos, which allowed Reines and Cowan to exploit the $\bar{\nu} + p^+ \rightarrow n^0 + e^+$ [4] reaction in their experiments. By searching for a characteristic delay between the detection of gamma rays¹ they were able to distinguish the signal from the background and provide experimental evidence for the neutrino.

During the following decades, another flavour of neutrino was detected, distinct from the previously discovered neutrino due to it’s part in interactions involving muons rather than electrons. To distinguish between the two flavours of neutrino, this was termed the μ -neutrino (ν_μ), and the neutrino from the Reines-Cowan experiment was relabelled as the electron-neutrino (ν_e). The final Standard Model neutrino, the τ -neutrino (ν_τ), was implied by the existence of the τ lepton which was discovered in the 1970s, and this was experimentally verified by the DONUT collaboration in 2000 [5]. Excepting the 2013 discovery of the higgs boson, this makes the τ -neutrino the most recent SM particle to be identified.

1.2 The Standard Model Neutrino

The Standard Model of particle physics describes the unification of three of the four fundamental forces of nature — electromagnetism, the weak force, and the strong force — within the framework of quantum field theory. The theory has produced an astounding number of predictions which have been experimentally tested and verified, although efforts to include the final force — gravity — have so far been unsuccessful. Despite this, the SM remains one of the most useful, and rigorously tested theories in modern physics.

¹Two gamma rays are produced when the positron annihilates with an electron, the third is produced some microseconds later, when the neutron is captured by an atomic nucleus and releases the excess energy.

The SM is intimately tied with group theory, based on a $SU(3)_C \times SU(2)_L \times U(1)_Y$ gauge group, where the subscripts C , L and Y denote colour charge, left handed chirality and the weak hypercharge respectively. When spontaneously broken, this becomes $SU(3)_{\text{colour}} \times U(1)_{\text{em}}$, and fermions of the SM can be thought of as irreducible representations of this group. After electroweak symmetry breaking, there are eight gluons (g) corresponding to the $SU(3)$ part of the gauge group, and four gauge bosons (W^\pm, Z^0, γ) corresponding to the unified electroweak part of the gauge group ($SU(2) \times U(1)$). The symmetry group of the SM completely determines the allowed interactions for the fundamental fermions (which are shown in table 1.1). These fundamental fermions are believed to be the constituents of all matter, including baryons (bound states of three quarks), mesons (bound quark-anti-quark states), and leptons (single fermions such as the electron).

The SM can be formalised in terms of a Lagrangian density (\mathcal{L} , colloquially just referred to as the Lagrangian), which contains terms for the mass, kinetics, and interactions of all of the fundamental fermions. The parts of the SM Lagrangian which are relevant for neutrino interactions are given by equation 1.1 and equation 1.2:

$$\mathcal{L}_\nu^{cc} = -\frac{ig}{\sqrt{2}} \sum_{\alpha=e,\mu,\tau} \overline{\nu_{\alpha L}} W \ell_{\alpha L} + \text{h.c.}, \quad (1.1)$$

$$\mathcal{L}_\nu^{nc} = -\frac{ig}{2 \cos \theta_W} \sum_{\alpha=e,\mu,\tau} \overline{\nu_{\alpha L}} \not{Z}^0 \nu_{\alpha L} + \text{h.c.}, \quad (1.2)$$

where, g denotes the weak coupling constant, θ_W denotes the Weinberg angle, h.c refers to the hermitian conjugate and the Feynman slash notation has been used. Terms in equation 1.1 correspond to interaction vertices with W -bosons and are termed charge-current (CC) interactions due to their ability to transfer electric charge, whilst the term in equation 1.2 correspond to an interaction vertex with the Z -boson and are termed neutral-current (NC) interactions due to their inability to do so. Examples of each of these interactions can be found in figure 1.1. It is currently thought that there are three *active* neutrinos: the electron neutrino, ν_e , the μ neutrino, ν_μ and the tau neutrino ν_τ . The possibility of a fourth generation of fermions (including neutrinos) has been widely discussed, however plots such as that of the Z^0 resonance [6] and results from the Large Hadron Collider have pushed these theories to higher and higher scales, and so theories with a fourth generation are not discussed further in this dissertation.

Within quantum field theory, a general field ψ can be projected out in to left-handed

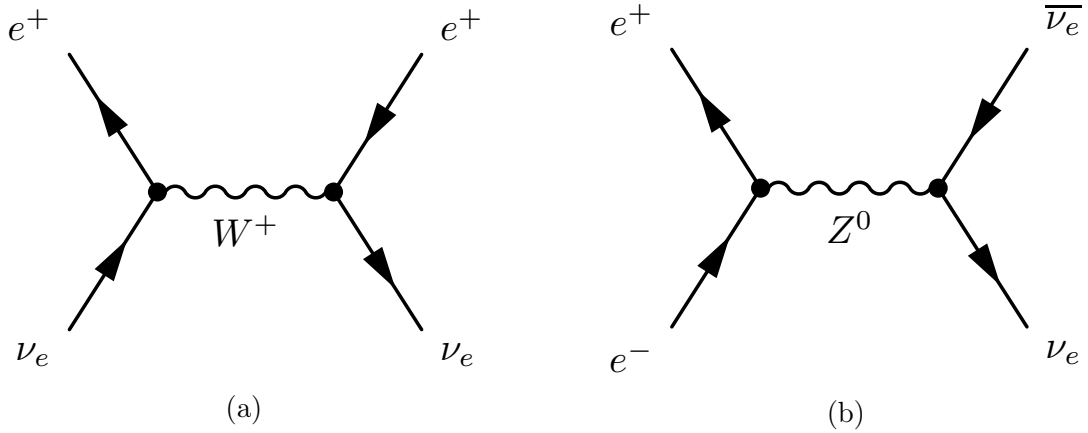


Figure 1.1: Example CC and NC interaction channels for neutrinos.

and right-handed components using the projection operators $P_L\psi = \frac{1}{2}(1 - \gamma_5)\psi$ and $P_R\psi = \frac{1}{2}(1 + \gamma_5)\psi$. The "handedness" of a particle here refers to its chirality, not its helicity², where chirality defines whether a particle transforms under a left or right-handed representation of the Poincaré group. Because the weak force violates chirality maximally [7], only left handed neutrinos are contained within the SM, meaning that no standard mass term can be created. This means that neutrinos are assumed to have zero mass in the SM. Further discussion on the topic of non-zero neutrino masses can be found in section 1.3 and chapter 2. As neutrinos are the only electrically neutral fermion in the SM, the question of whether they are Dirac or Majorana in nature is still open. In either case it is possible to generate neutrino mass, either through introducing a right handed neutrino which is a singlet under the SM gauge group (for Dirac masses) or by demanding that the neutrino is its own antiparticle (for Majorana masses). By doing this a Lorentz-invariant mass term is able to be written down, although these terms may suffer from problems such as non-renormalizability or lepton number violation³.

1.3 Neutrinos beyond the Standard Model

During the 1960s, experiments focusing on detection of solar neutrinos (Homestake, followed by Brookhaven) stumbled upon a problem which perplexed physicists for nearly four decades and was termed *the solar neutrino problem*. The dominant theories of ther-

²Helicity is defined as a projection of a particle's spin on to the direction of its momentum. It is not Lorentz invariant, as boosting in to another reference frame can change the helicity, however in the case where the particle is massless, or can be neglected, then helicity and chirality are equivalent.

³The SM is lepton number conserving, however this is an accidental symmetry and so a lepton number violating term is not expressly forbidden. L-violating interactions have been theorised as one of the ingredients needed for leptogenesis — one of the leading theories which could be used to explain the baryon/lepton-asymmetry of the universe.

	Quarks		Leptons	
Gen. I	u	d	e	ν_e
Gen. II	c	s	μ	ν_μ
Gen. III	t	b	τ	ν_τ
Electric Charge	$\frac{2}{3}$	$-\frac{1}{3}$	1	0

Table 1.1: Table of fundamental fermions contained in the SM. Quarks interact via all of the fundamental forces and have non-integer electric charge, whilst leptons do not undergo strong interactions and have an integer charge. The characteristic which makes each generation distinct is the mass of the particles contained within each generation. Generation I is the lightest group of fermions and generation III is the most massive.

monuclear fusion in the core of the sun predicted that neutrinos should be produced several times through interactions in the proton-proton chain, most notably by PP⁴ and PEP⁵ reactions. This idea was challenged however, when it was shown that there was a huge discrepancy between the number of PEP-reaction neutrinos⁶ which could be experimentally detected, and the number which were theoretically predicted [8]. This problem was further aggravated when it was found that atmospheric neutrinos suffered from a similar problem. Atmospheric neutrinos are produced when cosmic rays interact with nuclei in the upper atmosphere, producing hadronic showers which decay in to pions and kaons, and then in to secondary products including neutrinos. The absolute flux of both atmospheric ν_μ and ν_e are only known to $\sim 30\%$ accuracy [9], however by measuring the ratio of muon and electron neutrinos, $\frac{\nu_\mu}{\nu_e}$ experimentalists were able to determine the ratio to $\sim 5\%$ uncertainty, and thus were able to prove that a discrepancy between the data and Monte-Carlo simulations existed. This was imaginatively called *the atmospheric neutrino problem*.

For several decades, myriad theories pertaining to both of these issues were proposed, however no theory was found to be acceptable due to a lack of backing experimental evidence. However, one idea in particular began to gain traction. In 1957, inspired by $\overline{K^0} \leftrightarrows K^0$ oscillations [10], Bruno Pontecorvo began to explore how neutrinos might

⁴($p + p \rightarrow^2 H + e^+ + \nu$)

⁵($p + e^- + p \rightarrow^2 H + \nu$)

⁶The PEP reaction was favoured over the PP reaction as the experimental methods which were used (For Brookhaven, $\nu + ^{37} Cl \rightarrow ^{37} Ar + e^-$) were not sensitive to the lower energy PP neutrinos. The PEP/PP ratio was relatively constant for the most accepted solar models, allowing a total number of neutrinos to be calculated.

change from one flavour (e , μ , τ) to another in a process which was dubbed *neutrino oscillations*. It was suggested that electron neutrinos could oscillate in to μ or τ neutrinos during their flight from source to detector, and this would explain the deficit in electron neutrinos observed. This was a somewhat controversial idea, however, as for neutrinos to oscillate they must be given a small mass. This is discussed in detail in chapter 2.

Experimental success with the neutral kaon system meant that neutrino oscillations garnered popularity very quickly, and inspired several groups to set forth with the ambitious objective of experimentally verifying the oscillations. These efforts came to a head when oscillations of atmospheric neutrinos were confirmed by the Super-Kamiokande collaboration in 1998 [11] by studying the zenith angle dependence of electron and muon neutrino flux. Meanwhile, oscillations of solar neutrinos were measured by the SNO collaboration, working from the previous work of Homestake [12, 13], meaning that the flavour changing nature of neutrinos now has a solid grounding in both theory and experiment. The current generation of neutrino oscillation experiments have constrained the oscillation parameters to those located in reference [14]. In particular, KamLAND dominates the measurement of the solar parameters, θ_{12} and Δm_{21}^2 , MINOS dominates the measurements of Δm_{31}^2 and gives guidance on θ_{23} , and this generation of reactor experiments, namely Daya Bay, RENO, and Double CHOOZ, dominate the measurement of θ_{13} , which was recently confirmed to be non-zero to 5σ .

That neutrino oscillations have been confirmed is extremely exciting, and has implications not just within the realm of neutrino physics but within the whole field of high energy physics, as they are the first experimental evidence of physics beyond the standard model.

1.4 Outline of this Dissertation

This dissertation is primarily focused on the physics of neutrino oscillations, how they can be detected and the implications of present and future experiments in this field. The next generation of neutrino oscillation experiments are expected to shed light on three big unknowns in neutrino oscillations: the mass hierarchy, CP violation and the octant of θ_{23} . With the aim of demonstrating the future of the field, GLoBES simulations of the Long Baseline Neutrino Experiment will be performed in such a way that quantifies its ability to answer these questions. LBNE has been chosen as it is particularly important to the future of neutrino oscillation physics, having been made a priority by Fermilab:

funding for a reduced initial stage has already been secured, and alternative avenues of financing are currently being explored. In order to explore the effectiveness of LBNE, it is first necessary to introduce the robust theory of neutrino oscillations and analyse how they can be described within the framework of quantum field theory.

This introduction has briefly outlined why neutrinos were originally introduced and their place within the Standard Model (SM). Chapter 2 introduces the idea of non-SM neutrinos and neutrino oscillations, 2ν and 3ν oscillation models (for both vacuum and matter oscillations), and contains a discussion on the current state of neutrino physics. Chapter 3 reviews some of the current oscillation experiments and analyses their strengths, particularly with respect to which types of experiment dominate the measurements of each of the oscillation parameters. Chapter 4 and chapter 5 contain a brief overview of the statistics relevant to neutrino oscillations, and a number of simulations of the future Long Baseline Neutrino Experiment (LBNE). In chapter 6, the results are summarised and their implications are discussed.

Chapter 2

Neutrino Oscillations

2.1 Theory of Oscillations

Although Pontecorvo was the first to suggest neutrino oscillations, his derivation of the phases was only an estimation analogous to the oscillations in the kaon system, and as such the oscillation phases were correct only to a factor of two. The standard derivation of neutrino oscillations was developed in the 1970s by three pairs — Fritzsch and Minkowski [15], Eliezer and Swift [16] and Bilenky and Pontecorvo [17]. In this standard derivation (reviewed in section 2.1.1), neutrinos are treated as plane waves and a number of assumptions are made, which ultimately have been revealed to be unfounded. This naturally lead to the development of a treatment which relies on fewer of these assumptions, the wave-packet treatment, which will be reviewed in section 2.1.3.

It was realised separately by Maki, Sakata, and Nakagawa [18], and by Pontecorvo [19], that if neutrino oscillations were to be described mathematically, small neutrino masses must be introduced. It is now hypothesised that neutrinos have two distinct *states*, flavour states (ν_e, ν_μ, ν_τ) which can be observed and which have well defined weak interactions, and mass states (ν_1, ν_2, ν_3), which propagate through space, and have well defined masses. These states are thought to mix — that is, a flavour state can be thought of as a superposition of mass states, and a mass state can be thought of as a superposition of flavour states.

2.1.1 The Standard Derivation of Neutrino Oscillations Using the Plane Wave Approximation

In the standard derivation of neutrino oscillations flavour states of neutrinos, which are produced along with an anti-lepton ℓ^+ or detected with a lepton ℓ^- , can be represented

by equation 2.1,

$$|\nu_\alpha\rangle = \sum_j U_{\alpha j}^* |\nu_j\rangle. \quad (2.1)$$

This equation is the mathematical formulation of the statement that a flavour state is a superposition of massive states, and by the unitarity of U , it is understood that massive neutrinos are therefore a superposition of flavour states,

$$|\nu_j\rangle = \sum_\alpha U_{\alpha j} |\nu_\alpha\rangle, \quad (2.2)$$

where Greek indices denote flavour states, Roman indices denote mass states and U denotes some unitary leptonic mixing matrix. From this principle, a mathematical description of neutrino oscillations can be constructed. It should be noted that the number of mass states in the above equation is not limited. In the SM there are three flavour states (called *active* neutrinos), and so there must be at least three massive states, but there remains a possibility of additional mass states. If these additional states exist, then they are said to be *sterile*, i.e. they do not interact via SM interactions.

In order to set up an orthonormal basis for the mass states¹, a finite normalisation volume is utilised as discussed in appendix A. Massive states $|\nu_j\rangle$ are eigenstates of the Hamiltonian,

$$\mathcal{H} |\nu_j\rangle = E_j |\nu_j\rangle, \quad (2.3)$$

with eigenvalues given by the dispersion relation

$$E_j = \sqrt{\vec{p} + m_j}. \quad (2.4)$$

By considering the time dependant Schröedinger equation for a massive state, which has definite energy E_j and mass m_j , it can be seen that neutrinos evolve in time as plane waves,

$$i \frac{d}{dt} |\nu_j(t)\rangle = \mathcal{H} |\nu_j(t)\rangle, \quad (2.5)$$

$$|\nu_j(t)\rangle = e^{-iE_j t} |\nu_j\rangle. \quad (2.6)$$

Because flavour states can be detected, and so are more experimentally interesting than massive states, the evolution of a flavour state is considered by using equation 2.1 along

¹An orthonormal basis means that $\langle \nu_i | \nu_j \rangle = \delta_{ij}$, and due to the unitarity of the mixing matrix U , this also implies that the flavour states are orthonormal, $\langle \nu_\alpha | \nu_\beta \rangle = \delta_{\alpha\beta}$

with equation 2.6, giving the time evolution equation

$$|\nu_\alpha(t)\rangle = \sum_j U_{\alpha j}^* e^{-iE_j t} |\nu_j\rangle. \quad (2.7)$$

Now, by substituting via the relation in equation 2.2,

$$|\nu_\alpha(t)\rangle = \sum_\beta \sum_j U_{\alpha j}^* U_{\beta j} e^{-iE_j t} |\nu_\beta\rangle, \quad (2.8)$$

and so the initial flavour state $|\nu_\alpha\rangle$ transforms to some different flavour state $|\nu_\beta\rangle$ after some time t . The coefficient of $|\nu_\beta\rangle$ is the time-dependant amplitude for a transition of a neutrino of flavour α to a neutrino of flavour β . By squaring this transition amplitude, the probability of a transition from $\nu_\alpha \rightarrow \nu_\beta$ can be obtained,

$$P_{\nu_\alpha \rightarrow \nu_\beta}(t) = |\langle \nu_\beta | \nu_\alpha(t) \rangle|^2 \quad (2.9)$$

$$= \left| \sum_j U_{\alpha j}^* U_{\beta j} e^{-iE_j t} \right|^2 \quad (2.10)$$

$$= \sum_{j,k} U_{\alpha j}^* U_{\beta j} U_{\alpha k} U_{\beta k}^* e^{-i(E_j - E_k)t}. \quad (2.11)$$

As data from the Planck collaboration places an upper bound on the sum of the masses of the active neutrinos at 0.23 eV [20], they can be considered as ultrarelativistic particles, and so the dispersion relation in equation 2.4 can be approximated by Taylor expanding,

$$E_j = E + \frac{m_j^2}{2E}. \quad (2.12)$$

If this substitution is made and at the same time it is realised that neutrinos travel at approximately the speed of light allowing a second approximation $t = L$ to be made², then the final probability equation is given by

$$P_{\nu_\alpha \rightarrow \nu_\beta}(t) = \sum_{j,k} U_{\alpha j}^* U_{\beta j} U_{\alpha k} U_{\beta k}^* e^{-i\frac{\Delta m_{jk}^2}{2E}L} \quad (2.13)$$

where Δm_{jk}^2 is the *mass-squared difference*, $m_j^2 - m_k^2$. This shows that not only do neutrinos need to have mass, but also that at least one of the neutrino masses of the active neutrinos must be non-degenerate in order for them to oscillate.

A slightly different form of the neutrino oscillation probability given in equation 2.13

²This is preferable as in neutrino experiments, the propagation time t is not measured, however the baseline L is experimentally controlled.

may be derived which is easier to deal with analytically. This can be done by starting from equation 2.10 and equation 2.12 and noticing that this allows the probability to be written as

$$P_{\nu_\alpha \rightarrow \nu_\beta}(t) = \left| \sum_j U_{\beta j}^* U_{\alpha j} \exp(-iEL) \exp\left(-i \frac{m_j^2 L}{2E}\right) \right|^2 \quad (2.14)$$

$$= \left| \exp(-iEL) \exp\left(-i \frac{m_1^2 L}{2E}\right) \right|^2 \left| \sum_j U_{\beta j}^* U_{\alpha j} \exp\left(-i \frac{\Delta m_{j1}^2 L}{2E}\right) \right|^2 \quad (2.15)$$

$$= \left| \sum_j U_{\beta j}^* U_{\alpha j} \exp\left(-i \frac{\Delta m_{j1}^2 L}{2E}\right) \right|^2, \quad (2.16)$$

where the $t = L$ approximation has been made. In the second line, the parts which have been separated out will disappear when the modulus squared is taken, hence dropping the terms on the final line. The main difference between this and the previous probability equation is that this measures the mass-squared differences with respect to m_1^2 , reducing the number of terms which need to be calculated.

As mentioned in section 2.1, this derivation relies on a number of assumptions:

Equal momentum assumption

This assumption states that all massive neutrino components travel with the same momentum.

Light-ray approximation

This corresponds to making the substitution $t = L$, which is unjustified in the plane-wave approximation as plane waves extend over the whole of space-time with the same amplitude.

Flavour state assumption

This is the assumption that CC-produced neutrinos are described by flavour states defined in equation 2.1.

These assumptions are unfounded in this derivation, however quantum field theoretical calculations performed widely in the literature have found that the final probability obtained here is true for terrestrial oscillation experiments. This will be discussed in section 2.1.2 and section 2.1.3.

As probability is a dimensionless quantity, it is necessary that the right hand side of equation 2.13 is also dimensionless. The elements of the unitary matrix are always dimensionless quantities, and so the only term that needs to be altered is the exponent,

$\frac{\Delta m_{jk}^2}{2E} L$. Due to trigonometric identities, these exponents are usually presented as $\frac{\Delta m_{jk}^2}{4E} L$ in final probabilities, and so this is what must be made dimensionless. As the units of the mass-squared difference are eV², and the units of the energy are usually given in GeV, the baseline L (given in km) must be phrased in inverse eV.

To calculate the conversion constant, natural units are dropped and the Planck relation,

$$\lambda = \frac{\hbar c}{E}, \quad (2.17)$$

is used. From this equation it is easy to see that to express L in terms of inverse eV, a factor of $(\hbar c)^{-1}$ is required, and so

$$\frac{10^3 \times 1.6 \times 10^{-19}}{10^9 \hbar c} \frac{\Delta m_{jk}^2}{4E} L = 1.27 \frac{\Delta m_{jk}^2}{E} L \quad (2.18)$$

is dimensionless.

2.1.2 Quantum Field Theory of Flavour States in the Plane-Wave Approximation

In reference [21], it was found that the description of neutrinos manifest in equation 2.1 is inadequate, as the description differs slightly from standard quantum field theory. It can, however, be shown that for neutrino oscillation experiments, the neutrino flavour states reduce to those given in equation 2.1.

Fock states corresponding to the flavour basis of neutrinos have been shown to be possible in reference [22], however these suffer from many problems; the creation and annihilation operators are shown to be time-dependant and so do not satisfy the canonical commutation relations, the number of Fock spaces for the flavour states are infinite, and it has been shown that these flavour Fock spaces cannot partake in interaction processes [23]. This last point is naturally a problem, as all neutrino oscillation experiments rely on interactions for both the production and detection of neutrinos.

To approach the problem of flavour states within quantum field theory, a generic decay process is considered,

$$P_I \rightarrow P_F + \ell_\alpha^+ + \nu_\alpha, \quad (2.19)$$

in which P_I is some state of initial particles and P_F is a state of final particle products. Along with these final products, an anti-lepton ℓ_α^+ and neutrino ν_α , both of flavour α are

produced. The final state $|f\rangle$ can be phrased in the following way:

$$|f\rangle = S |P_I\rangle. \quad (2.20)$$

Here, S is the S -matrix operator. By noting that the flavour state neutrino is a linear superposition of massive states, a flavour neutrino state can be written as

$$|\nu_\alpha\rangle = \sum_k |\nu_k\rangle \langle \ell_\alpha^+, \nu_k, P_F | S | P_I \rangle, \quad (2.21)$$

where $\langle \ell_\alpha^+, \nu_k, P_F | S | P_I \rangle$ is the relevant element of the S -matrix [24]. As neutrino oscillation experiments are not sensitive to the mass scales of neutrinos, the kinematic part of the S -matrix dependant on neutrino mass can be approximately neglected,

$$\langle \ell_\alpha^+, \nu_k, P_F | S | P_I \rangle \approx U_{\alpha k}^* \langle \ell_\alpha^+, \nu_\alpha, P_F | S | P_I \rangle \Big|_{m_k=0}. \quad (2.22)$$

Here, the right hand side represents the matrix element evaluated under the Standard Model, with neutrino masses set to zero. This approximation does not work for neutrinos with large masses, as may be the case with sterile neutrinos. The treatment in reference [23] gives a good overview of the calculation in this case. By projecting over $|\ell_\alpha^+, P_F\rangle$ in the final state and normalising, the flavour state neutrino is found to be

$$|\nu_\alpha\rangle = \sum_k U_{\alpha k}^* |\nu_k\rangle. \quad (2.23)$$

This equation defines a flavour state produced in the charge-current interaction considered in equation 2.19, and can be seen to be the same as earlier state in equation 2.1.

Between the production and the detection of the neutrino at some different point in space-time (\vec{x}, t) , the neutrino evolves as

$$|\nu_\beta\rangle = \sum_k e^{i(\vec{P}_k \cdot \vec{x} - E_k t)} U_{\alpha k}^* |\nu_k\rangle, \quad (2.24)$$

where the energy $E_k = \sqrt{|\vec{P}_k|^2 + m_k^2}$, and \vec{P}_k is the three momentum of the neutrino. During detection of the neutrino, it will undergo some interaction,

$$D_I + \nu_\beta \rightarrow \ell_\beta^- + D_F, \quad (2.25)$$

where D_I and D_F are some initial and final state particles respectively. Following the

same treatment earlier, the parts of the S -matrix dependant on the neutrino masses may be neglected,

$$\langle \ell_\beta^-, D_F | S | D_I, \nu_k \rangle \approx U_{\beta k} \langle \ell_\beta^-, D_F | S | D_I, \nu_\beta \rangle \Big|_{m_k=0}. \quad (2.26)$$

By projecting over $|D_I\rangle$ in the initial state and using the unitarity of U , the transition amplitude can be derived to be

$$A_{\nu_\alpha \rightarrow \nu_\beta}(\vec{x}, t) = \sum_k U_{\beta k} U_{\alpha k}^* e^{i(\vec{P}_k \cdot \vec{x} - E_k t)}, \quad (2.27)$$

up to some global phase which is irrelevant to neutrino oscillations. If this is reduced to a one dimensional case in which all of the massive neutrinos travel in one direction, L , and then the assumption that $t = L$ along with plane-wave approximation, then

$$-E_k t + P_k L = -(E_k - P_k)L = -\frac{E_k^2 - P_k^2}{E_k + P_k}L = -\frac{m_k^2}{E_k + P_k}L \approx -\frac{m_k^2}{2E}L. \quad (2.28)$$

It should be noted here that the phases relevant to neutrino oscillations are independent of the massive neutrino energy or momentum. When this replacement is made, and the transition amplitude is squared then the probability is given by

$$P_{\nu_\alpha \rightarrow \nu_\beta}(t) = \sum_{j,k} U_{\alpha j}^* U_{\beta j} U_{\alpha k} U_{\beta k}^* e^{-i\frac{\Delta m_{jk}^2}{2E}L}, \quad (2.29)$$

which is the same as in equation 2.13, and so it is seen that the flavour states defined in 2.1 are realistic to use for neutrino oscillations.

2.1.3 Wave-Packet treatment

The treatment of neutrino oscillations in the previous sections are useful, however the assumption that neutrinos act as plane-waves is naive. The reasoning is obvious: plane-waves extend over the entirety of space-time and so cannot be involved in local events such as production and detection of particles. The solution to this glaring problem is to treat massive neutrino states as wave-packets.

The wave-packet approach deals with four issues set out in reference [25] which must be addressed for successful treatment of neutrino oscillations:

- i Both the source and the detector must be localised in areas much smaller than the oscillation length. This can be understood in terms of the uncertainty principle, $\sigma_x^I \sigma_p^I \sim \frac{1}{2}$. If massive neutrinos are measured precisely enough for the ν_i to be de-

terminated, then they will be delocalised to an area much larger than the oscillation length, and so the neutrino oscillation will not be detected [26], indicating that the location of the interactions must be limited so there is sufficient spread of momenta.

- ii The different neutrino mass eigenstates must travel with different momenta, in accordance with energy-momentum conservation.
- iii The different neutrino mass eigenstates must be produced and detected coherently. Once the neutrinos have fallen out of coherence, the neutrino wave functions no longer overlap and cannot interfere with each other to produce oscillations.
- iv The wavefunction of any propagating neutrino must be a superposition of mass eigenstates.

The treatment given here is for the 1 dimensional case. This is done for clarity, and so that the physics can be easily explored. A three dimensional treatment by similar methods can be found in reference [27], and there are several sources which give a full in-depth treatment, see in particular references [28] and [29].

To study the wave-packet treatment, a generic process is used in analogy with the plane-wave treatment,

$$P_I \rightarrow P_F + \mu^+ + \nu \implies \nu + D_I \rightarrow D_F + e^- . \quad (2.30)$$

The final state can be phrased as

$$|f\rangle = \sum_k \int \frac{d^3 p}{(2\pi)^3 2E_k} \sum_h \mathcal{A}_{\alpha k}^I(\vec{p}, h) |\nu_k(E_k, \vec{p}, h), \ell_\alpha^+, P_F\rangle + \dots , \quad (2.31)$$

where $\mathcal{A}_{\alpha k}^I(\vec{p}, h) = \langle \nu_k(E_k, \vec{p}, h), \ell_\alpha^+, P_F | f \rangle$ is the amplitude for the interaction process of $|\nu_k(E_k, \vec{p}, h)\rangle$, E_k is the energy of the k th massive neutrino, \vec{p} is momentum, and h labels helicity. For $I=P$, then this denotes a production process, and for $I=D$ then this denotes a detection process. The ellipsis denotes the other final states which may be produced. As in the plane-wave case, the normalised neutrino flavour state can be found by projecting the final state over $|\ell_\alpha^+, P_F\rangle$,

$$|\nu_\alpha^I\rangle = \mathcal{N}_\alpha^I \sum_k \int \frac{d^3 p}{(2\pi)^3 2E_k} \sum_h \mathcal{A}_{\alpha k}^I(\vec{p}, h) |\nu_k(E_k, \vec{p}, h)\rangle . \quad (2.32)$$

This satisfies condition **iv** given in the list at the start of this section, as it is easy to see that the equation contains a superposition of massive neutrino eigenstates. The

normalisation factor, \mathcal{N}_α^I , is given by

$$\mathcal{N}_\alpha^I = \left(\sum_k \int \frac{d^3 p}{(2\pi)^3 2E_k} \sum_h |\mathcal{A}_{\alpha k}^I(\vec{p}, h)|^2 \right)^{-1/2}. \quad (2.33)$$

By neglecting mass effects in the production and detection processes, as oscillation experiments are not sensitive to the mass scales of neutrinos, these neutrino states can be written as in reference [30],

$$|\nu_\alpha^I\rangle = \sum_k U_{\alpha k}^* \int dp \Psi_k^I(p) |\nu_k(p)\rangle, \quad (2.34)$$

where, provided the spread of the momentum is sharply peaked around the average momentum and can be assumed to be Gaussian, the wave function is given by

$$\Psi_k^I(p) = \frac{1}{(2\pi(\sigma_p^I)^2)^{1/4}} \exp \left[-\frac{(p - p_k)^2}{4(\sigma_p^I)^2} \right]. \quad (2.35)$$

Allowing the different massive neutrinos to have different momenta, p_k , indicates conservation of momentum and fulfils condition **ii** from the list at the beginning of this section.

A freely propagating neutrino in one dimensional space-time can be described by the evolution equation

$$|\nu(L, T)\rangle = e^{-iE_k T + ipL} |\nu_\alpha^P\rangle, \quad (2.36)$$

where the one dimensional case has been used for clarity. This means that the amplitude for a $\nu_\alpha \rightarrow \nu_\beta$ transition can be written as

$$A_{\nu_\alpha \rightarrow \nu_\beta}(L, T) = \langle \nu_\beta^D | e^{-iE_k T + ipL} | \nu_\alpha^P \rangle. \quad (2.37)$$

Now, using the flavour states defined in 2.35, the amplitude can be written as

$$\mathcal{A}_{\alpha\beta}(L, T) \propto \sum_k U_{\alpha k}^* U_{\beta k} \int dp \exp \left[-iE_k(p)T + ipL - \frac{(p - p_k)^2}{4\sigma_p^2} \right], \quad (2.38)$$

where the terms which are not relevant to neutrino oscillations have been neglected, $E_k(p) = \sqrt{p^2 + m_k^2}$, and $\frac{1}{\sigma_p^2} = \frac{1}{(\sigma_p^P)^2} + \frac{1}{(\sigma_p^D)^2}$. As the momentum distribution is sharply peaked at the average momentum, $\sigma_p \ll E_k^2(p_k)/m_k$, the approximation,

$$E_k(p) \simeq E_k + v_k(p - p_k), \quad (2.39)$$

can be made, where

$$E_k = \sqrt{p_k^2 + m_k^2} \quad (2.40)$$

is the average energy and

$$v_k = \frac{\partial E_k(p)}{\partial p} \Big|_{p=p_k} = \frac{p_k}{E_k} \quad (2.41)$$

is the group velocity. By using this approximation, the integration over p is Gaussian and so can be performed analytically via integration by substitution:

$$\mathcal{A}_{\alpha\beta}(L, T) \propto \sum_k U_{\alpha k}^* U_{\beta k} \exp \left[-iE_k T + ip_k L - \frac{(L - v_k T)^2}{4\sigma_x^2} \right]. \quad (2.42)$$

Here, the last term of the exponential is the extra “wave packet” part. The amplitude is still dependant upon T here, which is undesirable as the flight time of neutrinos is not measured. To remove this dependance, the amplitude is squared to find the probability, and an integration by substitution is performed over T . The probability can then be found to be

$$P_{\nu_\alpha \rightarrow \nu_\beta}(L) \propto \sum_{k,j} U_{\alpha k}^* U_{\beta k} U_{\alpha j} U_{\beta j}^* \exp \left[-i \left((E_k - E_j) \frac{v_k + v_j}{v_k^2 + v_j^2} \right) L \right] \times \exp \left[-\frac{L^2}{2\sigma_x^2} + \frac{(v_k L)^2 + (v_j L)^2}{2\sigma_x^2(v_k^2 + v_j^2)} - \frac{[(v_k - v_j)L]^2}{4\sigma_x^2(v_k^2 + v_j^2)} - \frac{(E_k - E_j)^2}{4\sigma_p^2(v_k^2 + v_j^2)} \right], \quad (2.43)$$

where the first exponential generates oscillations, and the second term acts as a damping term, i.e. for large spatial uncertainty the oscillations will be diminished. By now using the ultrarelativistic approximation,

$$E_k \simeq E + \zeta \frac{m_k^2}{2E}, \quad (2.44)$$

$$p_k \simeq E - (1 - \zeta) \frac{m_k^2}{2E}, \quad (2.45)$$

where ζ is a value which is dependant on the specifics of the production process. The probability can finally be written as

$$P_{\nu_\alpha \rightarrow \nu_\beta}(L) = \sum_{k,j} U_{\alpha k}^* U_{\beta k} U_{\alpha j} U_{\beta j}^* \exp \left[-2\pi i \frac{L}{L_{kj}^{osc}} - \left(\frac{L}{L_{kj}^{coh}} \right)^2 - 2\pi^2 \zeta^2 \left(\frac{\sigma_x}{L_{kj}^{osc}} \right)^2 \right], \quad (2.46)$$

where the second term of the exponential is known as the *coherence* term and the last term of the exponential is known as *localisation* term. The oscillation and coherence

lengths are given by

$$L_{kj}^{osc} = \frac{4\pi E}{\Delta m_{kj}^2}, \quad (2.47)$$

$$L_{kj}^{coh} = \frac{4\sqrt{2}E^2}{|\Delta m_{kj}^2|}\sigma_x. \quad (2.48)$$

This treatment indicates the existence of some ‘‘coherence length’’, L_{kj}^{coh} , beyond which neutrino oscillations should be suppressed. This is physically due to separation of the different massive neutrino wave packets, each of which travels with a different velocity, v_k , and can be understood by explicitly writing the coherence term:

$$P_{\nu_\alpha \rightarrow \nu_\beta}^{coh} = \exp \left[\left(\frac{L}{L_{kj}^{coh}} \right)^2 \right] = \exp \left[\left(-\frac{L|\Delta m_{kj}^2|}{4\sqrt{2}E^2\sigma_x} \right)^2 \right]. \quad (2.49)$$

This indicates that for a constant spatial uncertainty there is a length beyond which the wave packets are unable to interact due to their spatial positions, i.e. beyond this point, the wave packets are so separated that they cannot overlap with each other and with the detection process. For this case, the damping term will increase and neutrino oscillations will be suppressed. A graphical representation of this can be found in reference [30]. The existence of such a coherence length provides a mechanism for condition **iii**. The localisation term,

$$P_{\nu_\alpha \rightarrow \nu_\beta}^{loc} = \exp \left[-2\pi^2 \zeta^2 \left(\frac{\sigma_x}{L_{kj}^{osc}} \right)^2 \right], \quad (2.50)$$

contributes a suppression to neutrino oscillations if $\sigma_x > L_{kj}^{osc}$. This indicates that neutrinos should be localised: their spacial uncertainty must therefore be localised to an area smaller than the oscillation length. This is satisfied in all neutrino oscillation experiments. Provided that this is the case, then the localisation term can be safely neglected as it causes no suppression. This means that the probability is effectively given by

$$P_{\nu_\alpha \rightarrow \nu_\beta}(L) = \sum_{k,j} U_{\alpha k}^* U_{\beta k} U_{\alpha j} U_{\beta j}^* \exp \left[-2\pi i \frac{L}{L_{kj}^{osc}} - 2\pi^2 \zeta^2 \left(\frac{\sigma_x}{L_{kj}^{osc}} \right)^2 \right] \quad (2.51)$$

for physical experiments. This fulfils condition **i** set out at the beginning of this section.

2.1.4 CP, T and CPT transformations

By calculating the transition probability for anti-neutrinos explicitly, as done in reference [27], it can be shown that the transition probabilities for neutrinos and anti-neutrinos are

related by a charge-parity (CP) transformation, which reverses the chirality,

$$P_{\nu_\alpha \rightarrow \nu_\beta} \xleftrightarrow{\text{CP}} P_{\bar{\nu}_\alpha \rightarrow \bar{\nu}_\beta}. \quad (2.52)$$

Similarly to this, the initial and final flavour states can be interchanged by a time reversal (T) transformation,

$$P_{\nu_\alpha \rightarrow \nu_\beta} \xleftrightarrow{\text{T}} P_{\nu_\beta \rightarrow \nu_\alpha}. \quad (2.53)$$

By combining the above transformations, a CPT transformation both interchanges the initial and final flavour states and exchanges neutrinos for anti-neutrinos (or vice-versa),

$$P_{\nu_\alpha \rightarrow \nu_\beta} \xleftrightarrow{\text{CPT}} P_{\bar{\nu}_\beta \rightarrow \bar{\nu}_\alpha}. \quad (2.54)$$

CPT conservation is an assumed symmetry of any Lorentz invariant local quantum field theory such as the SM, and as such the relation in equation 2.54 can be replaced with an equality

$$P_{\nu_\alpha \rightarrow \nu_\beta} = P_{\bar{\nu}_\beta \rightarrow \bar{\nu}_\alpha}. \quad (2.55)$$

It is supposed, however, that at Planck scales Lorentz invariance and CPT invariance may break down [31], and so this assumption may not be valid and some small variation in the equality must then be allowed. It is thought that neutrino oscillation experiments may shed light on these violations should they exist, however due to the hypothetical nature of these questions they will not be further discussed in this dissertation.

In general, the unitary mixing matrix U is complex, and this leads to violation of the CP symmetry through a CP violating phase. Should CP violation be physical, it should manifest itself in transition probabilities, and so neutrino oscillation experiments should be well situated to determine if CP is violated in the leptonic sector, and determine the value of the CP violating phase. Should CPT invariance hold, then measuring CP violation is equivalent to measuring T violation [32].

2.2 Vacuum Oscillations

This section will analyse the oscillation probabilities in vacuum, first for the unphysical 2ν case and then for the 3ν case which seems to be manifest in nature. This is done by using the PMNS mixing matrix which is found by multiplying the three rotation matrices in three dimensions. Plots showing how varying each of the oscillation parameters can vary the probability will be shown and the effects will be linked with analytical probabilities.

2.2.1 2- ν Oscillations in Vacuum

For the case in which only two flavours of neutrino are considered, say α and β , then the mixing of these two neutrinos depends on only one mixing angle. Indeed, only one two dimensional unitary matrix can be written down,

$$U = \begin{pmatrix} \cos \theta & \sin \theta \\ -\sin \theta & \cos \theta \end{pmatrix}, \quad (2.56)$$

where θ is the two dimensional mixing angle. Assuming that $\alpha \neq \beta$, then the probability can be defined as in 2.16,

$$P_{\nu_\alpha \rightarrow \nu_\beta}(t) = |U_{\alpha 1}^* U_{\beta 1} + U_{\alpha 2}^* U_{\beta 2} e^{-i \frac{\Delta m_{21}^2 L}{2E}}|^2 \quad (2.57)$$

$$= |- \sin \theta \cos \theta + \sin \theta \cos \theta e^{-i \frac{\Delta m_{21}^2 L}{2E}}|^2 \quad (2.58)$$

$$= \cos^2 \theta \sin^2 \theta \left(2 - 2 \cos \left(\frac{\Delta m_{21}^2 L}{2E} \right) \right) \quad (2.59)$$

$$= \sin^2(2\theta) \sin^2 \left(\frac{\Delta m_{21}^2 L}{4E} \right). \quad (2.60)$$

To make sense of probability equations and to bring out the physics contained within it, it is often useful to plot the probability, varying one or more of the parameters. A plot of the probability in equation 2.60 is shown in figure 2.1. It is clear from equation 2.60 that CP violation does not exist in the two neutrino model, as the CP violating phase δ_{CP} is not contained within the probability. This is unsurprising as the 2ν case is unphysical.

2.2.2 3- ν Oscillations in Vacuum

The unitary mixing matrix for the case in which there are 3 active neutrinos can be parametrised by three mixing angles, θ_{12} , θ_{13} and θ_{23} , and a CP violating phase δ_{CP} . It is known as the Pontecorvo-Maki-Nakagawa-Sakata (PMNS) matrix, and is commonly parametrised in the form

$$U_{PMNS} = \begin{pmatrix} 1 & 0 & 0 \\ 0 & c_{23} & s_{23} \\ 0 & -s_{23} & c_{23} \end{pmatrix} \begin{pmatrix} c_{13} & 0 & s_{13} e^{i\delta_{CP}} \\ 0 & 1 & 0 \\ -s_{13} e^{-i\delta_{CP}} & 0 & c_{13} \end{pmatrix} \begin{pmatrix} c_{12} & s_{12} & 0 \\ -s_{12} & c_{12} & 0 \\ 0 & 0 & 1 \end{pmatrix} \quad (2.61)$$

$$= \begin{pmatrix} c_{13} c_{12} & c_{13} s_{12} & s_{13} e^{i\delta_{CP}} \\ -s_{12} c_{23} - s_{23} s_{13} c_{12} e^{-i\delta_{CP}} & c_{23} c_{12} - s_{23} s_{12} s_{13} e^{-i\delta_{CP}} & s_{23} c_{13} \\ s_{23} s_{12} - c_{23} s_{13} c_{12} e^{-i\delta_{CP}} & -c_{12} s_{23} - c_{23} s_{12} c_{13} e^{-i\delta_{CP}} & c_{23} c_{13} \end{pmatrix} \quad (2.62)$$

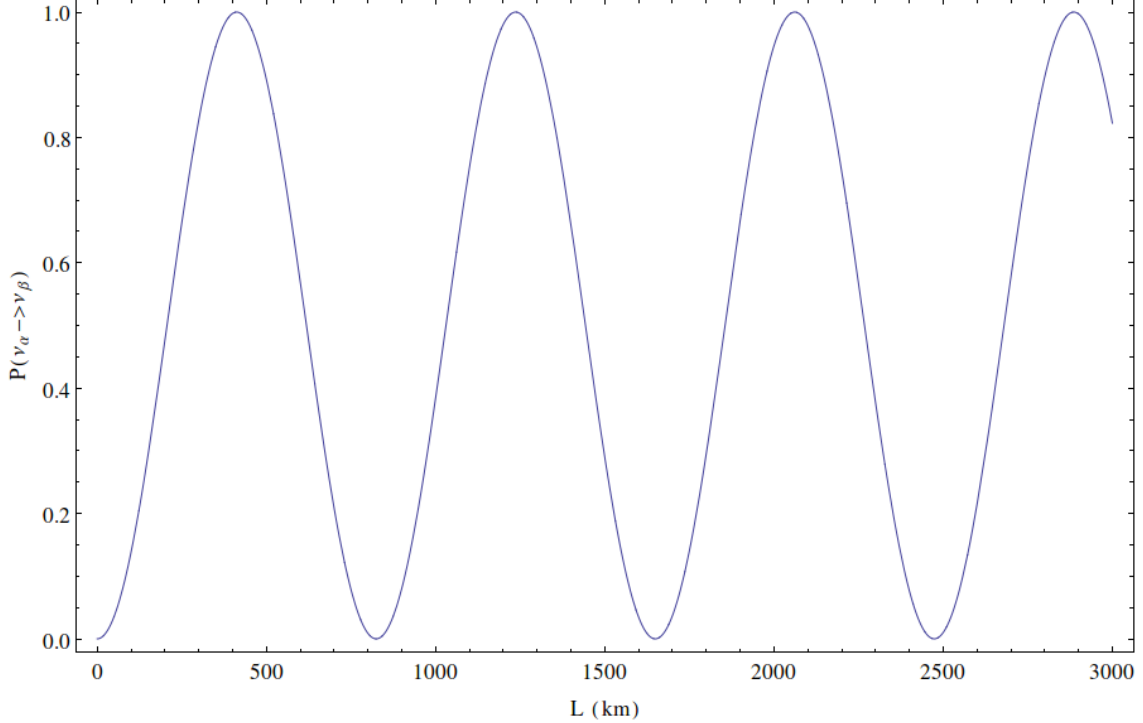


Figure 2.1: A plot of probability for the two neutrino case. The probability is dependant on four parameters, the values of the mixing angle and the mass-squared difference, and the length of baseline and beam energy which are chosen in experiments. For the purpose of demonstration the values for θ , Δm_{12}^2 , and E were chosen to be $\pi/2$, 0.003 eV^2 and 1 GeV respectively, although these values are arbitrary as the 2 neutrino case is unphysical.

where c_{ij} and s_{ij} are shorthand for $\cos \theta_{ij}$ and $\sin \theta_{ij}$ respectively. By using the same method as for the two neutrino case, probabilities for $\nu_e \rightarrow \nu_\mu$, $\nu_e \rightarrow \nu_\tau$ and $\nu_\mu \rightarrow \nu_\tau$ (and their T-transform) transitions can be produced. If equation 2.16 is used to calculate probabilities, then the survival probability for each species of neutrino here must be found via equation 2.63,

$$P_{\nu_\alpha^{\text{survival}}} = 1 - P_{\nu_\alpha \rightarrow \nu_\beta} - P_{\nu_\alpha \rightarrow \nu_\gamma}, \quad (2.63)$$

where $\alpha \neq \beta \neq \gamma$, as equation 2.16 assumes that $\alpha \neq \beta$.

Neutrino oscillations are dependant upon six parameters: The four mentioned earlier (θ_{12} , θ_{13} , θ_{23} , δ_{CP}), and the two mass-squared differences (Δm_{21}^2 , and Δm_{31}^2). By varying each of these parameters, their effect on vacuum oscillations can be measured. In the following sections, plots of $\nu_e \rightarrow \nu_\mu$ transition probabilities are singled out, although the same conclusions could be drawn from any of the other transition channels. It should also be noted that the following plots assume that Δm_{31}^2 is in the *normal hierarchy* and

θ_{23} is in the *lower octant*. An explanation of the mass hierarchy and the θ_{23} octant can be found in section 2.4.

Probabilities can be analytically computed although these are typically messy and often it is enough to use one of many approximations to simplify the procedure. Appendix B.1 shows in particular the one mass-squared dominance (OMSD) case, from which it is easy to calculate the $\nu_e \rightarrow \nu_\mu$ transition probability to be

$$P_{\nu_e \rightarrow \nu_\mu}^{OMSD} = s_{23}^2 \sin^2(2\theta_{13}) \sin^2 \left(\frac{\Delta m_{31}^2 L}{4E} \right). \quad (2.64)$$

Another approximation which can be made is to use perturbation theory to expand to second order in the small parameters, θ_{13} and Δm_{21}^2 . This can be done in analogy with the method taken up by Asano and Minakata in reference [33] and as done in appendix B.2. This results in the following probability:

$$\begin{aligned} P_{\nu_e \rightarrow \nu_\mu}^{(2)} = & s_{23}^2 \sin^2(2\theta_{31}) \sin^2 \left(\frac{\Delta_{31} L}{2} \right) + c_{23} \sin^2(2\theta_{12}) \sin^2 \left(\frac{\Delta_{21} L}{2} \right) \\ & + \tilde{J} \cos \left(\pm \delta - \frac{\Delta_{31} L}{2} \right) \frac{\Delta_{21} L}{2} \sin \left(\frac{\Delta_{31} L}{2} \right), \end{aligned} \quad (2.65)$$

where $\Delta_{ij} = \frac{\Delta m_{ij}}{2E}$, and $\tilde{J} = c_{13} \sin 2\theta_{12} \sin 2\theta_{13} \sin 2\theta_{13}$ is the Jarlskog coefficient. This is analytically useful as the interplay between the terms is much simpler than the probability to all orders, meaning that the physics is much easier to extract. Numerically, it is easy to use the all-orders probability and so this has been used to produce the plots in this section.

Varying δ_{CP}

By studying the PMNS matrix, it can be seen that all transition probabilities for the 3ν case will contain the CP violating phase. This suggests that if CP is violated in the leptonic sector then neutrino oscillations are well poised to detect it.

As seen in figure 2.2, allowing the CP violating phase to vary within its 3σ range ($0-2\pi$) gives rise to a huge change in both the phase and the amplitude of the transition probability. For this reason, along with applications in baryogenesis, δ_{CP} is probably the most important parameter to determine in neutrino physics. Unfortunately, it is also the least well known parameter. Discussions on the ability of future experiments to determine

δ_{CP} (in particular LBNE), can be found in chapter 5.

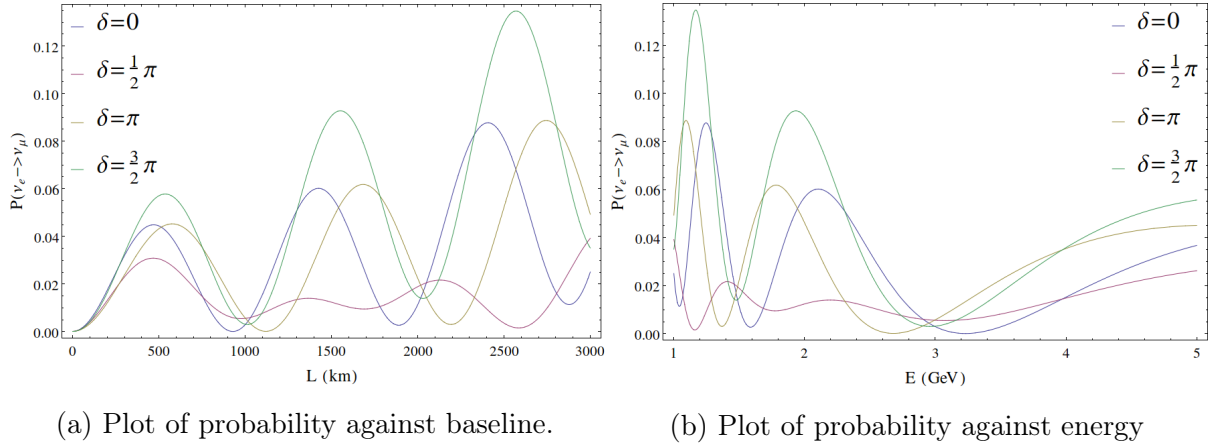


Figure 2.2: Plots of transition probabilities for varying values of δ_{CP} between 0 and 2π .

Varying the mass-squared differences

The difference in masses of the neutrino massive states do not enter the probability through the mixing matrix, but by acting as a relative phase between the two states. The values of both of the mass squared differences have been measured precisely, with solar oscillation experiments such as Sudbury Neutrino Observatory (SNO) and Super-Kamiokande (SK) dominating the measurements of Δm_{21}^2 and atmospheric oscillation experiments such as SK and long baseline experiments such as Main Injector Neutrino Oscillation Search (MINOS) dominating the measurements of Δm_{31}^2 . To this end, the mass-squared differences are often referred to as the solar mass-squared difference, Δm_{sol}^2 , and the atmospheric mass-squared difference Δm_{atm}^2 .

The plots in figure 2.3 and figure 2.4 show how the oscillation probabilities for $\nu_e \rightarrow \nu_\mu$ vary depending on the values of the mass-squared differences. It is obvious that the mass-squared difference associated with solar oscillations, Δm_{21}^2 , has very little effect on the probability for the baselines and energies which are relevant for neutrino oscillation experiments with terrestrial sources. By looking at equation 2.65, it can be seen that this is because Δm_{21}^2 only becomes important when $\Delta m_{21}^2 L$ is of $\mathcal{O}(1)$, or when $L \sim 10^5$ km — much greater than terrestrial distances. The plots in figure 2.3 show the beginnings of a solar oscillation, but they are relatively unimportant at these distances. The mass-squared difference associated with atmospheric oscillations, Δm_{31}^2 , produces a noticeable difference in the phase, and a small difference in amplitude for a wide range of energies and all baselines relevant to long baseline neutrino experiments. It is unsurprising that this has a much greater impact than Δm_{21}^2 , as by looking at equation 2.65 it can be seen

that Δm_{31}^2 is subject to a similar constraint, i.e. to have an important impact, $\Delta m_{31}^2 L$ must be of $\mathcal{O}(1)$, but as Δm_{31} is larger than Δm_{21}^2 by 2 orders of magnitude, it's effects become important at $L \sim 10^3$ km — within the terrestrial range.

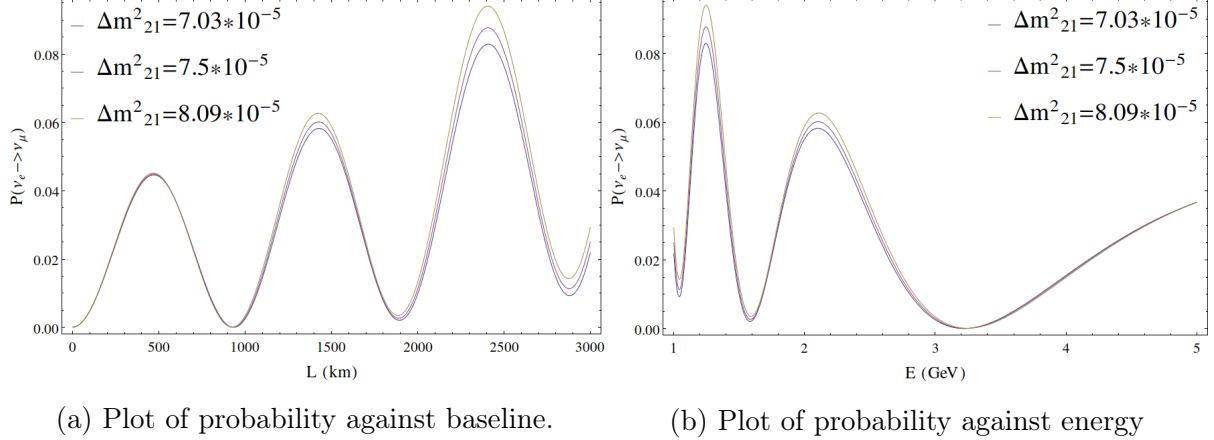


Figure 2.3: Plots of transition probabilities for varying values of Δm_{21}^2 within 3σ range, where $\Delta m_{21}^2 = 7.5 \times 10^{-5}$ is the best fit value according to [14].

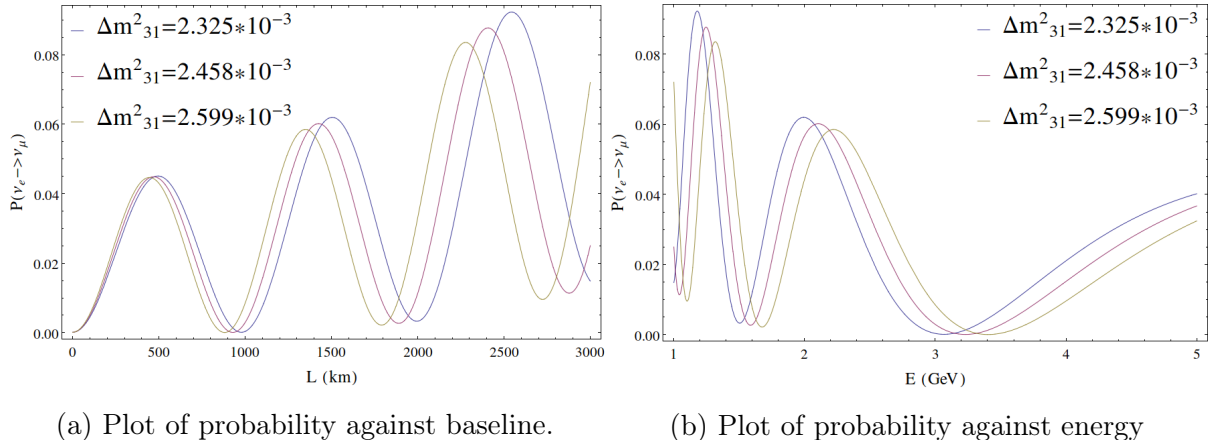
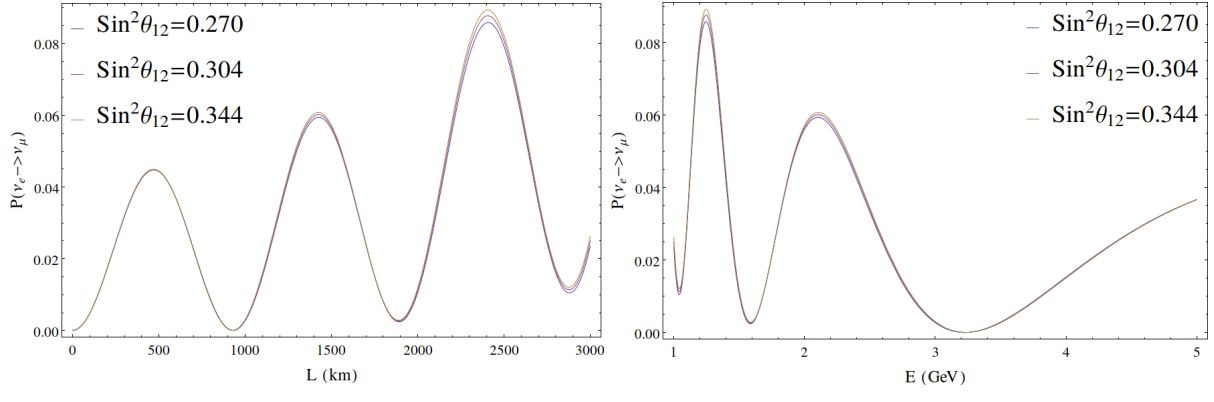


Figure 2.4: Plots of transition probabilities for varying values of Δm_{31}^2 within 3σ range, where $\Delta m_{31}^2 = 2.458 \times 10^{-3}$ is the best fit value according to [14].

Varying the mixing angles

In the same vein as the measurements of the mass-squared differences, data on the values of each of the mixing angles is dominated by a specific type of experiment. θ_{12} is dominantly measured by solar experiments and is sometimes written θ_{sol} , θ_{23} is dominantly measured by atmospheric experiments and is sometimes called θ_{atm} and θ_{13} is dominantly measured by reactor experiments, most notably at Daya Bay and RENO. A discussion

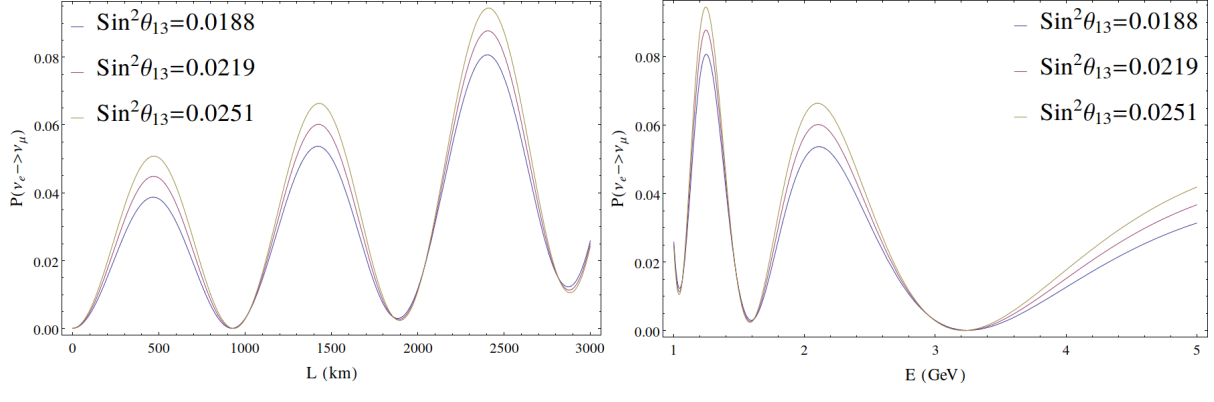
of the different species of experiment and their strengths in determining the different oscillation parameters can be found in section 3.1.



(a) Plot of probability against baseline.

(b) Plot of probability against energy

Figure 2.5: Plots of transition probabilities for varying values of θ_{12} within 3σ range, where $\sin^2 \theta_{12} = 0.304$ is the best fit value according to [14].

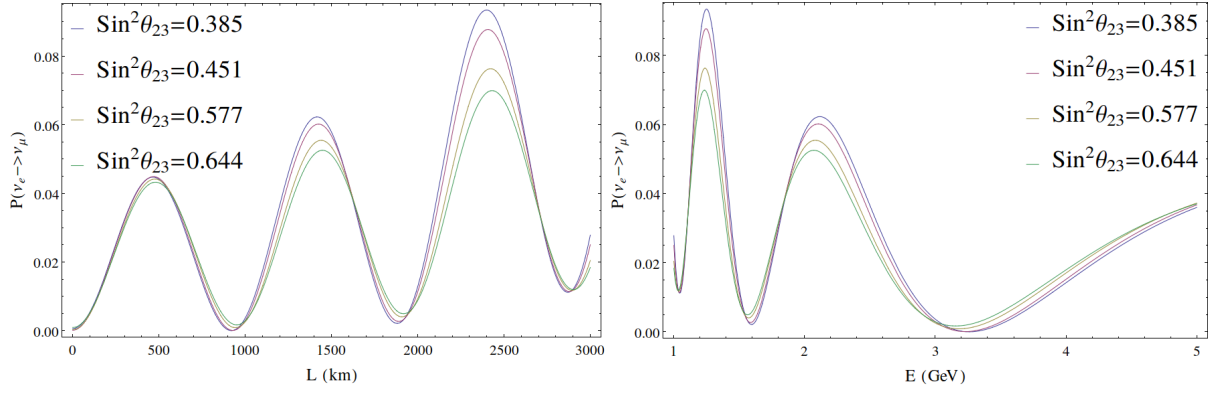


(a) Plot of probability against baseline.

(b) Plot of probability against energy

Figure 2.6: Plots of transition probabilities for varying values of θ_{13} within 3σ range, where $\sin^2 \theta_{13} = 0.0219$ is the best fit value according to [14].

It is clear from figures 2.5, 2.6 and 2.7 that at terrestrial distances and energies, probabilities are dominantly dependant on θ_{13} and θ_{23} while varying θ_{12} causes only a sub-dominant effect. This can be understood by again referring to equation 2.65, where it is easy to see that the dominant term doesn't contain θ_{12} , only the sub-dominant terms which are also dependant upon Δm_{21}^2 . It should be noted that the large contribution from θ_{23} is mainly due to the uncertainty in the octant, and once this is determined the contribution should be much smaller. Determination of the octant is expected to be obtained from the next generation of neutrino oscillation experiments. For example,



(a) Plot of probability against baseline.

(b) Plot of probability against energy

Figure 2.7: Plots of transition probabilities for varying values of θ_{23}^2 within 3σ range as given in [14]. As the octant of θ_{23} is unknown, there are two best fit values. $\sin^2 \theta_{23} = 0.451$ corresponds to the best fit value if $\theta_{23} < 45^\circ$, and $\sin^2 \theta_{23} = 0.577$ corresponds to the best fit value if $\theta_{23} > 45^\circ$.

a discussion on the sensitivity of LBNE to the octant can be found in section 5.4.4. From these plots it is clear that at terrestrial distances and energies, the probabilities are dominantly affected by δ_{CP} , Δm_{31}^2 , θ_{13} and θ_{23} , and contributions from the solar parameters, θ_{12} and Δm_{21}^2 are very much sub-dominant effects.

2.3 Matter Effects in ν Oscillations

The phenomenon of matter effects on neutrino oscillations was first studied in 1978 by Wolfenstein [34], and later by Mikheyev and Smirnov in 1986 [35] when trying to discover the source of the solar neutrino problem. The modification of the oscillation probabilities of neutrinos in matter can be compared to the phenomena of refraction of light through mediums of different refractive index. The effect is termed the *MSW effect* and is caused by coherent forward scattering of neutrinos in charged current processes due to electrons in the background medium. This causes the neutrino masses to be altered, exhibiting an effective mass, different to that of vacuum neutrinos. This can make a substantial difference to oscillation probabilities. Neutrinos passing through a medium are also subject to incoherent scatterings, although the number of these scatterings is usually small enough that they can be neglected.

2.3.1 Derivation of the Matter Potential

The matter potential can be derived from the effective charged current and neutral current weak interaction Lagrangians relevant to neutrinos, as done in reference [27]. For example, take the effective charged current Lagrangian for electrons,

$$\mathcal{L}_{eff}^{cc} = -\frac{G_F}{\sqrt{2}} j_{W\mu}^\dagger j_W^\mu, \quad (2.66)$$

where $j_W^\mu = 2\bar{\nu}_{eL}\gamma^\mu\ell_{eL}$ is the leptonic weak current for electrons. From this, the effective Hamiltonian can be read,

$$\mathcal{H}_{eff}^{cc}(x) = \frac{G_F}{\sqrt{2}} [\bar{\nu}_e(x)\gamma^\mu(1-\gamma^5)e(x)] [\bar{e}(x)\gamma_\mu(1-\gamma^5)\nu_e(x)]. \quad (2.67)$$

Here, the Hamiltonian for electron neutrinos has been picked out, as the number of electrons in the Earth massively outweighs the number of muons and tauons. By applying a Fierz transformation so that contributions to the Hamiltonian from the electrons and neutrinos are separated,

$$\mathcal{H}_{eff}^{cc}(x) = \frac{G_F}{\sqrt{2}} [\bar{\nu}_e(x)\gamma^\mu(1-\gamma^5)\nu_e(x)] [\bar{e}(x)\gamma_\mu(1-\gamma^5)e(x)], \quad (2.68)$$

where G_F is the Fermi constant. Now, by taking a statistical approach to the electron background and averaging,

$$\begin{aligned} \overline{\mathcal{H}_{eff}^{cc}}(x) &= \frac{G_F}{\sqrt{2}} \bar{\nu}_e(x)\gamma^\mu(1-\gamma^5)\nu_e(x) \int d^3p_e f(E_e, T) \\ &\times \frac{1}{2} \sum_{h_e=\pm 1} \langle e^-(p_e, h_e) | \bar{e}(x)\gamma_\mu(1-\gamma^5)e(x) | e^-(p_e, h_e) \rangle, \end{aligned} \quad (2.69)$$

where p_e and h_e are electron momentum and helicity respectively. The integration is over a statistical distribution of the temperature-dependent electron energy, $f(E_e, T)$, and is normalised to $\int d^3p_e f(E_e, T) = N_e V$ where N_e is the number density of electrons and V is the total volume of the area, so that $N_e V$ is the total number of electrons. The second line of the equation acts as an average over the helicities of the background electrons. By using the finite normalisation volume method outlined in appendix A, single particle electron states can be defined as

$$|e^-(p_e, h_e)\rangle = \frac{1}{\sqrt{2E_e V}} a_e^{h_e\dagger}(p_e), \quad (2.70)$$

where $a_e^{h_e\dagger}$ is the creation operator. By this definition, the average over the helicites can be rewritten

$$\begin{aligned} & \frac{1}{2} \sum_{h_e=\pm 1} \langle e^-(p_e, h_e) | \bar{e}(x) \gamma_\mu (1 - \gamma^5) e(x) | e^-(p_e, h_e) \rangle \\ &= \frac{1}{4E_e V} \sum_{h_e=\pm 1} \bar{u}_e^{h_e}(p_e) \gamma_\mu (1 - \gamma^5) u_e^{h_e}(p_e) \\ &= \frac{1}{4E_e V} \text{Tr} \left[\left(\sum_{h_e=\pm 1} u_e^{h_e}(p_e) \bar{u}_e^{h_e}(p_e) \right) \gamma_\mu (1 - \gamma^5) \right], \end{aligned} \quad (2.71)$$

where u is a Dirac spinor. Now, by using the sum rule, $\sum_{h_e=\pm 1} u(p_e, h_e) \bar{u}(p_e, h_e) = \not{p}_e + m_e$, and by using trace identities, this can be written as

$$\frac{1}{4E_e V} \text{Tr} \left[\left(\sum_{h_e=\pm 1} u_e^{h_e}(p_e) \bar{u}_e^{h_e}(p_e) \right) \gamma_\mu (1 - \gamma^5) \right] \quad (2.72)$$

$$= \frac{1}{4E_e V} \text{Tr} \left[(\not{p}_e + m_e) \gamma_\mu (1 - \gamma^5) \right] = \frac{p_{e\mu}}{E_e V}. \quad (2.73)$$

By plugging this in to equation 2.69 and performing the integration,

$$\begin{aligned} \int d^3 p_e f(E_e, T) \frac{\not{p}_e}{E_e} &= \int d^3 p_e f(E_e, T) \left(\frac{P_e^0 \cdot \gamma^0}{E_e} - \frac{\vec{p}_e \cdot \vec{\gamma}}{E_e} \right) \\ &= \int d^3 p_e f(E_e, T) \left(\gamma^0 - \frac{\vec{p}_e \cdot \vec{\gamma}}{E_e} \right) \\ &= N_e V \gamma^0, \end{aligned} \quad (2.74)$$

where the second term vanishes as it is odd under $\vec{p}_e \rightarrow -\vec{p}_e$, then finally, the averaged effective Hamiltonian can be written as

$$\overline{\mathcal{H}_{eff}^{cc}}(x) = V_{cc} \overline{\nu_{eL}}(x) \gamma^0 \nu_{eL}, \quad (2.75)$$

with

$$V_{cc} = \sqrt{2} G_F N_e \quad (2.76)$$

being the charged-current matter potential.

The same process can be followed starting from the effective neutral current Hamiltonian as defined in reference [27]:

$$\mathcal{H}_{eff}^{nc}(x) = \frac{G_F}{\sqrt{2}} \sum_{\alpha=e,\mu,\tau} [\overline{\nu_\alpha}(x) \gamma^\mu (1 - \gamma^5) \nu_\alpha(x)] \sum_f [\overline{f}(x) \gamma_\mu (g_V^f - g_A^f \gamma^5) f(x)] \quad (2.77)$$

where the sum over f is over neutrons, protons and electrons. The couplings g_V^f and g_A^f are the vector and axial couplings which are defined as combinations of the left and right couplings, g_L^f and g_R^f

$$g_L^f = I_3^f - q_f \sin^2 \theta_w \quad g_R^f = -q_f \sin^2 \theta_w \quad (2.78)$$

$$g_V^f = g_L^f + g_R^f = I_3^f - 2q_f \sin^2 \theta_w \quad g_A^f = g_L^f - g_R^f = I_3^f \quad (2.79)$$

where I_3 is the third component of the weak isospin, q_f is the electric charge of the fermion and θ_w is the Weinberg angle. Now, The same steps can be followed with little difference until the average over helicities is taken:

$$\begin{aligned} & \frac{1}{2} \sum_{h_f=\pm 1} \left\langle f(p_f, h_f) \left| \bar{f}(x) \gamma_\mu (g_V^f - g_A^f \gamma^5) f(x) \right| f(p_f, h_f) \right\rangle \\ &= \frac{1}{4E_f V} \sum_{h_f \neq 1} \overline{u_f^{h_f}}(p_f) \gamma_\mu (g_V^f - g_A^f \gamma^5) u_f^{h_f}(p_f) \\ &= \frac{1}{4E_f V} \text{Tr} \left[\left(\sum_{h_f=\pm 1} u_f^{h_f}(p_f) \overline{u_f^{h_f}}(p_f) \right) \gamma_\mu (g_V^f - g_A^f \gamma^5) \right] \\ &= \frac{1}{4E_f V} \text{Tr} \left[(\not{p}_f + m_e) \gamma_\mu (g_V^f - g_A^f \gamma^5) \right] = \frac{p_f \mu}{E_f V} g_V^f. \end{aligned} \quad (2.80)$$

which provides the neutral-current matter potential

$$V_{nc} = \sqrt{2} G_F N_f g_V^f \quad (2.81)$$

In low temperature, low density environments the contributions of protons and electrons largely cancel out due to electrical neutrality, and so the only term which is considered is the scattering due to neutrons. neutrons have the quark structure u-d-d, and the vector couplings for u-type and d-type can be found in the literature [27] to be

$$g_V^u = \frac{1}{2} - \frac{4}{3} \sin^2 \theta_w \quad g_V^d = -\frac{1}{2} + \frac{2}{3} \sin^2 \theta_w \quad (2.82)$$

so the coupling for neutrons can be found to be

$$g_V^n = g_V^u + 2g_V^d = -\frac{1}{2} \quad (2.83)$$

providing the neutral-current matter potential

$$V_{nc} = -\frac{1}{2} \sqrt{2} G_F N_n. \quad (2.84)$$

These two terms can be combined in to one *matter potential* term,

$$V_\rho = V_{cc}\delta_{\rho e} + V_{nc} = \sqrt{2}G_F \left(N_e\delta_{\rho e} - \frac{1}{2}N_n \right). \quad (2.85)$$

Here, the Kronecker delta acts to pick out only the interactions involving electron neutrinos. It should be noted that due to the low quantities of μ and τ particles in the Earth, ν_μ and ν_τ do not generally interact via charged current processes, and so the matter potential reduces to $V_{\mu,\tau} = \sqrt{2}G_F \left(-\frac{N_n}{2} \right)$ for these particles.

2.3.2 2- ν Oscillations in Matter

To set up the machinery for neutrino oscillations in matter, the Hamiltonian is first split in to a vacuum part (\mathcal{H}_0) and an interaction part (\mathcal{H}_I),

$$\mathcal{H} = \mathcal{H}_0 + \mathcal{H}_I, \quad (2.86)$$

where \mathcal{H}_0 is defined in the usual way, as outlined in equation 2.3, and \mathcal{H}_I is defined as

$$\mathcal{H}_I |\nu_\alpha\rangle = V_\alpha |\nu_\alpha\rangle. \quad (2.87)$$

From equation 2.5, it can be seen that in the Shröedinger picture, neutrinos obey

$$i\frac{d}{dt} |\nu_\alpha(t)\rangle = \mathcal{H} |\nu_\alpha(t)\rangle. \quad (2.88)$$

If a $\nu_\alpha \rightarrow \nu_\beta$ transition is then considered, this can be written as

$$\left\langle \nu_\beta \left| i\frac{d}{dt} \right| \nu_\alpha(t) \right\rangle = \langle \nu_\beta | \mathcal{H} | \nu_\alpha(t) \rangle \quad (2.89)$$

$$= \sum_k \langle \nu_k | U_{\beta k} E_k | \nu_\alpha(t) \rangle + \langle \nu_\beta | \mathcal{H}_I | \nu_\alpha(t) \rangle \quad (2.90)$$

$$= \sum_k \sum_\eta \langle \nu_\eta | U_{\beta k} E_k U_{k\eta}^* | \nu_\alpha(t) \rangle + \langle \nu_\beta | V_\beta | \nu_\alpha(t) \rangle \quad (2.91)$$

$$= \sum_\eta \left\langle \nu_\eta \left| \sum_k U_{\beta k} E_k U_{k\eta}^* + V_\beta \delta_{\beta\eta} \right| \nu_\alpha(t) \right\rangle, \quad (2.92)$$

where in the first step, the Hamiltonian has been written in its constituent parts, and the flavour states have been written as a superposition of massive states. From here, the ultrarelativistic approximation is taken in which the dispersion relation, $E_k = E + \frac{m_k^2}{2E}$, along with $p \simeq E$ and $t \simeq L$ are used. If, at the same time, the definition of V_β from

equation 2.85 is used, then the following is found:

$$\begin{aligned}
& \left\langle \nu_\beta \left| i \frac{d}{dt} \right| \nu_\alpha(t) \right\rangle \\
&= \sum_{\eta} \left\langle \nu_\eta \left| \sum_k U_{\beta k} \left(E + \frac{m_k^2}{2E} \right) U_{k\eta}^* + V_{cc} \delta_{\beta e} \delta_{\beta\eta} + V_{nc} \delta_{\beta\eta} \right| \nu_\alpha(t) \right\rangle \\
&= \sum_{\eta} \left\langle \nu_\eta \left| \sum_k \left(U_{\beta k} E U_{k\eta}^* + U_{\beta k} \frac{m_k^2}{2E} U_{k\eta}^* \right) + V_{cc} \delta_{\beta e} \delta_{\beta\eta} + V_{nc} \delta_{\beta\eta} \right| \nu_\alpha(t) \right\rangle.
\end{aligned} \tag{2.93}$$

By writing $m_k^2 = \frac{\Delta m_{k1}^2}{2E} + \frac{m_1^2}{2E}$, where $\Delta m_{k1}^2 = m_k^2 - m_1^2$, this can now be written as

$$\begin{aligned}
\left\langle \nu_\beta \left| i \frac{d}{dt} \right| \nu_\alpha(t) \right\rangle &= \left\langle \nu_\beta \left| E + \frac{m_1^2}{2E} + V_{nc} \right| \nu_\alpha(t) \right\rangle \\
&\quad + \sum_{\eta} \left\langle \nu_\eta \left| \sum_k U_{\beta k} \frac{\Delta m_{k1}^2}{2E} U_{k\eta}^* + V_{cc} \delta_{\beta e} \delta_{\beta\eta} \right| \nu_\alpha(t) \right\rangle.
\end{aligned} \tag{2.94}$$

The first term here contributes a global phase which is common to all flavours, and so is irrelevant for neutrino oscillations and can be safely neglected. This means that neutral current interactions do not have any effect on neutrino oscillations. This gives rise to the equation

$$\left\langle \nu_\beta \left| i \frac{d}{dt} \right| \nu_\alpha(t) \right\rangle = \sum_{\eta} \left\langle \nu_\eta \left| \sum_k U_{\beta k} \frac{\Delta m_{k1}^2}{2E} U_{k\eta}^* + V_{cc} \delta_{\beta e} \delta_{\beta\eta} \right| \nu_\alpha(t) \right\rangle, \tag{2.95}$$

where the part between the neutrino states is the Hamiltonian. The equation can be written in matrix form as

$$\begin{aligned}
i \frac{d}{dx} \begin{pmatrix} \nu_\alpha \\ \nu_\beta \end{pmatrix} &= \left[\frac{1}{2E} \begin{pmatrix} \cos \theta & \sin \theta \\ -\sin \theta & \cos \theta \end{pmatrix} \begin{pmatrix} 0 & 0 \\ 0 & \Delta m_{21}^2 \end{pmatrix} \begin{pmatrix} \cos \theta & -\sin \theta \\ \sin \theta & \cos \theta \end{pmatrix} \right. \\
&\quad \left. + \begin{pmatrix} V_{cc} & 0 \\ 0 & 0 \end{pmatrix} \right] \begin{pmatrix} \nu_1 \\ \nu_2 \end{pmatrix}.
\end{aligned} \tag{2.96}$$

By defining $A_{cc} = 2EV_{cc}$, the Hamiltonian can be rewritten as

$$\mathcal{H} = \frac{1}{2E} \begin{pmatrix} s^2 \theta \Delta m_{21}^2 + A_{cc} & s \theta c \theta \Delta m_{21}^2 \\ s \theta c \theta \Delta m_{21}^2 & c^2 \theta \Delta m_{21}^2 \end{pmatrix}, \tag{2.97}$$

and by trigonometric identities, this can be written as

$$\begin{pmatrix} -\cos(2\theta)\frac{\Delta m_{21}^2}{4E} + \frac{A_{cc}}{2E} & \sin(2\theta)\frac{\Delta m_{21}^2}{4E} \\ \sin(2\theta)\frac{\Delta m_{21}^2}{4E} & -\cos(2\theta)\frac{\Delta m_{21}^2}{4E} \end{pmatrix}, \quad (2.98)$$

where the common terms on the diagonal have been neglected as they contribute a global phase. θ_m is the mixing angle in matter defined by

$$\tan(2\theta_m) = \frac{\sin(2\theta)\frac{\Delta m_{21}^2}{2E}}{\cos(2\theta)\frac{\Delta m_{21}^2}{2E} + V_{cc}}. \quad (2.99)$$

By use of the characteristic equation the eigenvalues can be found to be

$$\lambda_{\mp} = \frac{1}{2}V_{cc} \mp \sqrt{\frac{1}{4}V_{cc}^2 - V_{cc}\frac{\Delta m_{21}^2}{4E}\cos(2\theta) + \left(\frac{\Delta m_{21}^2}{4E}\right)^2}, \quad (2.100)$$

and these can replace the eigenvalues in the 2-neutrino vacuum probability, where the eigenvalues were $E_k - E_j \simeq \frac{\Delta m_{kj}^2}{2E}$,

$$P_{\nu_\alpha \rightarrow \nu_\beta}(t) = \sin^2(2\theta_m) \sin^2\left((\lambda_+ - \lambda_-)\frac{L}{2}\right). \quad (2.101)$$

By plotting this as done in figure 2.8, the effects of matter can be observed. As is easily seen from the plot, changing the density of the matter changes the phase and reduces the probability, acting to suppress neutrino oscillations.

By explicitly calculating $\lambda_+ - \lambda_-$,

$$\lambda_+ - \lambda_- = \sqrt{\left(\frac{\Delta m_{21}^2}{2E}\cos(2\theta) - \sqrt{2}G_F N_e\right)^2 + \left(\frac{\Delta m_{21}^2}{2E}\right)^2 \sin^2(2\theta)}, \quad (2.102)$$

It can be seen that there are naively three cases for matter effects on neutrino oscillations depending on the density of material through which the neutrino is travelling.

i Vacuum limit

$\sqrt{2}G_F N_e \ll \frac{\Delta m_{21}^2}{2E}\cos(2\theta)$, in which the mass effects are negligible and the mixing angle in matter approaches the vacuum mixing angle, $\tan(2\theta_m) \simeq \tan(2\theta)$

ii Matter dominates

$\sqrt{2}G_F N_e \gg \frac{\Delta m_{21}^2}{2E}\cos(2\theta)$, when the matter is extremely dense the matter completely suppresses the oscillations, the mixing angle tends to zero $\tan(2\theta_m) \rightarrow 0$ and so the probability tends to zero $P \rightarrow 0$

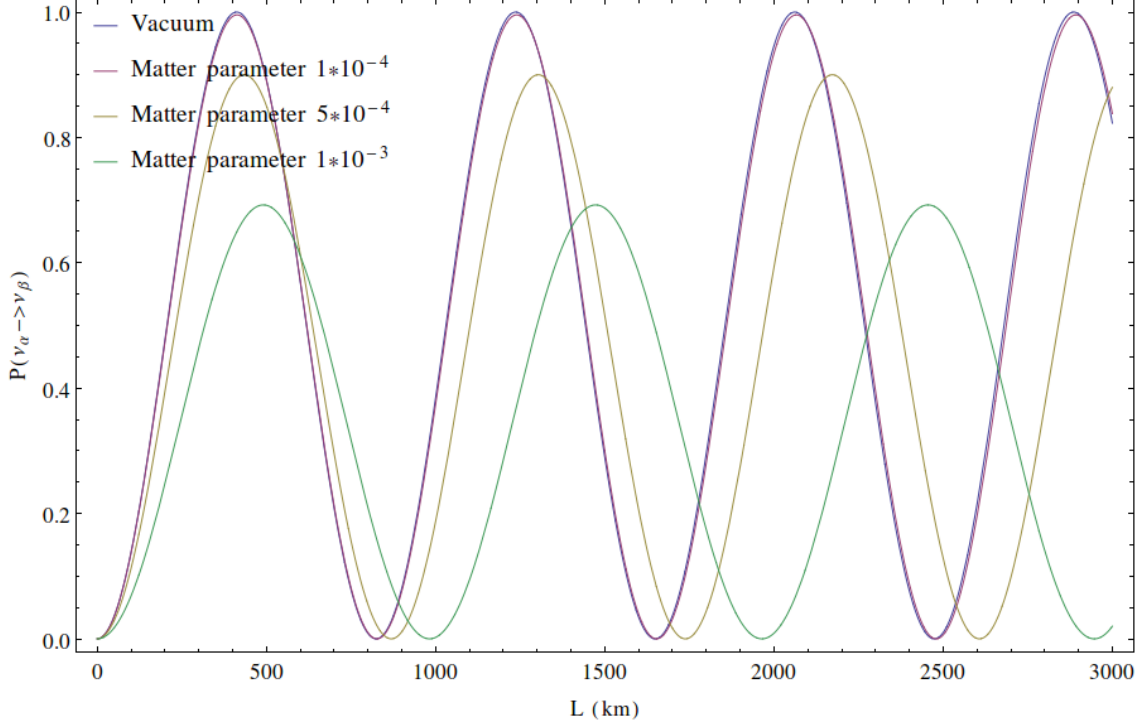


Figure 2.8: A plot of probability for the two neutrino case in matter. The probability is now dependant on five parameters, the values of the mixing angle and the mass-squared difference, the length of baseline and beam energy which are chosen in experiments, and the density of the matter. The parameters are set to the same values as in figure 2.1, and the matter parameter V_{cc} takes several values as stated in the figure. Again these choices are arbitrary due to this being the unphysical 2-neutrino system.

iii Resonance

$\sqrt{2}G_F N_e = \frac{\Delta m_{21}^2}{2E} \cos(2\theta)$, In this case the mixing angle tends to maximal, $\tan(2\theta_m) \rightarrow \infty$, $\theta_m \rightarrow \pi/4$, so the matter acts to enhance the probability.

2.3.3 3- ν Oscillations in Matter

To calculate the three neutrino oscillation probabilities in matter, an equation similar to equation 2.96, but for three neutrinos can be written down,

$$i \frac{d}{dx} \begin{pmatrix} \nu_e \\ \nu_\mu \\ \nu_\tau \end{pmatrix} = \mathcal{H}_F \begin{pmatrix} \nu_e \\ \nu_\mu \\ \nu_\tau \end{pmatrix}, \quad (2.103)$$

where

$$\mathcal{H}_F \equiv \frac{1}{2E} \left[U \begin{pmatrix} 0 & 0 & 0 \\ 0 & \Delta m_{21}^2 & 0 \\ 0 & 0 & \Delta m_{31}^2 \end{pmatrix} U^\dagger + 2E \begin{pmatrix} V_{cc} & 0 & 0 \\ 0 & 0 & 0 \\ 0 & 0 & 0 \end{pmatrix} \right], \quad (2.104)$$

is the matrix that needs to be diagonalised. Here U is the PMNS matrix as defined in equation 2.61. Exact diagonalisation of this matrix has been carried out in reference [36], however this dissertation will follow the perturbative approach set out in reference [37].

In general, there are two methods to approach this perturbatively. In the first method, only Δm_{21}^2 is considered to be small, and perturbations at each order of Δm_{21}^2 can be calculated. This is what will be carried out in this section. Secondly, an expansion can be made in θ_{13} as well as Δm_{21}^2 , using either “ ϵ ” perturbation theory as presented in reference [37] or “ $\sqrt{\epsilon}$ ” perturbation theory as presented in [33]. $\sqrt{\epsilon}$ perturbation theory calculations can be found in appendix B.2, where the small parameters have been kept to $\mathcal{O}(\epsilon^2)$.

Initially, only Δm_{21}^2 is expanded. It is proposed that a zeroth order Δm_{31}^2 component can be computed and the contribution from the small mass-difference can be treated as a first order correction. This takes the treatment shown in appendix B.1 further by including first order corrections in Δm_{21}^2 .

To begin, the small mass difference is first turned off so that the zeroth order part, which only contains terms from the dominant mass squared difference, can be calculated. This is done by diagonalisation of

$$M^0 \equiv \underbrace{\frac{1}{2E} U \begin{pmatrix} 0 & 0 & 0 \\ 0 & 0 & 0 \\ 0 & 0 & \Delta m_{31}^2 \end{pmatrix} U^\dagger}_{M^2} + \underbrace{\begin{pmatrix} V_{cc} & 0 & 0 \\ 0 & 0 & 0 \\ 0 & 0 & 0 \end{pmatrix}}_A. \quad (2.105)$$

U is composed of three rotation matrices $U = U_{23}U_{13}U_{12}$, and by writing out equation 2.105 explicitly it can be noted that U_{12} commutes with M^2 , and so disappears by unitarity, and U_{23} commutes with A which allows the evolution equation in equation 2.104 in to be written as

$$i \frac{d}{dx} \begin{pmatrix} \nu_1^0 \\ \nu_2^0 \\ \nu_3^0 \end{pmatrix} = \frac{1}{2E} \left[U_{13} \begin{pmatrix} 0 & 0 & 0 \\ 0 & 0 & 0 \\ 0 & 0 & \Delta m_{31}^2 \end{pmatrix} U_{13}^\dagger + 2E \begin{pmatrix} V_{cc} & 0 & 0 \\ 0 & 0 & 0 \\ 0 & 0 & 0 \end{pmatrix} \right] \begin{pmatrix} \nu_1^0 \\ \nu_2^0 \\ \nu_3^0 \end{pmatrix}, \quad (2.106)$$

where the new basis has been defined to be

$$\begin{pmatrix} \nu_1^0 \\ \nu_2^0 \\ \nu_3^0 \end{pmatrix} = U_{23}^\dagger \begin{pmatrix} \nu_e \\ \nu_\mu \\ \nu_\tau \end{pmatrix}. \quad (2.107)$$

By use of the characteristic equation, and then returning to the flavour basis, the diagonalised matrix to zeroth order can be found to be

$$M_\mp^0 = U_{23} U_{13}^{M\mp} \begin{pmatrix} \frac{\Delta_{31} \pm V_{cc} - B_\mp}{2} & 0 & 0 \\ 0 & 0 & 0 \\ 0 & 0 & \frac{\Delta_{31} \pm V_{cc} + B_\mp}{2} \end{pmatrix} U_{13}^{M\mp\dagger} U_{23}^\dagger, \quad (2.108)$$

in the flavour basis where the diagonals are the zeroth order eigenvalues, $\lambda_1^0, \lambda_2^0, \lambda_3^0, \Delta_{ij} = \frac{\Delta m_{ij}^2}{2E}$, and $U_{13}^{M\mp} = U_{13}(\theta_{M\mp})$ where $\theta_{M\mp}$ is defined by

$$\tan(2\theta_{M\mp}) \equiv \frac{\Delta_{31} \sin(2\theta_{13})}{\Delta_{31} \cos(2\theta_{13}) \mp V_{cc}}, \quad (2.109)$$

and is to be taken in the first quadrant if denominator is positive, or the second quadrant if the denominator is negative. B_\mp is here defined to be

$$B_\mp \equiv \sqrt{[\Delta_{31} \cos(2\theta_{13}) \mp V_{cc}]^2 + [\Delta_{31} \sin(2\theta_{13})]^2}. \quad (2.110)$$

If the perturbation is now turned on, the evolution equation in equation 2.104 becomes

$$\begin{aligned} i \frac{d}{dx} \begin{pmatrix} \nu_e \\ \nu_\mu \\ \nu_\tau \end{pmatrix} &= \left[M_\mp^0 + U \begin{pmatrix} 0 & 0 & 0 \\ 0 & \Delta_{21} & 0 \\ 0 & 0 & 0 \end{pmatrix} U^\dagger \right] \begin{pmatrix} \nu_e \\ \nu_\mu \\ \nu_\tau \end{pmatrix} \\ &= U_{23} U_{13}^{M\mp} \left[\begin{pmatrix} \lambda_1^0 & 0 & 0 \\ 0 & \lambda_2^0 & 0 \\ 0 & 0 & \lambda_3^0 \end{pmatrix} \right. \\ &\quad \left. + U_{13}^{M\mp\dagger} U_{23}^\dagger U \begin{pmatrix} 0 & 0 & 0 \\ 0 & \Delta_{21} & 0 \\ 0 & 0 & 0 \end{pmatrix} U^\dagger U_{23} U_{13}^{M\mp} \right] U_{13}^{M\mp\dagger} U_{23}^\dagger \begin{pmatrix} \nu_e \\ \nu_\mu \\ \nu_\tau \end{pmatrix}. \end{aligned} \quad (2.111)$$

By pre-multiplying both sides of this equation by $U_{13}^{M\mp\dagger} U_{23}^\dagger$, the first order mass basis can

then be defined to be

$$\begin{pmatrix} \nu_1^1 \\ \nu_2^1 \\ \nu_3^1 \end{pmatrix} = U_{13}^{M\mp\dagger} U_{23}^\dagger \begin{pmatrix} \nu_e \\ \nu_\mu \\ \nu_\tau \end{pmatrix}, \quad (2.112)$$

and now by diagonalising the first order matrix by use of the characteristic equation, the first order eigenvalues can be found to be

$$\begin{aligned} \lambda_1^1 &= \lambda_1^0 + s_{12}^2 \Delta_{21} \cos^2 \bar{\theta}_{M\mp}, \\ \lambda_2^1 &= \lambda_2^0 + c_{12}^2 \Delta_{21}, \\ \lambda_3^1 &= \lambda_3^0 s_{12}^2 \Delta_{21} \sin^2 \bar{\theta}_{M\mp}, \end{aligned} \quad (2.113)$$

where $\bar{\theta}_{M\mp} = \theta_{13} - \theta_{M\mp}$. From this it is possible to calculate the eigenvectors of the system, which are

$$\begin{aligned} \nu_1^1 &= \left(1, \frac{\Delta_{21} \sin(2\theta_{12}) \cos \bar{\theta}_{M\mp}}{\Delta_{31} + A_{cc} - B_{\mp}}, \frac{\Delta_{21} s_{12}^2 \sin(2\bar{\theta}_{M\mp}) e^{\mp i\delta}}{2B_{\mp}} \right), \\ \nu_2^1 &= \left(-\frac{\Delta_{21} \sin(2\theta_{12}) \cos \bar{\theta}_{M\mp}}{\Delta_{31} + A_{cc} - B_{\mp}}, 1, \frac{\Delta_{21} \sin(2\theta_{12}) \sin(\bar{\theta}_{M\mp}) e^{\mp i\delta}}{\Delta_{31} + A_{cc} + B_{\mp}} \right), \\ \nu_3^1 &= \left(-\frac{\Delta_{21} s_{12}^2 \sin(2\bar{\theta}_{M\mp}) e^{\pm i\delta}}{2B_{\mp}}, -\frac{\Delta_{21} \sin(2\theta_{12}) \sin(\bar{\theta}_{M\mp}) e^{\pm i\delta}}{\Delta_{31} + A_{cc} + B_{\mp}}, 1 \right). \end{aligned} \quad (2.114)$$

The matrix gained from putting these eigenvectors together acts as the mixing matrix for the system, allowing the transition probabilities to be derived. For example the transition

probability for $\nu_e \rightarrow \nu_\mu$ is given by

$$\begin{aligned}
P(\nu_e \rightarrow \nu_\mu) = & \sin^2(\theta_{23}) \sin^2(2\theta_{M_\mp}) \sin^2\left(\frac{B_\mp L}{2}\right) \\
& - \sin^2(\theta_{23}) \sin^2(\theta_{12}) \left[\sin(4\theta_{M_\mp}) \sin(2\bar{\theta}_{M_\mp}) \sin^2\left(\frac{B_\mp L}{2}\right) \frac{\Delta_{21}}{B_\mp} \right. \\
& \quad \left. + \sin^2(2\theta_{M_\mp}) \cos(2\bar{\theta}_{M_\mp}) \sin(B_\mp L) \frac{\Delta_{21} L}{2} \right] \\
& + \sin(2\theta_{12}) \sin(2\theta_{23}) \sin(2\theta_{M_\mp}) \sin\left(\frac{B_\mp L}{2}\right) \Delta_{21} \\
& \quad \times \left[\sin\left(\frac{\lambda_1^{(0)} L}{2}\right) \cos\left(\pm\delta - \frac{\lambda_3^{(0)} L}{2}\right) \right. \\
& \quad \times \left(\frac{\cos(\theta_{M_\mp}) \cos(\bar{\theta}_{M_\mp})}{\lambda_1^{(0)}} - \frac{\sin(\theta_{M_\mp}) \sin(\bar{\theta}_{M_\mp})}{\lambda_3^{(0)}} \right) \\
& \quad \left. - \sin(\theta_{M_\mp}) \sin(\bar{\theta}_{M_\mp}) \cos(\delta) \sin\left(\frac{B_\mp L}{2}\right) \frac{1}{\lambda_3^{(0)}} \right]. \quad (2.115)
\end{aligned}$$

This probability can be further improved upon by expanding in θ_{13} as well as Δ_{21} . This has been performed in reference [37] up to $\mathcal{O}(\Delta_{21}^2 \theta_{13}^0)$, $\mathcal{O}(\Delta_{21} \theta_{13})$ and $\mathcal{O}(\Delta_{21}^0 \theta_{13}^2)$, i.e. up to second order. This yields the probability

$$\begin{aligned}
P_{\nu_e \rightarrow \nu_\mu} = & s_{23}^2 \sin^2 2\theta_{13} \left(\frac{\Delta_{31}}{\tilde{B}_\mp} \right)^2 \sin^2\left(\frac{\tilde{B}_\mp L}{2}\right) \\
& + c_{23}^2 \sin^2 2\theta_{12} \left(\frac{\Delta_{21}}{V_{cc}} \right)^2 \sin^2\left(\frac{V_{cc} L}{2}\right) \\
& + \tilde{J} \frac{\Delta_{21}}{V_{cc}} \frac{\Delta_{31}}{\tilde{B}_\mp} \sin\left(\frac{V_{cc} L}{2}\right) \sin\left(\frac{\tilde{B}_\mp L}{2}\right) \cos\left(\pm\delta - \frac{\Delta_{31} L}{2}\right)
\end{aligned} \quad (2.116)$$

where $\tilde{B}_\mp \equiv |V_{cc} \mp \Delta_{31}|$ and $\tilde{J} = c_{13} \sin 2\theta_{12} \sin 2\theta_{23} \sin 2\theta_{13}$ is the Jarlskog coefficient. This is valid for relatively small values of θ_{13} , however due to the discovery of a relatively large value of θ_{13} which is close to the Chooz limit of $\theta_{13} \simeq 10^\circ$, higher order corrections are necessary to properly approximate the true probability. This has been carried by Asano and Minakata in reference [33], where perturbations are kept up to the fourth order. These calculations are carried out in appendix B.2, and the probability is found

to be:

$$\begin{aligned}
P_{\nu_e \rightarrow \nu_\mu} = & 4s_{23}^2 s_{13} \frac{1}{(1 - r_A)^2} \sin^2 \left(\frac{(1 - r_A)\Delta_{31}L}{2} \right) \\
& + 8J_r \frac{r_\Delta}{r_A(1 - r_A)} \cos \left(\delta - \frac{\Delta_{31}L}{2} \right) \sin \left(\frac{r_A\Delta_{31}L}{2} \right) \sin \left(\frac{(1 - r_A)\Delta_{31}L}{2} \right) \\
& + 4c_{23}^2 c_{12}^2 s_{12}^2 \left(\frac{r_\Delta}{r_A} \right)^2 \sin^2 \left(\frac{r_A\Delta_{31}L}{2} \right) \\
& - 4s_{23}^2 \left[s_{13}^2 \frac{(1 + r_A)^2}{(1 - r_A)^4} - 2s_{12}^2 s_{13}^2 \frac{r_\Delta r_A}{(1 - r_A)^3} \right] \sin^2 \left(\frac{(1 - r_A)\Delta_{31}L}{2} \right) \\
& + 2s_{23}^2 \left[2s_{13}^4 \frac{r_A}{(1 - r_A)^3} - s_{12}^2 s_{13}^2 \frac{r_\Delta}{(1 - r_A)^2} \right] \Delta_{31}L \sin((1 - r_A)\Delta_{31}L),
\end{aligned} \tag{2.117}$$

where $r_A = \frac{2EV_{cc}}{\Delta m_{31}^2}$ and $r_\Delta = \frac{\Delta m_{21}^2}{\Delta m_{31}^2}$.

Each of the approximations (the Cervera et al. and the Asano-Minakata) has been plotted against the true probability, which has been produced by GLoBES software, in figure 2.9. As can be seen from the plot, the Asano-Minakata probability approximates the true probability far more closely than the Cervera et al. probability, meaning that the higher order corrections make a significant difference to the probability.

Matter Effects in the Determination of δ_{CP}

Having now calculated several analytical probabilities, it is now useful to investigate the effects of the matter density on neutrino oscillations. The treatment in this section is only for cases of constant density. For cases with varying density a more sophisticated numerical approach is required such as using the General Long Baseline Experiment Simulator (GLoBES) [38, 39].

Matter effects induce a CP-odd asymmetry between neutrinos and anti-neutrinos, that is to say that it differentiates between them. This is because the background is CP and CPT violating in the respect that there are no positrons, anti-protons or anti-neutrons in the Earth and so neutrinos are granted a probability enhancement, whilst anti-neutrinos transition probabilities are suppressed (for the normal hierarchy, this is inverted for inverted hierarchy) [40]. Measurements of the true value of the CP violating phase are made more complicated by this interference. With the aim of discovering the value of the CP violating phase, two asymmetries may be defined, as in reference [41].

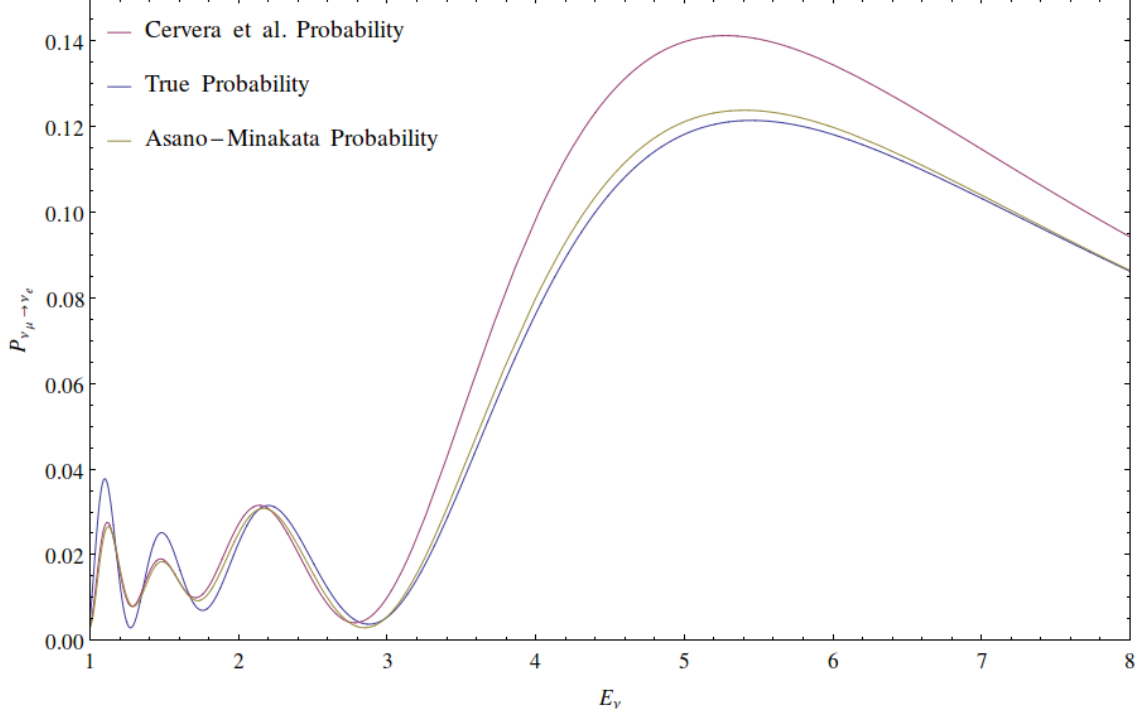


Figure 2.9: A comparison of the true oscillation probability and the oscillation probability as derived in [37], for a baseline $L=4000\text{km}$ with a matter density $\rho = 3.6\text{g/cm}^3$. The true probability was produced numerically using the GLoBES package.

The first is taken to be the CP asymmetry in a vacuum, which purely depends on δ_{CP} , the neutrino energy and the baseline of the experiment,

$$\mathcal{A}_{CP}^{vac}(\delta_{CP}) = \left| \frac{P^{vac}(\nu) - P^{vac}(\bar{\nu})}{P^{vac}(\nu) + P^{vac}(\bar{\nu})} \right|, \quad (2.118)$$

where the bars denote the absolute magnitude, and the second is taken to be the asymmetry due to the matter effects, taken at a constant value of δ_{CP} ,

$$\mathcal{A}_{CP}(\rho) = \left| \frac{P^{mat}(\nu) - P^{mat}(\bar{\nu})}{P^{mat}(\nu) + P^{mat}(\bar{\nu})} \right|. \quad (2.119)$$

By plotting these asymmetries as in figure 2.10, the effects of the matter density can be observed. The asymmetries range between zero and one, where a value of zero indicates complete insensitivity to CP violation at the related energy and baseline, and a value of 1 indicates maximum sensitivity to CP violation. It is easy to see that at around the first maximum, the asymmetry due to matter effects tends to dominate, and becomes less dominant at higher order maximum. It is of particular interest that the effects of CP violation grow as the order of the maxima grow, such that the second order maximum is

more sensitive to CP violation than the first maximum.

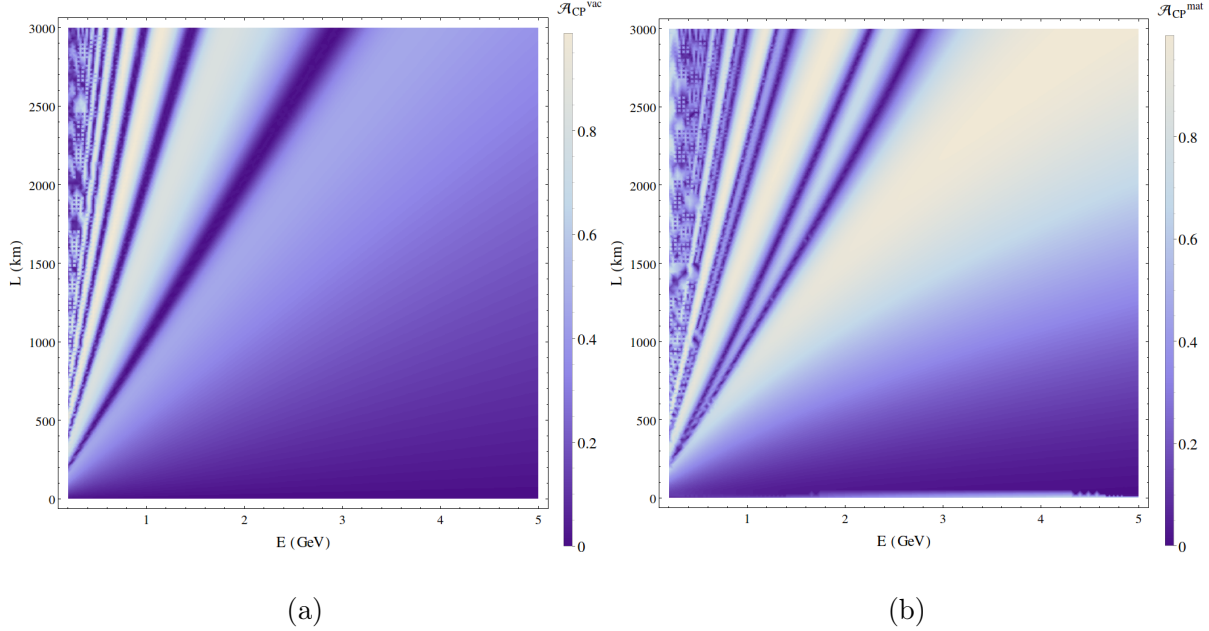


Figure 2.10: The CP asymmetry in the L-E plane for (a) a vacuum and (b) in the case of constant-density matter, with $\delta_{CP} = 270^\circ$ in both diagrams, and the matter density, $\rho = 2.8 \text{ g/cm}^3$

Varying the Matter Potential

Although in physical experiments it is impossible to change the density of the material through which the neutrino travels, showing how the oscillation probability varies as a function of the matter potential provides good physical intuition.

The plot in figure 2.11 shows how the value of the matter potential can either provide a suppression or enhancement of the probability. This is essentially the same idea as presented in section 2.3.2. The matter densities at which resonance between the eigenvalues occurs can be shown graphically, as in 2.12. The points at which the eigenvalues approach their closest define the resonances.

The contribution of the matter potential naturally varies dependant on the neutrino energy and the baseline which is chosen, as can be seen from figure 2.13. These plots reinforce the point made in section 2.3.2 that the matter density can act to suppress or enhance the transition probabilities. Plots like those in figures 2.10 and 2.13 are incredibly useful when planning neutrino oscillation experiments on the Earth, as knowledge of the density of the Earth and the expected energy range of the produced neutrinos

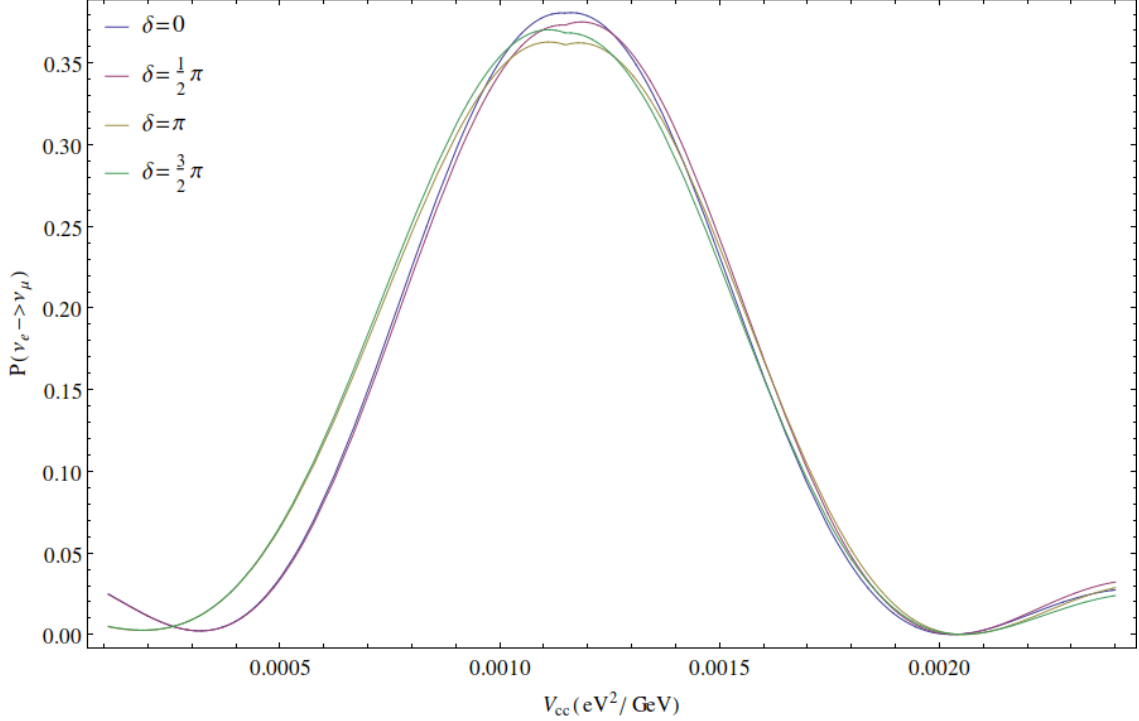


Figure 2.11: This plot shows how an oscillation probability is affected by the matter potential when the neutrino energy and the baseline are kept constant. Here the slight dip in the peak is caused by the definition of the matter mixing angle switching from the first quadrant to the second quadrant due to the denominator changing sign.

then allow a baseline to be chosen which either maximises the probability of oscillations occurring, or maximises the sensitivity to CP violating effects. Alternatively, should the baseline already be set, then these plots allow an appropriate energy range to be chosen.

2.4 Degeneracies

Although many of the oscillation parameters are measured with precision, there are still several open questions in the field of neutrino physics. There are several *degeneracies* which open up more than one region of allowed values. Together, the three degeneracies — hierarchy, octant and intrinsic — create an eight-fold parameter degeneracy in the neutrino sector [42]. It is expected that the next generation of neutrino oscillation experiments should break this degeneracy to some extent.

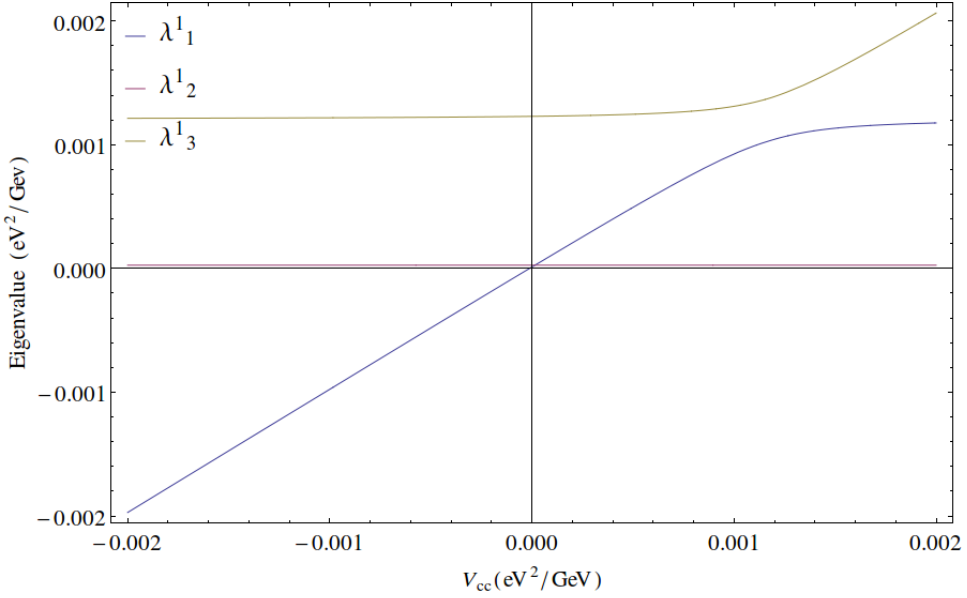


Figure 2.12: The values of the energy eigenvalues, which can be seen to be effective mass-squared differences in matter. The two closest approaches define the resonance peaks.

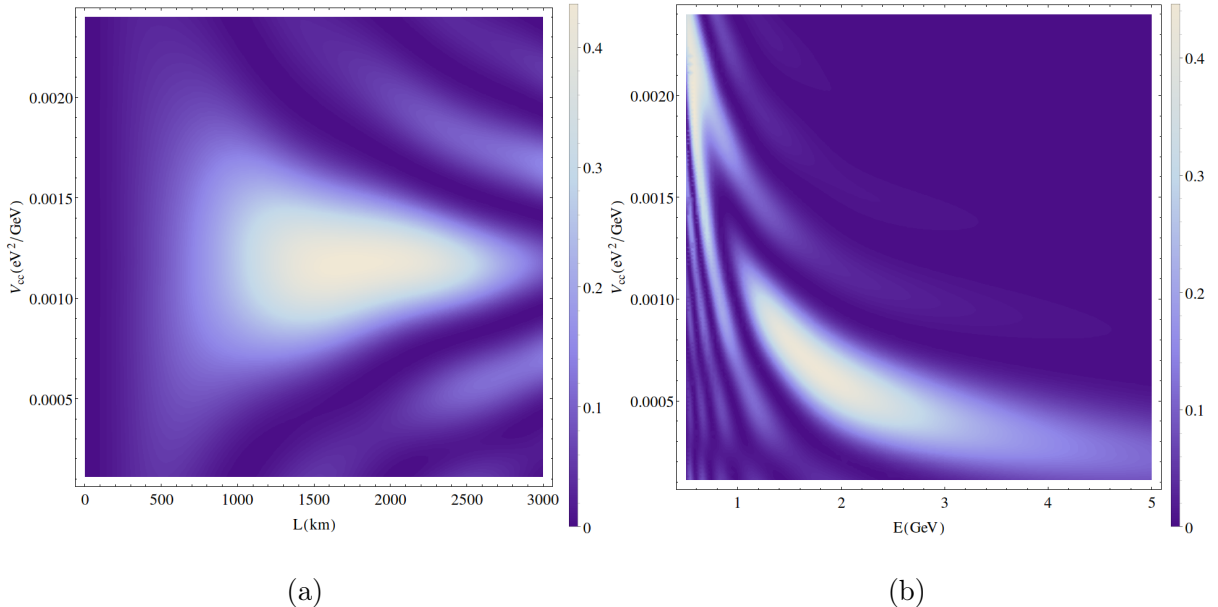


Figure 2.13: Plots showing the dependency of the oscillation probability on the matter density versus the baseline, with $E = 1$ GeV (a) and the energy with $L = 3000$ km (b). The oscillation parameters are assumed to be their best fit values as given in section 3.2 and δ_{CP} is taken to be zero.

2.4.1 Hierarchy Degeneracy

The hierarchy degeneracy relates to the unknown sign of Δm_{31}^2 , giving rise to two distinct regions known as normal hierarchy, $\Delta m_{31}^2 > 0$, and inverted hierarchy, $\Delta m_{31}^2 < 0$. This

is shown graphically in figure 2.14. Previous plots have always assumed normal hierarchy for the sake of brevity. The hierarchy degeneracy can easily be understood by looking at

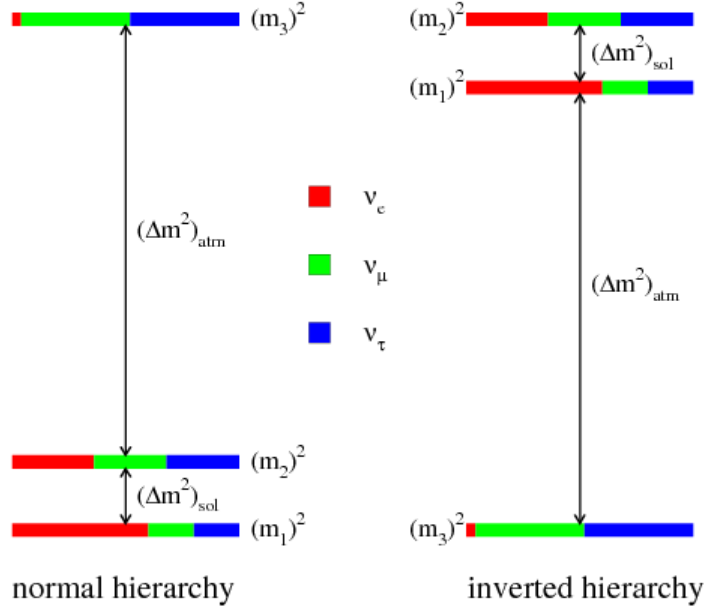


Figure 2.14: Graphical representation of the normal and inverted hierarchies. The colours represent the fractions of each flavour contained within each massive eigenstate. It should be noted that $\Delta m_{sol}^2 = \Delta m_{21}^2$ and $\Delta m_{atm}^2 = \Delta m_{31}^2$. Plot taken from reference [43].

the probability presented in equation 2.116. Only two terms are dependant upon Δm_{31}^2 . The dependence upon Δm_{31}^2 in the dominant term is contained within a sin squared term which means that it is insensitive to the sign of its argument. This means that the sign of Δm_{31}^2 is a sub-dominant effect and therefore difficult to measure. The sub-dominant term also contains dependence upon the CP violating phase which is unbounded, meaning that differing signs of Δm_{31}^2 are preferred depending upon the value of δ_{CP} .

2.4.2 Intrinsic Degeneracy

The intrinsic degeneracy is sometimes referred to as the $(\delta_{CP}, \theta_{13})$ degeneracy due to the existence of degenerate solutions for different values of δ_{CP} and θ_{13} ,

$$P(\theta_{13}, \delta) = P(\bar{\theta}_{13}, \bar{\delta}). \quad (2.120)$$

These degenerate solutions are known as the *intrinsic clones* of the true solution [44]. Although θ_{13} has been precisely determined, somewhat breaking the degeneracy, there is still complete uncertainty in the value of δ_{CP} at 3σ .

2.4.3 Octant Degeneracy

The octant degeneracy deals with the value of θ_{23} , and was touched upon briefly in 2.2.2. It is currently unknown whether this mixing angle is maximal ($\theta_{23} = \pi/4$) as is preferred by analysis of SK data, or if it is non-maximal as favoured by MINOS data. Assuming that the value is non-maximal, it is unknown whether the true value is in the lower *octant*, $\theta_{23} < \pi/4$, or the higher octant, $\theta_{23} > \pi/4$. This can be understood theoretically by looking at the ν_μ survival probability in vacuum,

$$P_{\nu_\mu \rightarrow \nu_\mu}^{vac} = 1 - c_{13}^2 \sin^2(2\theta_{23}) \sin^2\left(\frac{\Delta m_{31}^2}{4E} L\right) - s_{23}^4 \sin^2(2\theta_{13}) \sin^2\left(\frac{\Delta m_{31}^2}{4E} L\right) \quad (2.121)$$

which has been calculated in the one mass-squared dominance case (see appendix B.1). The second term on the RHS here is the dominant term, and as such, μ survival probabilities are primarily sensitive to terms proportional to $\sin^2(2\theta_{23})$. In this case, the same probability can be obtained from θ_{23} and $\pi/2 - \theta_{23}$, i.e. $P(\theta_{23}) = P(\pi/2 - \theta_{23})$.

The octant degeneracy is expected to be lifted by the study of disappearance events, i.e. $\nu_\mu \rightarrow \nu_e$ transitions. Using the same approximation as earlier (see appendix B.1), the probability can be found to be

$$P_{\nu_\mu \rightarrow \nu_e}^{vac} = s_{23}^2 \sin^2(2\theta_{13}) \sin^2\left(\frac{\Delta m_{31}^2}{4E} L\right), \quad (2.122)$$

which is not sensitive to $\sin^2(2\theta_{23})$, but $\sin^2(\theta_{23})$. This is not subject to the same degeneracy as the $\nu_\mu \rightarrow \nu_\mu$, however it is dependant on a precise measurement of θ_{13} .

Chapter 3

Oscillation Experiments

Neutrino oscillation experiments are one of the most effective ways in which to study the neutrino and can serve as testing grounds to probe BSM physics. The early experiments — Homestake, Kamiokande, SAGE, GALLEX, etc. — set bounds on many of the oscillation parameters, however there is still much to be learned from the current and next generation of oscillation of experiments. The current best fit values for the oscillation parameters, located in section 3.2, indicate that there is still some headway to be made, particularly with respect to the CP violating phase. This dissertation will focus on long-baseline (LBL) experiments (and in particular, the Long Baseline Neutrino Experiment, or *LBNE*), that is to say experiments in which the baseline $L > \mathcal{O}(1 \text{ km})$, however the importance of other types of experiment should not be overlooked. Having both LBL and a variety of other classes of experiment will deliver some complementarity in their measurements and allow the oscillation parameters to be measured to higher precision.

Interestingly, in addition to expanding the knowledge of neutrino physics, neutrino oscillation experiments serve several other purposes. Outlined as one of the main goals for the proposed LBNE [45] and LAGUNA [46] experiments is the testing of grand unified theories (GUTs). GUTs often exhibit exotic processes such as nucleon decay, and it is thought that the massive, high-resolution detectors will significantly expand the search for these rare processes. Another area of study which oscillation experiments may lend themselves to is the study of supernovae. Detectors are thought to be able to observe the intense neutrino bursts produced at core-collapse of supernovae, providing unprecedented information about the phenomena. The possibility of obtaining these results, along with the SM precision tests available to neutrino oscillation experiments make them one of the most intriguing areas of experimental physics today.

3.1 Experiments

As noted in section 2.2.2, neutrino oscillations can be completely defined by six parameters — the mixing angles, the mass-squared differences, and the CP violating phase — and the measurements of each of these parameters are dominated by different classes of experiment. Recent results presented at the Neutrino 2014 conference have provided more precise measurements of all of the oscillation parameters and the current best fit and 3σ regions are presented in the table in section 3.2.

3.1.1 Solar and Atmospheric Experiments

Super-Kamiokande (SK) and Borexino massively dominate the solar neutrino sector. In order to detect neutrinos, SK contains 50,000 tons of ultra-pure water and $\sim 11,000$ photomultiplier tubes (PMTs) [47]. When the neutrinos interact with electrons or nuclei in the water, a charged particle is produced moving faster than the speed of light in the medium, and this produces a cone of Cherenkov radiation. When a μ particle is produced, it is not susceptible to changes in its momentum due to its large mass, and so produces a well defined Cherenkov cone. Conversely, electrons are susceptible to changes in their momentum, and so a distorted ring of Cherenkov radiation will be observed from the induced electromagnetic showers. This distortion can be thought of as a superposition of a number of Cherenkov cones. This light is then detected by the PMTs, and the shape and distortion of the cone is used to determine which particle caused it and in this manner the flavour of the original neutrino can be deduced. The Borexino detector instead opts for a liquid scintillator detector [48], however the process is almost the same: Cherenkov radiation is produced by particles moving through the scintillator and collected by around 1700 PMTs.

Solar data from experiments like SK and Borexino, as well as reactor data from experiments such as KamLAND, are the main way in which the θ_{12} mixing angle is determined, which is currently set at $\theta_{12} = 33.48^{\circ +0.77}_{-0.74}$ by global fits.

Super-Kamiokande also dominates the measurement of atmospheric neutrinos, which is one of the methods — along with long baseline experiments — that θ_{23} is measured. Atmospheric neutrinos are created when cosmic rays strike nuclei in the upper atmosphere, creating a shower of hadrons which then decay into neutrinos and other products. The current global fit sets $\theta_{23} = 42.2^{\circ +0.1}_{-0.1}$ if it is found to be in the lower octant, and $\theta_{23} = 49.4^{\circ +1.6}_{-2.0}$ if it is found to be in the higher octant.

3.1.2 Short Baseline Experiments

Short baseline experiments (SBLs), defined by a baseline of $\mathcal{O}(1\text{km})$, often use electron anti-neutrinos produced by reactors. Because the baseline is short, the $\bar{\nu}_e$ disappearance due to the solar parameters, θ_{12} and Δm_{21}^2 can be neglected, and the atmospheric parameters, θ_{23} and Δm_{13}^2 , have only a small effect, and so these experiments are best placed to measure the value of θ_{13} . In particular Daya Bay and RENO, dominate the measurement of this mixing angle. Both the Daya Bay and RENO experiments use liquid scintillator detectors, however they use the inverse beta decay process to define a neutrino experiment [49, 50]. The idea is that a distinct flash of radiation can be detected from the electron-positron annihilation process, and the characteristic delay between this and the flash of radiation from the neutron capture defines a neutrino interaction.

The current global fit suggests a value of $\theta_{13} = 8.52^{\circ}_{-0.21}{}^{+0.20}$. As CP violation only becomes prominent at large baselines, SBL experiments are insensitive to δ_{CP} , however the revelation that θ_{13} is relatively large indicates that a larger number of events should be detected, and the dominant term in equation 2.116 can be more easily probed, meaning that there are opportunities to discover the mass hierarchy in this sector.

3.1.3 Long Baseline Experiments

Long baseline experiments (LBLs) are loosely defined as having a baseline longer than their SBL counterparts. Due to the unrigorous nature of their definition the LBLs come in two flavours, reactor experiments and neutrino beam experiments. KamLAND seems to be unique among neutrino oscillation experiments in that it is the only long baseline reactor neutrino experiment. The experiment uses all of Japan's nuclear industry as one source of electron anti-neutrinos. KamLAND uses the same detection process as the previously mentioned SBL experiments: Inverse beta decay in liquid scintillators [51]. The spread of the majority of the baselines of 140 km - 210 km means that the detector is particularly sensitive to the solar parameters. As already stated, the solar mixing angle is mostly determined by SK, however KamLAND dominates the determination of the solar mass-squared difference, Δm_{21}^2 . The current best fit value for this is $\Delta m_{21}^2 = 7.5^{\pm 0.19}_{-0.17} \times 10^{-5}$.

The more conventional form of LBL experiment is the neutrino beam. The general set up for these experiments is to have a storage of protons, which can be extracted and directed towards a carbon target. Interactions on the target produce a shower of mesons (kaons and pions), and these are then focussed down a decay tunnel, where

the mesons decay into secondary products including neutrinos. LBL experiments act to constrain the θ_{13} , θ_{23} and Δm_{13}^2 parameters whilst also giving indication on the octant of θ_{23} and the value of the CP violating phase. LBL data previously relied heavily on the MINOS experiment, however recently this has been superseded by T2K and will be further replaced by NO ν A. MINOS and NO ν A will share a beam source — the NuMI neutrino beam — and they have both been designed to use liquid scintillator detectors, however it is claimed that the NO ν A scintillators will be of higher quality and lower cost than their MINOS counterparts. Another difference is that unlike the MINOS detector, the NO ν A detector will sit off-axis of the neutrino beam which has the benefit of more oscillation-energy neutrinos and fewer background events. T2K uses a similar beamline and processes, again using scintillation processes to detect the neutrinos in the near detector, and uses SK as its far detector. The current best fit values for the large mass-squared splitting is $\Delta m_{31}^2 = 2.458^{+0.002}_{-0.002} \times 10^{-3}$ if it is found to be in the normal hierarchy and $\Delta m_{31}^2 = -2.448^{+0.047}_{-0.047} \times 10^{-3}$ in the inverted hierarchy.

3.1.4 Neutrino Factories

Over the last decade or so, the idea of a dedicated source of neutrinos has gained traction in the form of a Neutrino Factory. In 2011, the Interim Design Report by the International Scoping Study for the Neutrino Factory Collaboration [52] focused on a set up in which protons collide with a target, creating pions and secondary muons. These muons are then captured and stored in storage rings, where they can be focussed into a beam and decay into an intense source of muon and electron neutrinos and anti-neutrinos. By measuring the charge, polarization and momentum of the muons, the composition of the neutrino beam is expected to be accurately known. The uncertainties on the beam composition and the flux of the neutrino beam are expected to be much lower than typical neutrino beams. By having two muon storage rings, two beams can be produced and sent to different detectors: one to a detector at a long-baseline and one to a detector at an intermediate-baseline.

As with the other proposed future neutrino experiments, superbeams and beta-beams, the primary goal of the Neutrino factory is to constrain the oscillation parameters and resolve the eight-fold degeneracy. However, with the next generation experiments there are exciting opportunities to probe several other areas. The unitarity of the mixing matrix needs to be tested, and the possibility of a fourth generation of leptons could be explored. Further to this it may be possible to detect sterile neutrinos via searching for new oscillation frequencies and mixing angles.

3.1.5 SuperBeams

Superbeams use the same general setup as typical neutrino beam experiments, however the proton beam intensity is much higher, meaning that the neutrino luminosity is also much higher. This is what allows detectors such as NO ν A to be placed off axis. The problem with these beams is that there is expected to be contamination of the beam by approximately 0.5% electron neutrinos [53].

Although experiments such as SPL and LBNE are expected to increase the sensitivity to the relevant oscillation parameters (θ_{23} , θ_{13} , Δm^2_{31}), and provide some guidance on the unknown oscillation parameters, these experiments are not expected to be as sensitive to the remaining unknown parameters as the Neutrino Factory. However, the possibility of constructing a superbeam as part of a staged construction of a Neutrino Factory may be a logical step as much of the technology needed for Superbeams must also be developed for Neutrino Factories. A more in-depth discussion of the LBNE setup and physics reach is given in chapter 5.

3.1.6 Beta-Beams

Beta-beams intend to make use of beta decay in various species of ions. By this method a beam of purely electron neutrinos or anti-neutrinos is provided. As the kinematics of β decay is well known, the flux of the produced neutrinos can be precisely determined by knowing three parameters: The type of ion (and the end-point kinetic energy of the emitted electron), the relativistic E/m of the ion, and the baseline. The choice of isotopes should be made by compromise between ensuring that the half-life is not so short that it causes strong losses in the acceleration phase, but short enough that a neutrino beam of sufficient flux is produced [52].

As beta-beams are typically of lower energy than superbeams, it has been suggested that detectors be placed near the first oscillation maximum in the L/E plane. This suggests that beta-beams will be less sensitive to CP violation as higher order maxima, which Superbeams have access to, exhibit greater CP violating effects. It has been suggested that a beta-beam/superbeam combination may provide similar sensitivity to the Neutrino Factory, however in general it is expected that a neutrino factory would dominate sensitivities over all of the parameter space.

3.2 Current Oscillation Parameters

Table 3.1 shows the current best fit values to the oscillation parameters after the Neutrino 2014 conference [14], along with what type of experiment dominates the measurement. It is of interest that the CP violating phase remains completely unconstrained at 3σ , with the possibility of CP being conserved ($\delta_{CP} = 0, \pi$) even within the 1σ range. Unless stated otherwise, these are the values which have been used throughout this work when producing plots both analytically and numerically.

Parameter	Best Fit Value $\pm 1\sigma$	3σ	Determined By
$\theta_{12}/^\circ$	$33.48^{+0.77}_{-0.74}$	$31.30 \rightarrow 35.90$	Solar & KamLAND
$\theta_{13}/^\circ$	$8.52^{+0.20}_{-0.21}$	$7.87 \rightarrow 9.11$	Atmospheric & LBL
$\theta_{23}^{LO}/^\circ$	$42.2^{+0.1}_{-0.1}$	$38.4 \rightarrow 53.3$	SBL & LBL
$\theta_{23}^{HO}/^\circ$	$49.4^{+1.6}_{-2.0}$		
$\Delta m_{21}^2/10^{-5}\text{eV}^2$	$7.5^{+0.19}_{-0.17}$	$7.03 \rightarrow 8.09$	KamLAND
$\Delta m_{31}^{2,NH}/10^{-3}\text{eV}^2$	$2.458^{+0.002}_{-0.002}$	$2.325 \rightarrow 2.599$	LBL
$\Delta m_{31}^{2,IH}/10^{-3}\text{eV}^2$	$-2.448^{+0.047}_{-0.049}$	$-2.590 \rightarrow -2.307$	
$\delta_{CP}/^\circ$	251^{+67}_{-59}	$0 \rightarrow 360$	Undetermined

Table 3.1: Table showing the best fit values, 1σ and 3σ ranges for the oscillation parameters. Here, LO and HO refer to the lower and higher octants respectively, and NH and IH refer to the normal and inverted hierarchies.

Chapter 4

Statistical Overview

Within the field of neutrino physics, there has been much debate upon the statistical methods used in experimental analysis in recent years. In particular, the study of the mass hierarchy which has two discreet values (normal/inverted ordering) has come under scrutiny as it has previously been unclear whether it can be approached from the usual frequentist approach widely implemented in the literature. This section will give a brief overview of the statistics of neutrino oscillations before moving on to a treatment of these “discreet frequentist probabilities”. Note that more information on how GLoBES actually goes about creating the chi squared statistic can be found in appendix C.

4.1 Likelihoods, Bins and Priors

The objective of any statistical test is to gain information on how a theoretical hypothesis matches up to experimental data. In the case of neutrino oscillation physics this boils down to: “how well can we theoretically predict event numbers (or probabilities) for specific channels ($\nu_\mu \rightarrow \nu_e$ and $\nu_\mu \rightarrow \nu_\mu$ being dominant for accelerator neutrinos) in physical experiments by varying the values of the six parameters which these values depend upon?”. This introduces a six dimensional parameter space, and constraining this is no easy feat. Discussion on some of the degeneracies which currently plague the field have been discussed in section 2.4.

To begin, it is worth defining the *likelihood function* of a system,

$$\mathcal{L}(n|y) = P(y|n). \quad (4.1)$$

The likelihood can essentially be thought of as an “inverse” probability, in that the the

probability discusses how likely the data, y , is when given a predicted data, n , whereas the likelihood asks what the chances are of the expected data being true given a set of data. It should be stated that likelihood has no physical meaning and its use lies in comparison of likelihoods. In general, log-likelihood ratios are considered [54],

$$\lambda = \frac{\mathcal{L}(n|y)}{\mathcal{L}(y_{true}|y)}. \quad (4.2)$$

y_{true} is assumed to be the "true" data, which could be observed with no errors. Wilks' theorem then states that defining a test statistic as

$$\Delta\chi^2 = -2 \ln(\lambda) = -2 \ln(\mathcal{L}(n|y)) + 2 \ln(\mathcal{L}(y_{true}|y)) \quad (4.3)$$

ensures that it approaches a χ^2 distribution asymptotically, hence the label $\Delta\chi^2$. The objective is then to minimise the $\Delta\chi^2$, which can be done by varying free parameters in the theory. $\Delta\chi^2 = 0$ will occur when the test parameters exactly match the true parameters (in the absence of statistical fluctuations). As data produced by GLoBES is binned (see appendix C) and drawn from a Poisson distribution, this can be further simplified, and the substitution $y_{true} = y$ can be made, as the "true" data can be replaced with the bin-by-bin maximum likelihood estimation which is equal to y . This gives rise to the Poisson likelihood χ^2 ,

$$\Delta\chi^2 = 2 \sum_i^{bins} y_i - n_i + n_i \ln \left(\frac{n_i}{y_i} \right). \quad (4.4)$$

here, the sum is over the number of bins of data.

In general, past experiments have determined oscillation parameters to some confidence, and using these past measurements as guidance can improve sensitivity to other parameters and help to constrain the parameter space. Values of the oscillation parameters can be included as priors, which give each parameter a Gaussian distribution around its best fit value with a width corresponding to how precise past measurements of the parameter have been. These Gaussian fits act to penalise values far from the best fit value, and by minimising over the parameter space, less idealistic χ^2 values can be estimated. They are included by adding extra terms for each prior,

$$\Delta\chi^2_{+prior} = \min_{\theta} \left(\Delta\chi^2(\theta) + \frac{(\theta_i - \theta_i^0)^2}{\sigma_{\theta_i}^2} \right), \quad (4.5)$$

where θ is the vector of oscillation parameters (plus the matter density, which is con-

sidered as such for these purposes), and θ^0 is the best fit value. σ_{θ_i} is the error on the measurement. More information on how GLoBES actually calculates χ^2 values can be found in appendix C.

4.2 Mass Hierarchy Statistics

As the Mass hierarchy is essentially a “yes or no” type question with two hypotheses, the usual methods as described above cannot be used. Instead, frequentist hypothesis testing is used for these analyses. Frequentist hypothesis testing essentially assumes the existence of two hypotheses, the hypothesis which is being tested (also called the null hypothesis), H , and the alternative hypothesis H' . Initially, this will be introduced for simple hypotheses — those which do not depend on any free parameters — and then this will be generalised to composite hypothesis testing and applied to the mass hierarchy.

4.2.1 Simple Frequentist Hypothesis Testing

Frequentist hypothesis testing essentially boils down to determining whether a given null hypothesis can be excluded at a given confidence level, and with this aim a test statistic T must be defined. There is a lot of freedom in choosing a test statistic: so long as the statistic reduces the data to single stochastic variable which can be used in hypothesis testing, it can be chosen to be anything. When the T distribution is known under the null hypothesis being true, it is decided that H is rejected at confidence level $(1 - \alpha)$ if the observation is within the α most extreme results, i.e. if $T > T_c^\alpha$ where T_c^α is the critical test statistic which is determined at the point of rejection α . For instance, if the probability distribution function for T is Gaussian then a plot can be produced such as in figure 4.1, where the shaded regions are bounded by the test statistic evaluated at the critical points.

The definition of T_c^α is given by

$$\alpha = \int_{T_c^\alpha}^{\infty} p(T|H) dT, \quad (4.6)$$

where $p(T|H)$ is read as being the value of the test statistic given that the null hypothesis is true. The probability α is a measure of the probability of rejecting the null hypothesis although it is true, and is known as a type-I error. By methods discussed in reference [55], this can be converted to a Gaussian number of standard deviations away from the mean, giving a higher CL with increased distance from the mean.

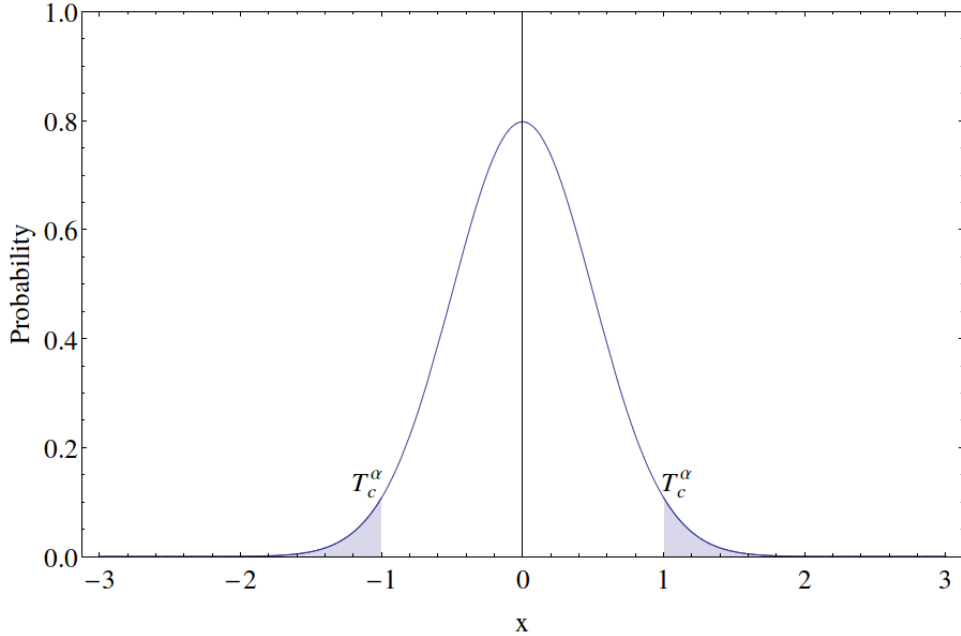


Figure 4.1: Gaussian probability distribution function for the test statistic T with mean $\mu = 0$ and standard deviation $\sigma = 0.5$, assuming that the null hypothesis is true. The shaded areas are bounded at the critical points.

With the aim of quantifying how powerful any test statistic is, the probability of accepting the null hypothesis although it is false, β , must be calculated. This is known as a type-II error.

$$\beta = \int_{-\infty}^{T_c^\alpha} p(T|H')dT, \quad (4.7)$$

where $p(T|H')$ is now read as being the probability distribution of T given that the alternative hypothesis, H' is true. If the value of β is small then the probability of making a type-II error is small, and so the “power” of the test statistic, $(1 - \beta)$ is large. By this metric, a test statistic with a high power is better than a test statistic with a low power.

4.2.2 Application to the Neutrino Mass Hierarchy

In the case of the neutrino mass hierarchy, the simple frequentist hypothesis testing cannot be used because the hierarchy depends on all of the oscillation parameters, and in particular δ_{CP} . This means that composite hypothesis testing must be invoked. The approach is essentially the same, however several conditions must be met.

The main difference is that the null hypothesis H can only be rejected if all of the

oscillation parameters can be rejected, and to this end, the test statistic must be maximised over the parameters, $\max_{\theta \in H} T_c^\alpha(\theta)$. The second difference is that the power of the test statistic now depends on the true parameters in the alternative hypothesis,

$$\beta(\theta) = \int_{-\infty}^{T_c^\alpha} p(T|\theta \in H') dT, \quad (4.8)$$

where T_c^α is maximised as above.

Within the literature, the χ^2 statistic is most widely used, and so this will be adopted here. As discussed in appendix C, if the mean value, μ_i for the i^{th} degree of freedom in the χ^2 distribution,

$$\chi^2 = \sum_{i=1}^n \frac{(x_i - \mu_i)^2}{\sigma_i^2}, \quad (4.9)$$

is dependant upon a set of P parameters, then the minimum of the distribution is usually considered,

$$\chi_{\min}^2 = \min_{\theta} \chi^2(\theta). \quad (4.10)$$

By Wilks theorem, this follows a χ^2 distribution with $n - P$ degrees of freedom, although in general this isn't guaranteed, and must be confirmed by Monte-Carlo simulation.

To choose a test statistic to analyse these discrete choices of variable, the literature can provide guidance. Reference [45], amongst other have chosen to define their test statistic as

$$T_{MH} = |\min_{\theta \in IH} \chi^2(\theta) - \min_{\theta \in NH} \chi^2(\theta)| = |\chi_{IH}^2 - \chi_{NH}^2|, \quad (4.11)$$

and so this is what has been used throughout this dissertation for studies of the mass hierarchy unless stated otherwise.

4.3 CP Violation Statistics

Statistics related to CP violation and the octant of θ_{23} are not as complicated as those for the mass hierarchy, as neither is a “yes or no” type question and so there is no need for composite hypothesis testing.

Although constraining the value of the CP violating phase is important, actually determining whether CPV is manifest in nature is far more important than finding the exact value. To this end it is necessary to define a test statistic which can quantify the

ability of LBNE to discover whether CP is violated. The test statistic must be zero at $\delta_{CP} = 0, \pi$, as if CP is not violated, then there's obviously no way for LBNE to discover it. The test statistic adopted in this dissertation is the one which has widespread usage in the literature,

$$\Delta\chi^2_{CPV} = \min(\Delta\chi^2_{CP}(\delta_{CP}^{test} = 0), \Delta\chi^2_{CP}(\delta_{CP}^{test} = \pi)), \quad (4.12)$$

where

$$\Delta\chi^2_{CP} = \chi^2_{\delta_{CP}^{test}} - \chi^2_{\delta_{CP}^{true}}. \quad (4.13)$$

and the “true” value of delta is run over from 0 to 2π . Taking the minimum guarantees that the test statistic goes to zero to both $\delta_{CP} = 0$ and $\delta_{CP} = \pi$, and accounts for the fact that the larger CP violation is, the more easily it should be detected.

4.4 θ_{23} Octant Statistics

When dealing with the octant of θ_{23} , the main interest is how well all of the values in the wrong octant can be disregarded for any true value of θ_{23} . For this reason, the test statistic,

$$\Delta\chi^2_{octant} = |\chi^2_{\theta_{23}^{test}>45^\circ} - \chi^2_{\theta_{23}<45^\circ}|. \quad (4.14)$$

is used, where each χ^2 is minimised over: for each of the test octants, the value of θ_{23}^{test} in that octant is taken to be the one which gives the minimum χ^2 values. In the absence of statistical fluctuations, as has been assumed in this work, the χ^2 in the true octant is identically zero.

$$\Delta\chi^2_{octant} = \min(\Delta\chi^2_{test}) \quad (4.15)$$

where the test octant is always defined to be in the higher (lower) octant if the true octant is the lower (higher) octant.

Chapter 5

Precision study of LBNE

The Long Baseline Neutrino Experiment (LBNE) is a proposed superbeam experiment which will produce neutrinos at Fermilab in Batavia, Illinois and send them 1300km to the Sanford Underground Research Laboratory in Lead, South Dakota. Now a priority by Fermilab, and having already succeeded in securing financing for a reduced initial phase, LBNE is obviously hugely important for the imminent future of neutrino oscillation physics. The combination of this baseline and the provision of neutrinos and anti-neutrinos of energy $0.5 - 5$ GeV means that this experiment will cover the first and second oscillation maxima, and so will be somewhat sensitive to δ_{CP} , although confirmation of CP violation at 5σ will only occur for the later setups (with improvements to the beamline and detector), and only for some values of δ_{CP} . The experiment is expected to further constrain the values of the oscillation parameters, and is expected to determine the mass hierarchy to a high precision. A full capacity LBNE is also expected to be able to measure the value of θ_{23} to within a few degrees, and will determine its octant provided that the true value is not too close to maximal.

5.1 LBNE Experimental Setup

LBNE will use the pre-existing NuMI beamline to create an intense beam of μ neutrinos (or anti-neutrinos) with a peak flux of 2.5 GeV which will then be aimed towards a near detector 500 m downstream of the proton target and a far detector, located 1300 km away in South Dakota [45]. The main intentions of the experiment can be summarised as follows:

- i LBNE expects to characterise the known oscillation parameters, in particular providing measurements of θ_{13} and θ_{23} , including it's octant. It is also expected to determine the mass hierarchy with high precision and to constrain the value of the CP violating

phase. If CPV is close to maximally violated (i.e. $\delta_{CP} \sim \pi/2, 3\pi/2$), then LBNE is expected to provide confirmation of CPV in the leptonic sector.

- ii Many GUTs are expected to exhibit processes such as nucleon decay, and the huge size of neutrino detectors provide the perfect testing ground of these theories. Several GUTs have already been ruled out by previous neutrino experiments, and LBNE is expected to constrain the allowed parameters in the remaining theories.
- iii It is also expected that neutrino flux from supernovae core collapse could yield information about the processes that drive such phenomena, should any supernovae occur during the lifetime of LBNE. In a 20 year run, it is expected that there is around a 40% chance of LBNE observing supernova neutrinos.

LBNE intends to undergo a staged construction process, having already secured funding for a reduced initial phase [56]. LBNE is expected to have a near detector, however funding for this has not been secured, and this has not been considered in these simulations.

5.1.1 Initial Setup

The initial setup of the LBNE beamline will use the NuMI beamline with the additional NO ν A and Proton Improvement Plan (PIP) upgrades (700 kw at 120 GeV) with additional PIP II upgrades. This means that at initial setup, LBNE will use a beam power of 1.2 MW with a proton energy which is tunable between 60 – 120 GeV.

LBNE is intended to have both a near and far detector, where the near detector may be built as a separate experiment at the same time as the far detector, or later. The near detector is expected to house argon targets similar to those located in the far detector, allowing measurements of the absolute neutrino flux and energy shape of the four neutrino flavours (ν_e , ν_μ , $\bar{\nu}_e$, $\bar{\nu}_\mu$), along with the cancellation of systematic errors. As the near detector is privy to around 10^7 interactions per year, it is expected to measure neutrino fluxes, cross sections, and particle production, and so will be an experiment in its own right. The far detector will initially have a Liquid Argon Time Projection Chamber (LArTPC) with a fiducial mass of 10 kt. When charged particles pass through the liquid argon, they leave a path of ionisation electrons. By drifting these paths over to wire planes, the magnitude, position, and time can be reconstructed [57]. The LArTPC has been chosen as it has unmatched position and energy resolution while being scalable, which allows the staged approach to be taken. It is also expected to be sensitive to proton

decay modes.

In 2012, the money was granted for a reduced “CDR” design, without the near detector, and not located underground. It is still hoped that money can be found for the full initial setup. The reference values which will be used in simulations are found in table 5.1.

CDR	Range	Reference Value
Proton Energy	60-120 GeV	120 GeV
Beam Power	1.2 MW	1.2 MW
Fiducial Mass	10 kt	10 kt

Table 5.1: Experimental ranges and reference values for GLoBES simulations for the initial setup.

5.1.2 Final Setup

The staged improvement of LBNE allows for several improvements to be made over the initial experiment. Upgrades further to the PIP II improvements intend to upgrade the beamline to produce a beam of 2.3 MW power for 80 GeV protons. The fiducial mass in the far detector is expected to be upgraded to 35 kt. These improvements are expected to yield 5σ confirmation of CP violation for values of δ_{CP} which are far away from their CP conserving values $(0, \pi)$. There is no particular order in which the improvements must be made, and so there is some freedom in that respect.

LBNE Full	Range	Reference Value
Proton Energy	60-120 GeV	80 GeV
Beam Power	2.3 MW	2.3 MW
Fiducial Mass	35 kt	35 kt

Table 5.2: Experimental ranges and reference values for GLoBES simulations for the final setup.

Throughout the following simulations, “final” setup refers to the reference values in the table 5.2, although in the simulations, beamline and detector improvements are generally considered separately.

5.2 Study of Oscillation Probabilities

As LBNE has its baseline set to 1300km, and its detector is sensitive to neutrinos in the 0.5 – 5 GeV range, a study of the oscillation probabilities for neutrinos and anti-neutrinos will yield information about the possible sensitivity to CP violation amongst other things. Figure 5.1 shows the oscillation probabilities against the neutrino energy for the three transitions ($\nu_\mu \rightarrow \nu_e$, $\nu_\mu \rightarrow \nu_\mu$, $\nu_\mu \rightarrow \nu_\tau$). It is easily seen that the μ neutrinos have a much greater chance of evolving into a τ neutrino for most of the energy spectrum, however at the peak flux (~ 2.5 GeV) the electron appearance channel is more likely for both neutrinos and anti-neutrinos. Currently, no attempts are being made to identify charged current ν_τ interactions due to the challenges in producing and detecting them, although there has been some progress in removing τ decay backgrounds.

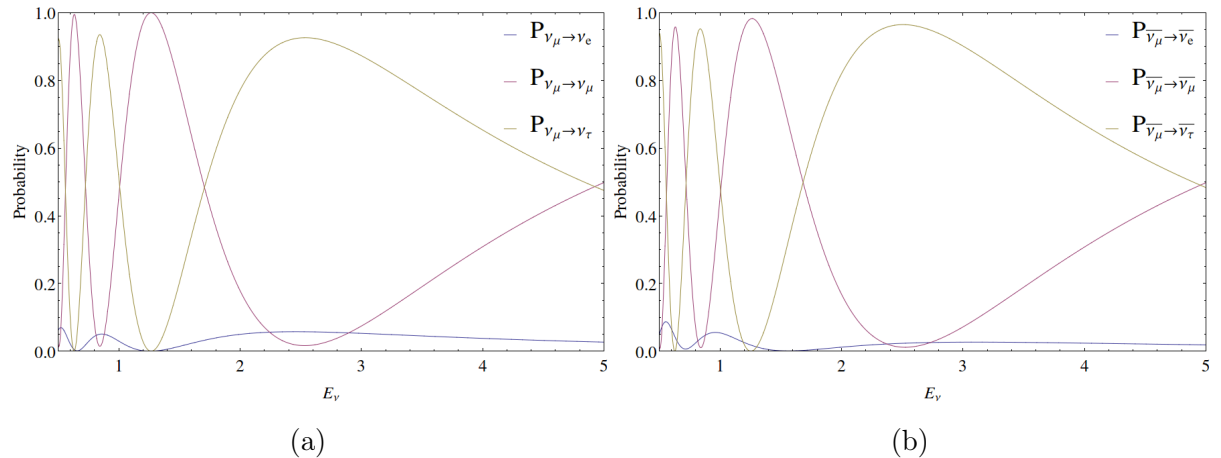


Figure 5.1: Oscillation probability plots for the three channels, for both neutrinos (a) and anti-neutrinos (b). These are produced with the oscillation parameters set to their best fit value defined in table 3.1. The values of the unknown parameters are taken to be in the lower octant, normal hierarchy, and $\delta_{CP} = 0$.

By comparing the plots in figures 5.2 and 5.3 it can be seen that neutrinos have similar oscillation probabilities in the normal hierarchy as anti-neutrinos do in the inverted hierarchy. This is obvious if equation 2.115 is considered: By switching the hierarchy, sending $\delta_{CP} \rightarrow -\delta_{CP}$ and $V_{cc} \rightarrow -V_{cc}$, and pulling out the minus signs, it can be seen that the oscillation probabilities are almost the same up to some re-phasing of δ_{CP} . The differing oscillation probabilities for different values of δ_{CP} suggests that the value of the CP violating phase could be experimentally determined by comparing the shape of the electron appearance channel signal over a range of energies.

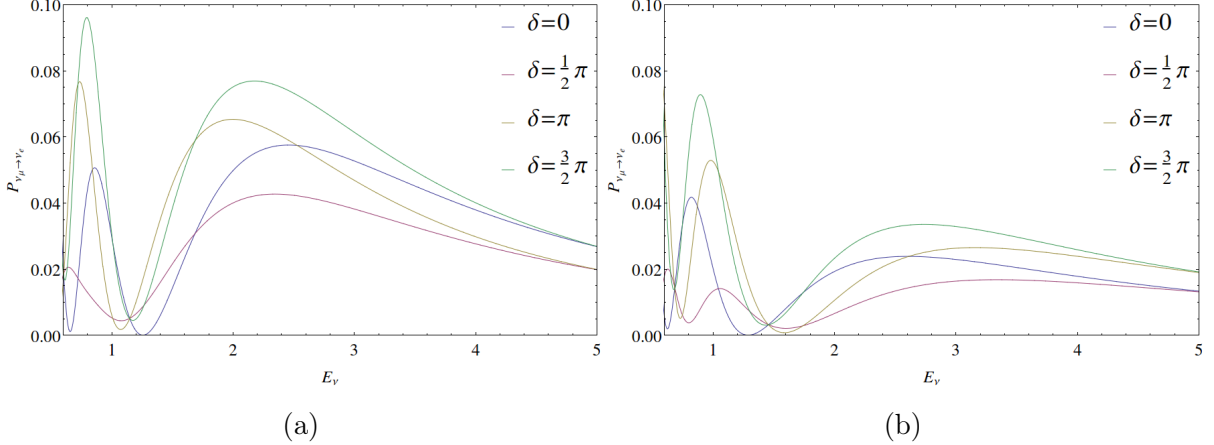


Figure 5.2: Oscillation probability plots for neutrinos in the normal hierarchy (a) and the inverted hierarchy (b). Values are again set to the best fit values in the lower octant.

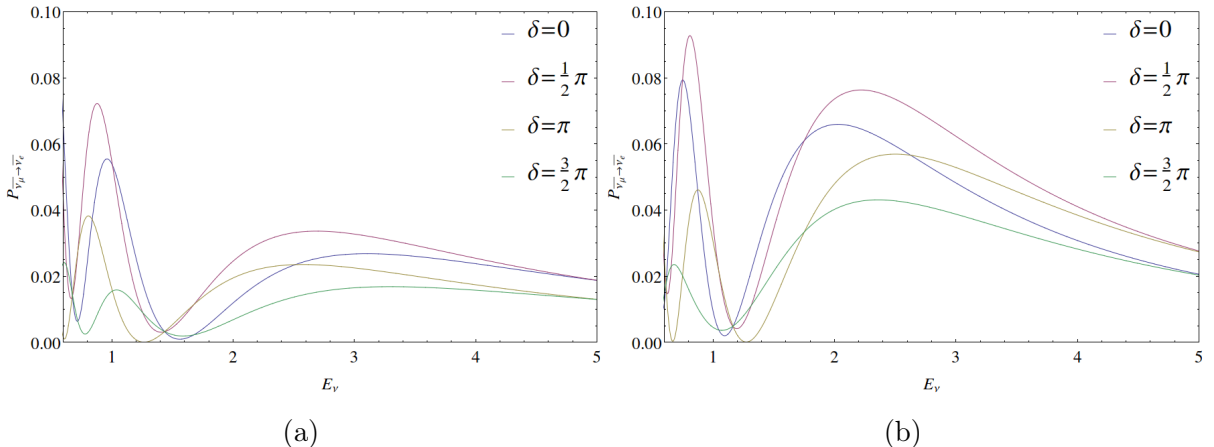


Figure 5.3: Oscillation probability plots for anti-neutrinos in the normal hierarchy (a) and the inverted hierarchy (b). Values set to the best fit values in the lower octant.

Figure 5.4a shows that at 1300km, LBNE has access to the second oscillation maxima, meaning that CP violation sensitivity is greatly increased when compared to an experiment which can only observe the first oscillation maximum. Figure 5.4b exemplifies this, showing the peak CP asymmetry for LBNE. This placement is clearly well chosen as the oscillation maxima is around 2.5 GeV where the peak neutrino flux of the beamline is located. This will maximise the number of transition events which will be detected.

5.3 LBNE Simulation Event Numbers

When simulating LBNE with GLoBES, the event rates are normalised to those in reference [45]. In particular, event rates for the electron appearance channel, $\nu_\mu \rightarrow \nu_e$, have

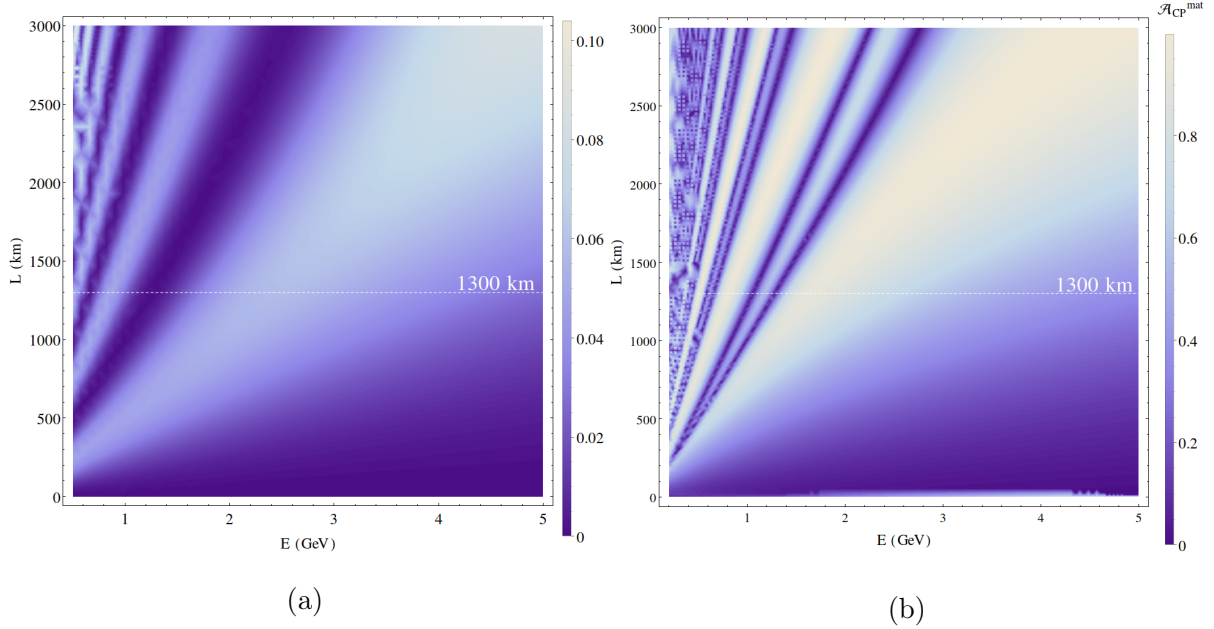


Figure 5.4: (a) shows an oscillation plot in the E - L plane for the electron appearance channel. In figure (b) the CP asymmetry in matter (as defined in equation 2.119) is shown. The dashed white line denotes the baseline of LBNE at 1300km. Here, normal ordering and the lower octant are assumed.

been calculated using values of the oscillation parameters defined in reference [45]. In particular, it is important to notice that the analysis presented in the paper only take events up to 10 GeV in to account, and this comparison takes that in to account. A comparison of the values present in the paper and those calculated by GLoBES simulation are presented below.

ν	δ	LBNE event number	Calculated event number
$\nu_\mu \rightarrow \nu_e$	$-\pi/2$	605	586.353
	0	480	480.501
	$\pi/2$	350	349.566

Table 5.3: Number of events for the $\nu_\mu \rightarrow \nu_e$ transition.

The discrepancy of the event numbers produced by GLoBES and those given in reference [45] are insignificant, and make very little difference to the calculated chi-squared values.

$\bar{\nu}$	δ	LBNE event number	Calculated event number
$\bar{\nu}_\mu$	$-\pi/2$	51	51.68
	0	86	86.18
	$\pi/2$	106	104.34

Table 5.4: Number of events for the $\bar{\nu}_\mu \rightarrow \bar{\nu}_e$ transition.

5.4 Study of LBNE

There is a lot of subtlety in the calculation of χ^2 values, and this is especially true of LBNE and other such large experiments where there are a lot of sources of uncertainty and error. For this reason, plots produced in this section, whilst useful, should not be taken as entirely precise. In particular, the values of error have been naively thrown together in to two sources: background error and signal error. This is completely unrealistic as there are a huge number of sources of error. These are listed in reference [45] to be: beam flux uncertainties, ν_μ energy scale uncertainties, absolute ν_e energy scale uncertainties, simulation uncertainties, fiducial mass uncertainties, and ν_e appearance background systematics uncertainties. As is to be expected, reducing these down to two sources of error is extremely naive. As the LBNE collaboration opted to use the simple χ^2 provided with the GLoBES software, differences between the simulations performed here and those in reference [45] are expected to arise due to differences in the AEDL, smear, flux, and cross section files. Despite this, effort has been taken to try and use the same values as reference [45] where possible.

This section will initially look at simple χ^2 tests for the mixing angles (excluding θ_{12}) and Δm_{31}^2 mass-squared difference, indicating to what precision LBNE should be able to measure each of them, and providing allowed ranges in the $\sin^2(\theta_{13}) - \delta_{CP}$ and $\sin^2(\theta_{23}) - \delta_{CP}$ planes in particular. The sensitivity of LBNE to the CP violating phase, the mass hierarchy and the octant of θ_{23} will then be discussed. The solar parameters are not discussed here as LBNE is not expected to measure them more precisely than SK or KamLAND.

GLoBES can produce χ^2 plots centred around the current best fit values for each of the parameters, and these are shown in figure 5.5. These plots are completely idealistic as they rely on a complete knowledge of the oscillation parameters, i.e. these can be seen as the sensitivity of LBNE to a chosen parameter assuming that all of the other

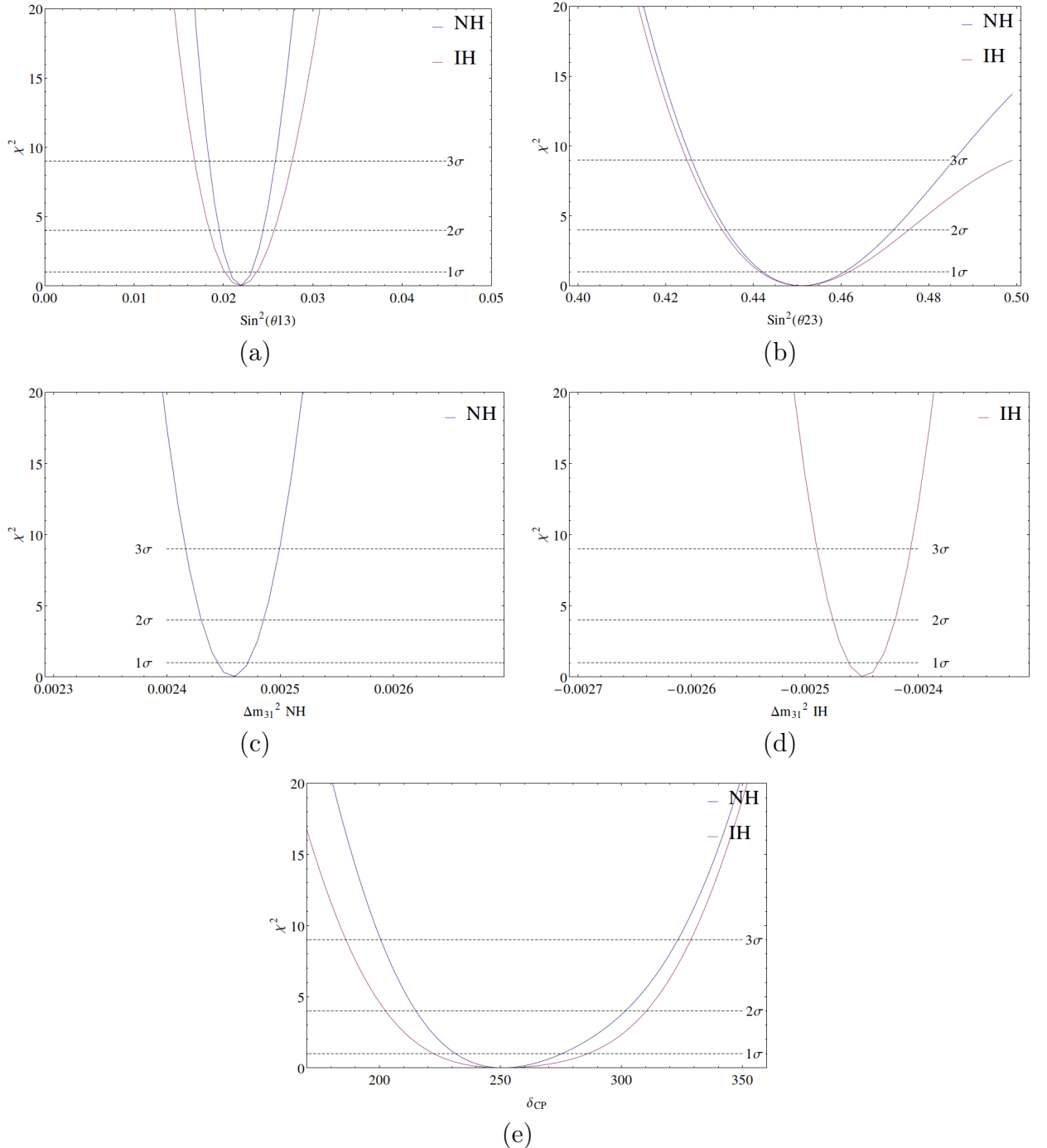


Figure 5.5: χ^2 plots for oscillation parameters in the normal and inverted hierarchies for the initial setup: 1.2MW ν beam power at 120GeV, with a 10 kt detector for 6 years. The hierarchies are presented on different graphs for the atmospheric mass splitting in (c) and (d) so that the curves are more clearly visible. θ_{23} is assumed to be in the lower octant for all plots and the solar parameters have been neglected as LBNE is insensitive to them.

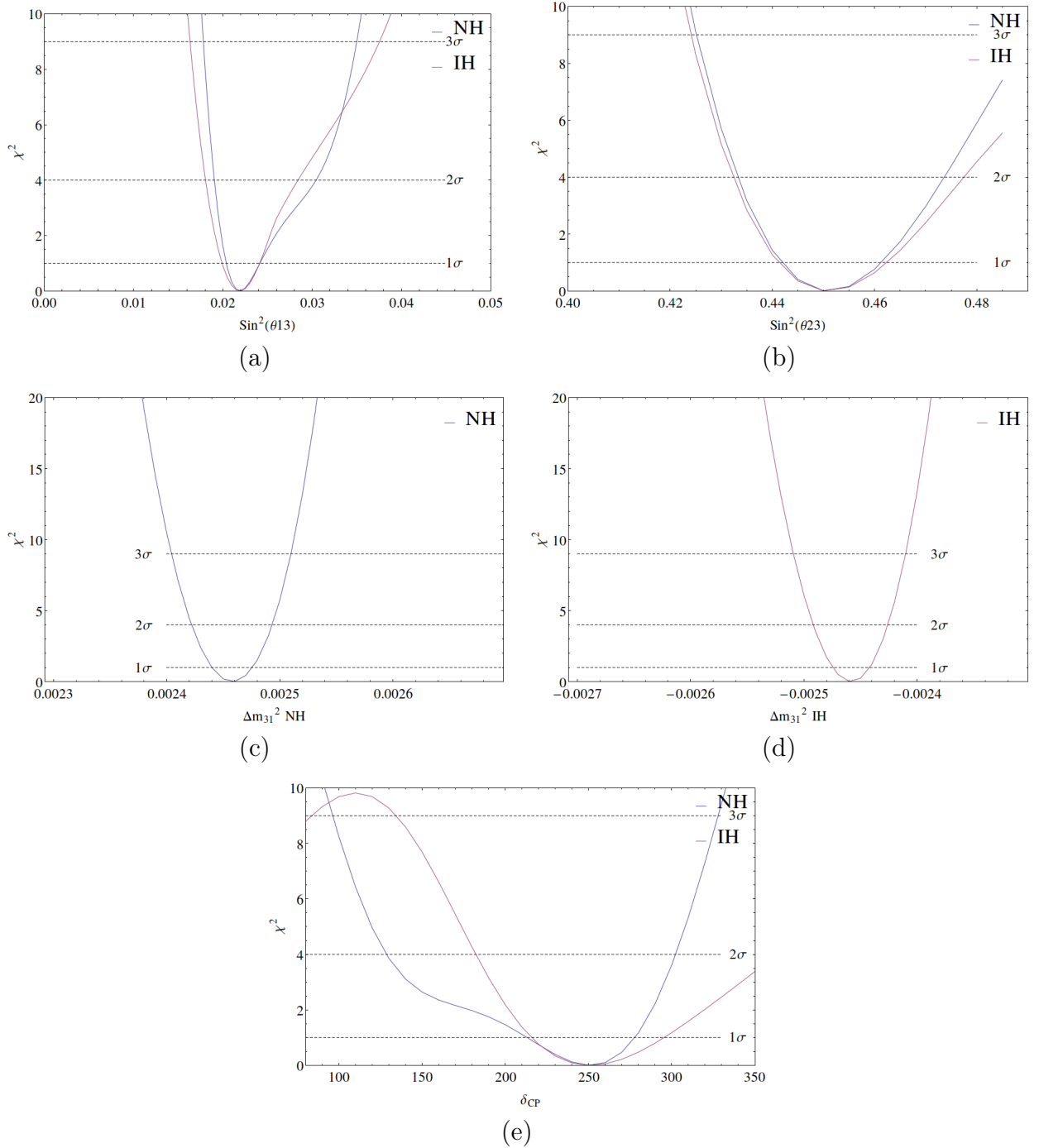


Figure 5.6: These plots have exactly the same setup as those in figure 5.5. They are not idealistic in the sense that they take Gaussian priors in to account, however they can still be seen as such as they assume the true values of the parameters.

parameters are completely determined with infinite precision. These plots also do not take in to account any statistical fluctuations which are expected to be present in any real experiment, however they do take in to account systematics, which are treated by the *pull* method (See appendix C for more details).

To make these plots more realistic, *priors* are used as inputs (see appendix C), which allow the oscillation parameters to vary around their central best fit values. The priors are taken to be Gaussian, with the standard deviation defined to be the 1σ range (as defined in table 3.1), and by minimising the χ^2 over all of the oscillation parameters (including the matter density), a final value can be found and plotted. Plots using this method can be found in figure 5.6. By comparing the two sets of plots (figures 5.5 and 5.6), the over-optimism of the first set can be more easily seen. These plots assume that the 0-point on the χ^2 axis is the “true” value of the relevant parameter, and measures how well LBNE should be able to determine said parameter. As such, these are of limited use, however the realistic plots still give some interesting insight. In particular, LBNE should be able to constrain the value of the CP violating phase at three sigma, and this is especially true for the normal hierarchy (at least for this true value of δ_{CP}). It should be noted that these plots are for the LBNE 10 kt setup without beam upgrades running a ν beam for 6 years. Obviously increasing the beam power, detector mass, and running time will lead to significant increases in the precision which LBNE can measure to, and this will be discussed in detail in the next subsections.

5.4.1 Allowed Regions

Allowed regions can be constructed by simultaneously running over different test values for two of the parameters. Without priors, this is done by setting up a grid, and calculating the χ^2 at each point on the grid. With priors, the current best fit values are set to the true values with priors set to their 1σ uncertainties. The two parameters of interest are kept fixed and the minimiser runs over all of the parameters other than those that are fixed. The minimum over all of the non-fixed parameters is then found and projected on to the plane constructed by the two fixed parameters.

Because δ_{CP} is completely unconstrained at three sigma and is therefore the least well determined oscillation parameter, it is often most interesting to see how differing values of δ_{CP}^{true} vary the allowed regions of different parameters. Here, θ_{13} and θ_{23} have been chosen as they are the least well determined parameters other than δ_{CP} . Both of the simulations here assume the full scope LBNE running with minimum errors for 6 years with equal $\nu/\bar{\nu}$ exposure. The priors on the oscillation parameters are set to their 1σ

values.

Figure 5.7 shows the allowed regions in the $\delta_{CP} - \sin^2(\theta_{13})$ plane for the inverted (coloured lines) and normal (black lines) hierarchies. A comparison of the allowed regions for both the normal hierarchy and the inverted hierarchy indicates that the significance at which the CP violating phase can be determined is not greatly affected by the sign of the mass hierarchy. With the full scope of LBNE it is also expected that the intrinsic degeneracy will be broken, and this is reflected by the lack of an elongated allowed region in the plane. Such an allowed region would indicate multiple solutions indicating the degeneracy had not been broken.

Figure 5.8 shows the allowed regions in the $\delta_{CP} - \sin^2(\theta_{23})$ plane for both the lower and higher octant in the inverse hierarchy. The different colours represent the same as in the previous plot. Should the true octant be found to be greater than 45° , the determination of the CP violating phase will be slightly impaired. This effect can be explained through propagation of errors, as done in section 5.4.3.

5.4.2 Study of the Mass Hierarchy

An in depth analysis of mass hierarchy can be performed, as done for the octant of θ_{23} . It is slightly more subtle, however, in that the same methods cannot be applied due to the choice of mass hierarchy being discreet — it is either the normal hierarchy or the inverted hierarchy. A discussion of the statistics behind these studies are provided in chapter 4, and in particular section 4.2.2. As discussed at the end of this section, the test statistic,

$$T_{MH} = \left| \min_{\theta \in IH} \chi^2(\theta) - \min_{\theta \in NH} \chi^2(\theta) \right| = |\chi^2_{IH} - \chi^2_{NH}|, \quad (5.1)$$

is chosen such that it is in keeping with the literature. In the absence of statistical fluctuations, the χ^2 in the “true” hierarchy (the hierarchy which is being testing) should be identically zero. This test statistic should therefore be read as “the significance at which LBNE can reject the false hypothesis”.

It is important to note that the test statistic in figure 5.9 is no longer labelled as $\Delta\chi^2$, but as simply T . This is because the chosen statistic no longer approaches the χ^2 asymptotically as it does not follow the standard normal distribution, $\mathcal{N}(\pm T_0, \sqrt{T_0})$, but a normal distribution with mean $\pm T_0$ and standard deviation $2\sqrt{T_0}$: $\mathcal{N}(\pm T_0, 2\sqrt{T_0})$. It then follows that one cannot simply square root to find the significance level. This effect is considerably less noticeable at high values of T .

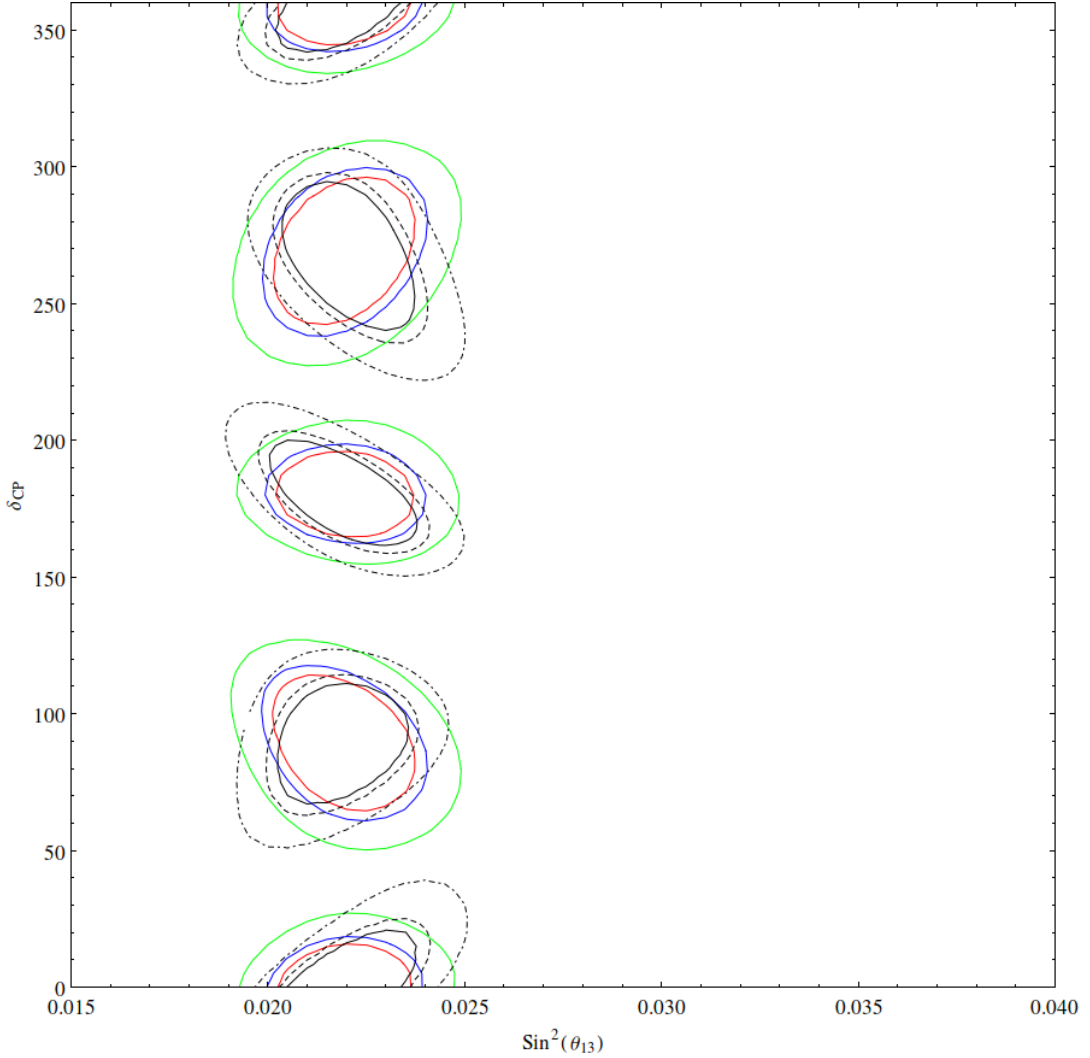


Figure 5.7: Allowed regions in the $\delta_{CP} - \sin^2(\theta_{13})$ plane for $\delta_{CP}^{true} = 0^\circ, 90^\circ, 180^\circ, 270^\circ$. The concentric black lines represent 1σ (solid), 2σ (dashed) and 3σ (dot-dashed) in the normal hierarchy, whilst the coloured lines represent 1σ (red), 2σ (blue), and 3σ (red) in the inverted hierarchy. This simulation has assumed the full scope LBNE for 6 years with equal $\nu/\bar{\nu}$ run time, with minimum errors, and 1σ priors on the oscillation parameters.

The plots in figure 5.9 have been plotted for the Asimov data set - that is that it has been done for the “average” experiment, without statistical fluctuations. These plots show that with improvement in the fiducial mass of the detector, the wrong mass hierarchy can be ruled out at 5σ even without improvements to the beamline. With improvements to the beamline and reduction of uncertainties, this can be increased to over 7σ , and increasing the mass of the detector will increase the sensitivity further. Naturally, extending the run time to $5 + 5$ years for $\nu/\bar{\nu}$ will increase these sensitivities.

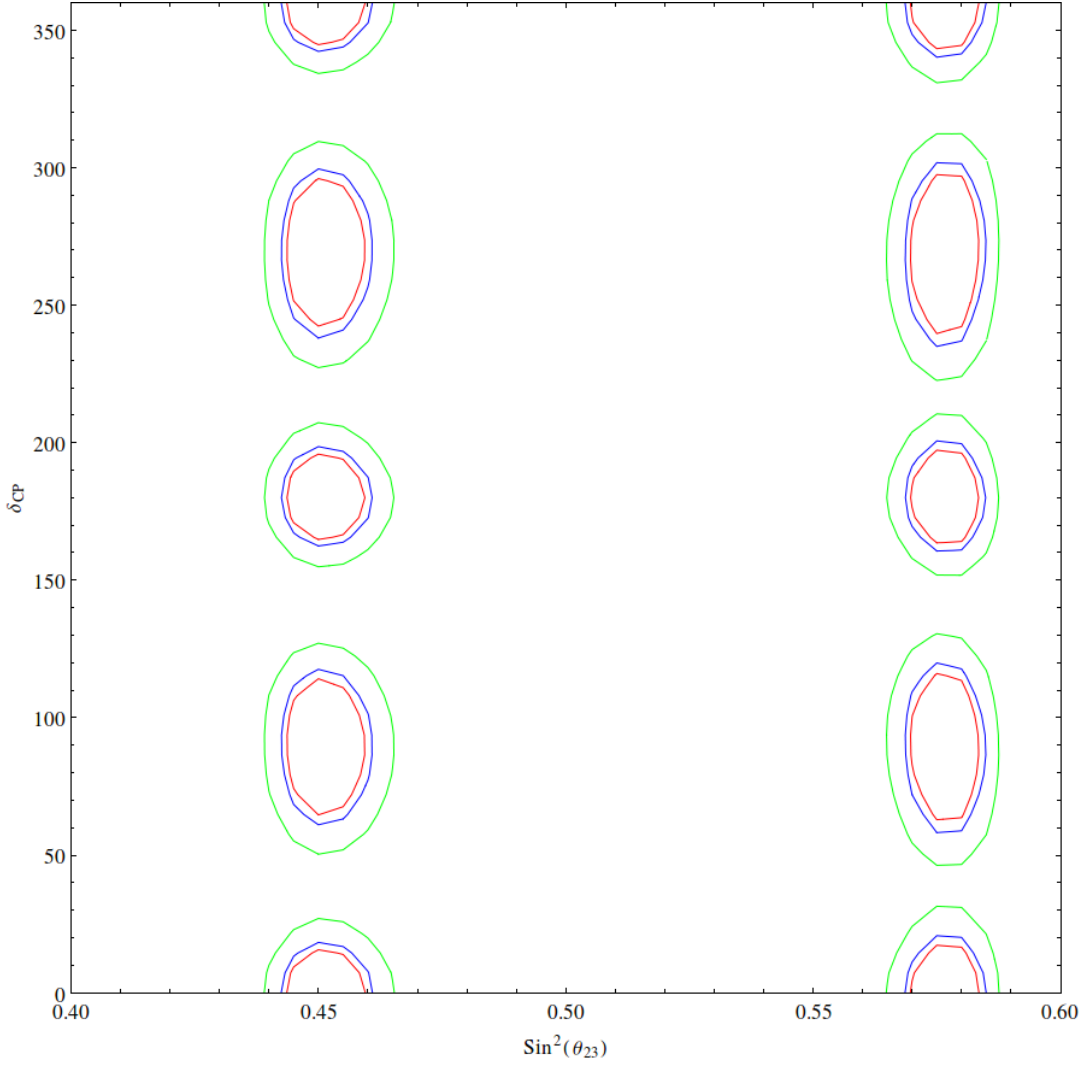


Figure 5.8: Allowed regions in the $\delta_{CP} - \sin^2(\theta_{23})$ plane for $\delta_{CP}^{true} = 0^\circ, 90^\circ, 180^\circ, 270^\circ$, and for both the lower octant and the higher octant. The concentric coloured lines represent the 1σ (red), 2σ (blue) and 3σ (green) allowed regions. The plots on the left assume θ_{23}^{true} is the best fit value in the lower octant, whilst the plots on the right assume θ_{23} is the best fit value in the higher octant. As in the previous simulation, this simulation assumes the full scope LBNE with 3 years ν and 3 years $\bar{\nu}$, minimum errors and 1σ priors on the oscillation parameters.

As is shown in figure 5.10, variation in the value of θ_{23} over both octants allows for some variation in the sensitivity to the mass hierarchy. This is similar to the effect present in figure 5.16, however the effect can be seen as less severe as even with the lowest value of θ_{23} , the mass hierarchy is still expected to be able to rule out the hierarchy with greater than 5σ precision.

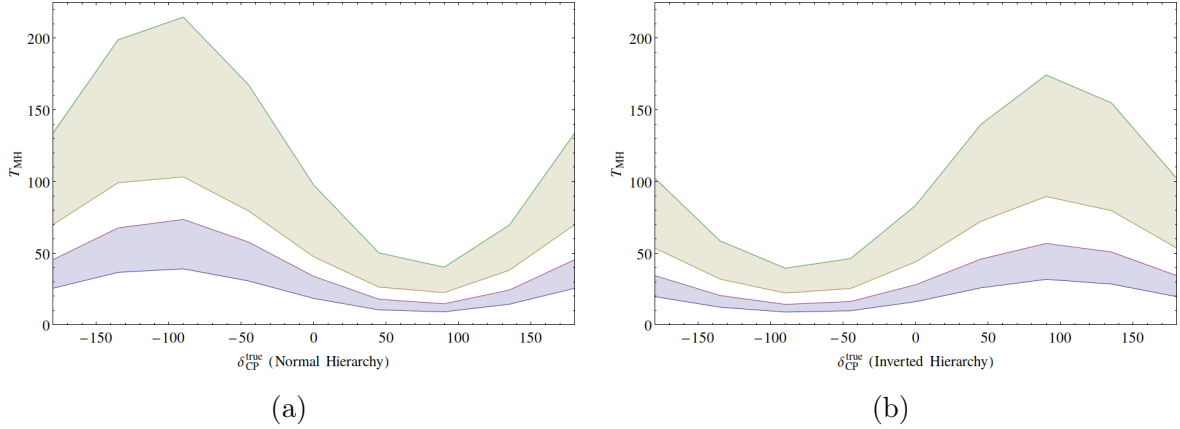


Figure 5.9: Sensitivity to the mass hierarchy in the (a) normal and (b) inverted hierarchies. Here the lower octant of θ_{23} has been assumed. The top band represents sensitivities achieved for the 35 kt setup, whilst the bottom band represents sensitivities for the 10 kt setup. The width of each band represents reduction in error and improvements to the beamline. This simulation assumes 3 + 3 years of running for $\nu/\bar{\nu}$.

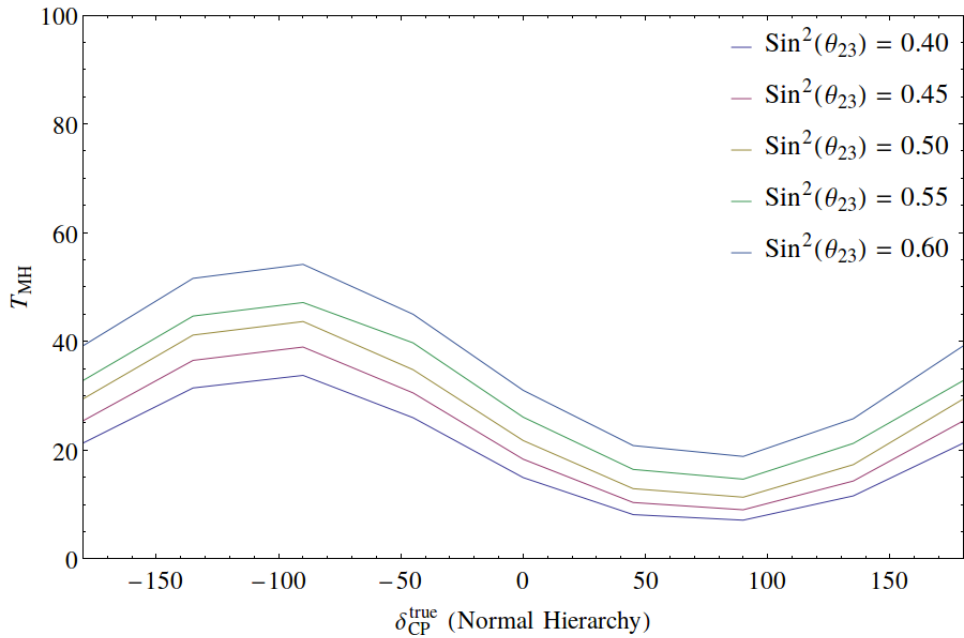


Figure 5.10: MH sensitivity for LBNE initial setup with largest uncertainties, for varying values of θ_{23} .

Similarly to this, and as before, varying the knowledge of θ_{13} in the form of varying the size of the prior on it allows for some insight. Figure 5.11 shows such plots.

Similarly to earlier, the effect of priors is noticeable, although the effect is comparable.

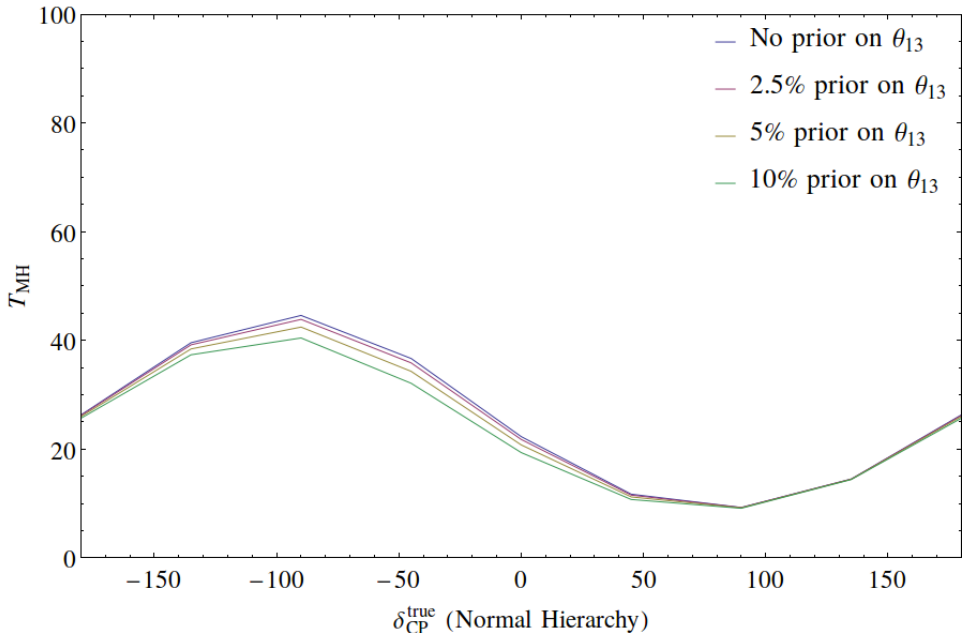


Figure 5.11: MH sensitivity dependence upon knowledge of θ_{13} . All priors are included in this plot.

tively small due to the large significances involved in measurements of the hierarchy.

Figures 5.10 and 5.11 show that even allowing for a (relatively) small value of θ_{23} , and allowing for large errors on θ_{13} , the significance to which LBNE can successfully rule out each of the mass hierarchies remains undiminished.

5.4.3 Study of δ_{CP}

The study of the CP violating phase can be studied in a variety of different ways. It has already been determined that the typical chi-squared test shown in figure 5.6 gives guidance on the sensitivity of LBNE, however cannot be taken to be true on the grounds that these plots *are accurate only if the true value of the parameter is at the point where $\chi = 0$* . In practice, these plots can be constructed for every “true” value in the allowed range, allowing for the fact that the true parameter values are not known, however this would give rise to large numbers of diagrams, only one of which would be realistic. This is, again, of limited use.

CP violation studies have two objectives: to determine whether CP is violated in the leptonic sector (i.e. $\delta_{CP} \neq 0, \pi$), and to constrain the value of the CP violating phase. Although constraining the value of δ_{CP} is important, it is the determination of CP violation in the leptonic sector which has far reaching consequences and is of more

theoretical interest. With this goal in mind a new test statistic can be defined, as in equation 5.2,

$$\Delta\chi_{CPV}^2 = \min (\Delta\chi_{CP}^2(\delta_{CP}^{test} = 0), \Delta\chi_{CP}^2(\delta_{CP}^{test} = \pi)), \quad (5.2)$$

with

$$\Delta\chi_{CP}^2 = \chi_{\delta_{CP}^{test}}^2 - \chi_{\delta_{CP}^{true}}^2. \quad (5.3)$$

Of course, in the absence of statistical fluctuations, $\chi_{\delta_{CP}^{true}}^2 = 0$, and so equation 5.3 reduces to $\Delta\chi_{CP}^2 = \chi_{\delta_{CP}^{test}}^2$. This is what has been assumed throughout this study. It should be noted that the same Gaussian priors have been used in this simulation as were used in previous simulations.

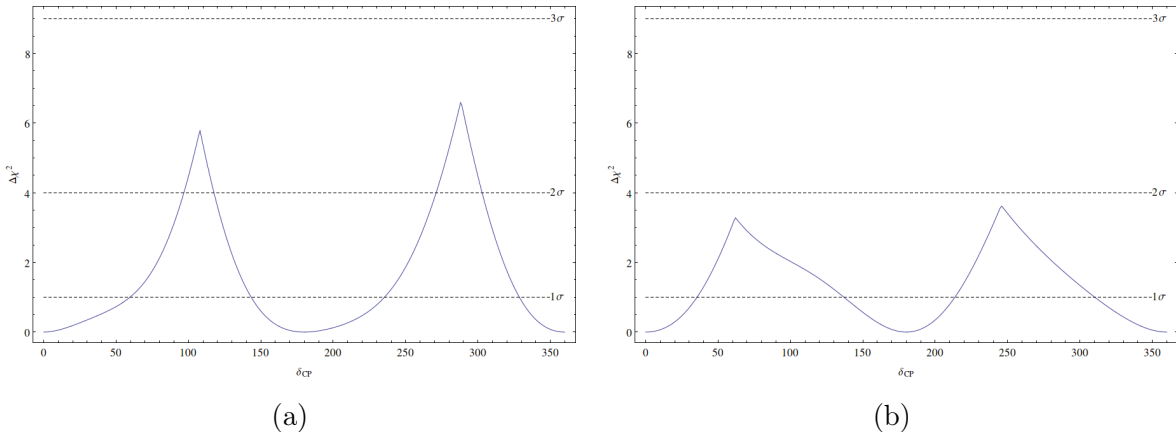


Figure 5.12: Plot of the $\Delta\chi_{CPV}^2$ test statistic as defined in equation 5.2, for the LBNE initial setup (1.2 MW, 80 GeV neutrino beam incident upon a 10 kt detector for 6 years), for the normal (a) and inverted (b) hierarchy.

Figure 5.12 shows a plot of this test statistic for different values of the true δ_{CP} . These plots show at what significance CP violation can be confirmed if the true value of δ_{CP} is the corresponding point on the axis. As such, if the true value of CPV is far away from $\delta_{CP} = 0, \pi$, then the significance to which CPV is confirmed will be much higher, and correspondingly, if $\delta_{CP} = 0, \pi$ then CP is not violated and so it cannot be confirmed to any significance.

As previously stated, LBNE is capable of delivering a beam of neutrinos or anti-neutrinos depending upon whether μ^+ or μ^- are used. By varying how much time is spent on detecting neutrinos/anti-neutrinos, the sensitivity to CPV can be varied. Plots of the test statistic defined in equation 5.2 for varying fractions of $\nu/\bar{\nu}$ can be found in figures 5.13 and 5.14. For both the normal hierarchy and the inverted hierarchy, the

greatest sensitivity can be achieved by running the neutrino and anti-neutrino beam for three years each.

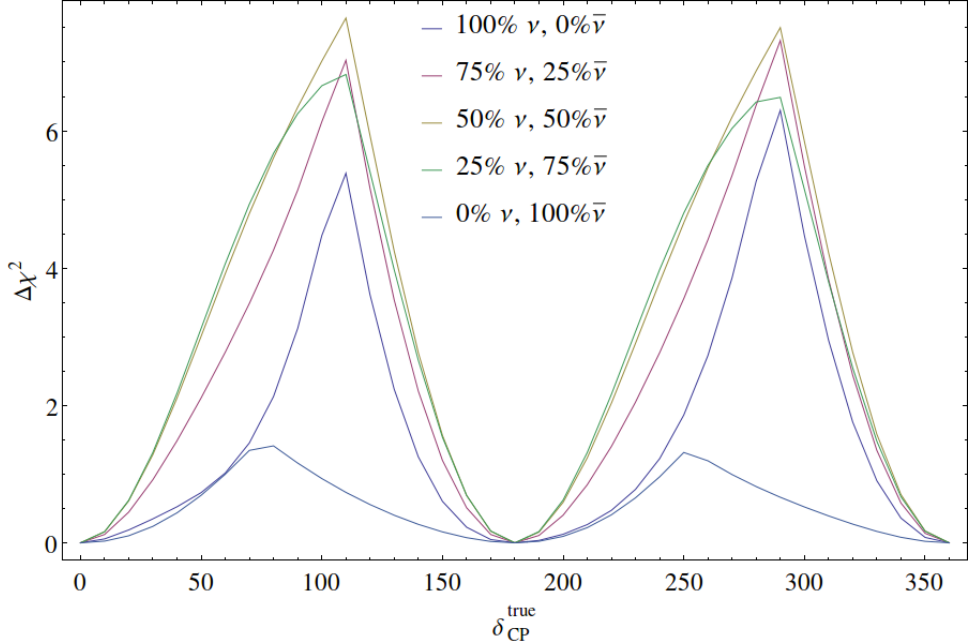


Figure 5.13: The test statistic of equation 5.2 for varying fractions of $\nu/\bar{\nu}$. These plots are calculated for the LBNE initial setup using oscillation parameters in the normal hierarchy. The percentages denote how much time of the 6 years are spent running neutrinos or antineutrinos.

This makes sense physically. If only a beam of either neutrinos or anti-neutrinos is used for six years, then only the number of appearance and disappearance events can be used to calculate the value of the CP violating phase. If both the neutrino and anti-neutrino beam are used, a comparison of the event probability shape for each of these beams may be studied and used to test CP violation. Fitting the theoretical probabilities to two sets of data (ν and $\bar{\nu}$) allows for much greater precision. In all of the following plots, it is assumed that LBNE is running with 50% ν and 50% $\bar{\nu}$, unless stated otherwise.

It is well known that the precision of the value of θ_{13} varies the CPV sensitivity of any particular experiment. By adding priors of varying amounts (2.5%, 5% and 10%), and performing further simulations, it can be shown that if Daya Bay, RENO, or any other SBL experiment is able to further constrain the value of θ_{13} , then access to CP violation will increase dramatically.

That varying the prior on θ_{13} can change the sensitivity so drastically should not be surprising. Looking at the Cervera, et al. probability calculated in equation 2.115, it is

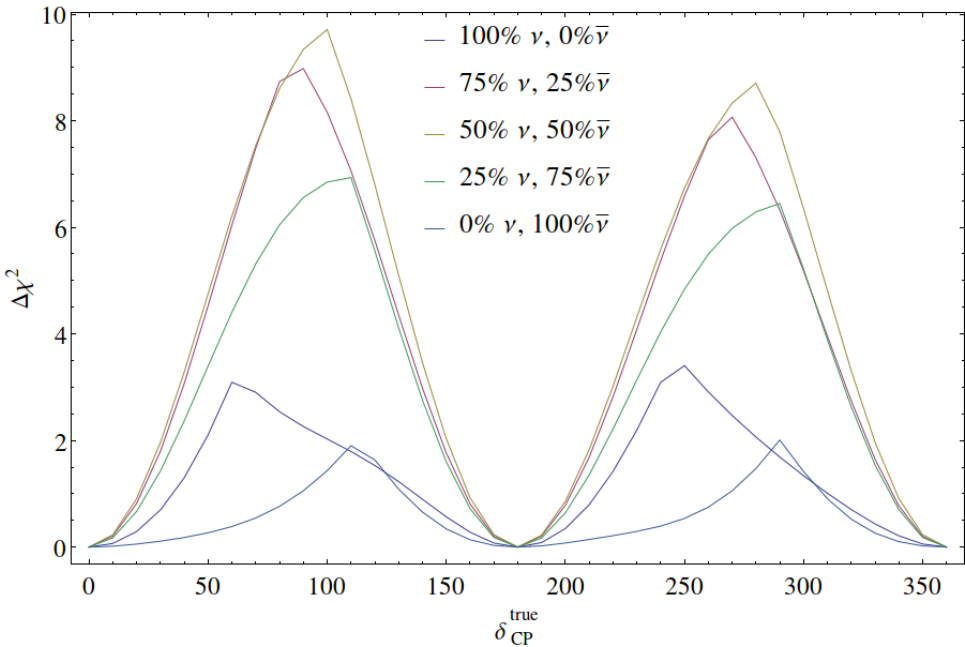


Figure 5.14: The test statistic of equation 5.2 for varying fractions of $\nu/\bar{\nu}$. Plots are calculated for the LBNE initial setup using oscillation parameters in the inverted hierarchy.

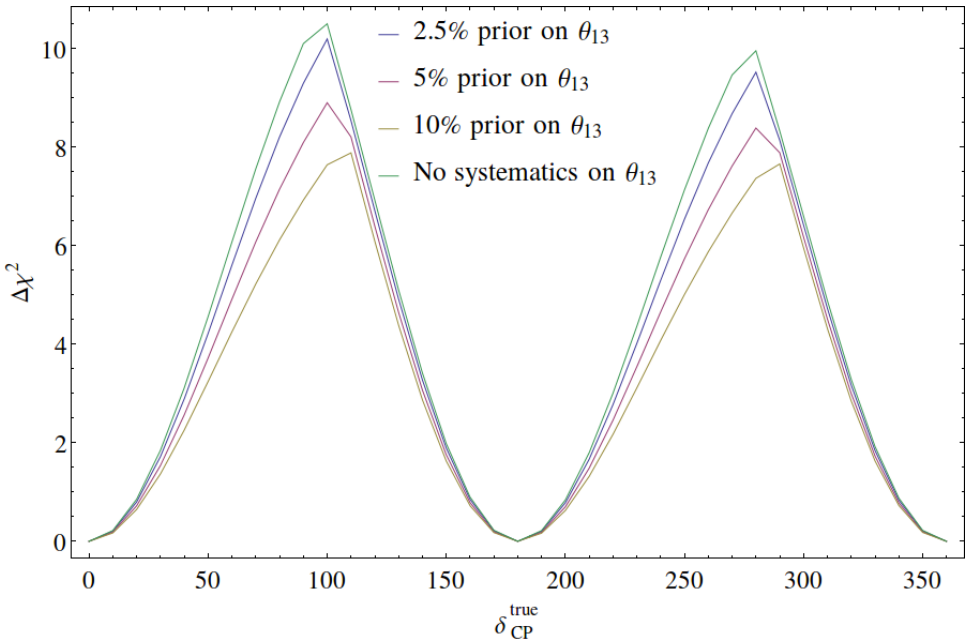


Figure 5.15: Variation in the sensitivity of LBNE to differing values of θ_{13} . Normal hierarchy is assumed, and priors on the other parameters are taken to be their 1σ values.

easily noticed that θ_{13} is the only mixing angle which appears in every term by virtue of being contained in the matter mixing angle. It therefore affects both the large and small contributions, and any variation will naturally cause a large change in probability.

The octant of θ_{23} also has a measurable affect on the sensitivity to δ_{CP} . If the true value is in the lower octant then the sensitivity to CP violation is increased somewhat.

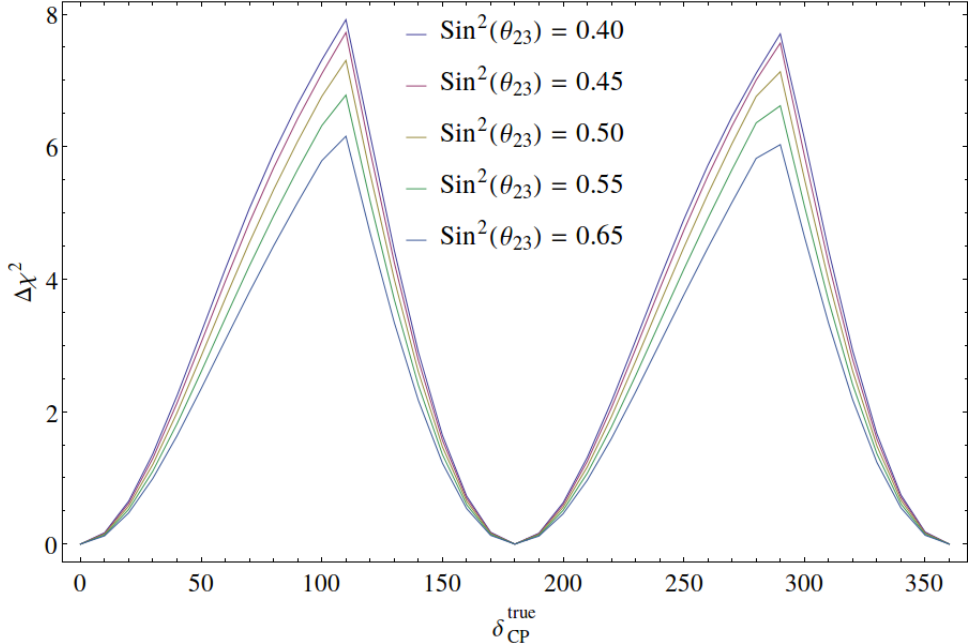


Figure 5.16: The χ^2_{CPV} test statistic for varying values of θ_{23} which are assumed to be known to infinite precision, allowing 1σ priors for all other parameters. Normal hierarchy is assumed.

This can be understood in terms of the Cervera, et al. probability (equation 2.115). To find how the error of δ_{CP} , $\Delta\delta_{CP}$ varies with respect to a changing θ_{23} , it must first be understood that the observable — the number of events — and the probability are linked. The event number relies on the probability, the neutrino-nucleon cross section, the neutrino flux and detector efficiencies, however by holding everything bar the probability constant, the event number and probability may be conflated, $N \propto P$. The propagation of error method may be applied here, as done in reference [58], by assuming that the error on the total number of events is largely dominated by Gaussian statistics, and so the error on the event number is given by $\Delta N \approx \sqrt{N}$, and so

$$\Delta N \approx \sqrt{N} = \left| \frac{\partial N}{\partial \delta_{CP}} \right| (\Delta \delta_{CP}). \quad (5.4)$$

By rearranging this and using $N \propto P$, the error on δ_{CP} can be given by

$$\Delta\delta_{CP} \propto \frac{\sqrt{P}}{\left| \frac{\partial P}{\partial\delta_{CP}} \right|}, \quad (5.5)$$

now, by noting from equation 2.115 that to leading order, $P \propto \sin^2(\theta_{23})$, and $\left| \frac{\partial P}{\partial\delta_{CP}} \right| \propto \sin(2\theta_{23})$,

$$\Delta\delta_{CP} \propto \frac{\sin(\theta_{23})}{\sin(2\theta_{23})} \propto \sec(\theta_{23}). \quad (5.6)$$

Hence the error on δ_{CP} increases as θ_{23} increases (within the allowed range), and as the chosen test statistic may provide a lower χ^2 value for higher values of θ_{23} .

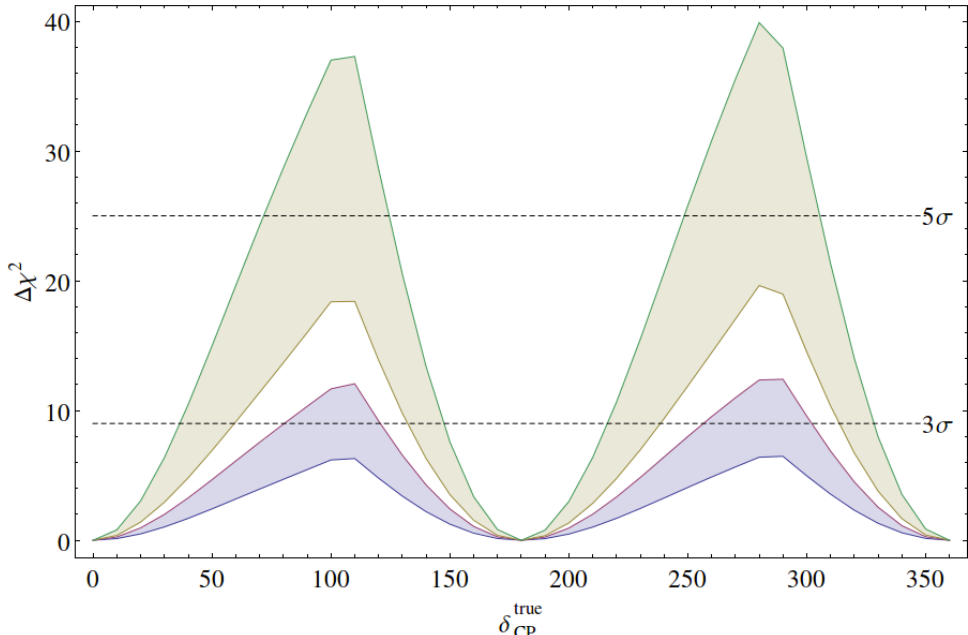


Figure 5.17: Sensitivity of LBNE to δ_{CP} . The blue band represents the sensitivities LBNE is capable of with a 10 kt detector, and the grey band represents the sensitivities with a 35 kt detector. The widths of the bands represent variation in the beamline setup and varying amounts of error on the signal and background normalisations. These simulations assume that no near detector is used, and that neutrinos and anti-neutrinos are each ran for 3 years.

Hitherto this point, simulations have focused on the initial setup to LBNE, without beam improvements, and with the relatively small 10 kt detector. With upgrades to the beamline and an increased mass of 35 kt, LBNE is expected to have a drastically improved sensitivity to the CP violating phase. This can be found by studying sensitivities

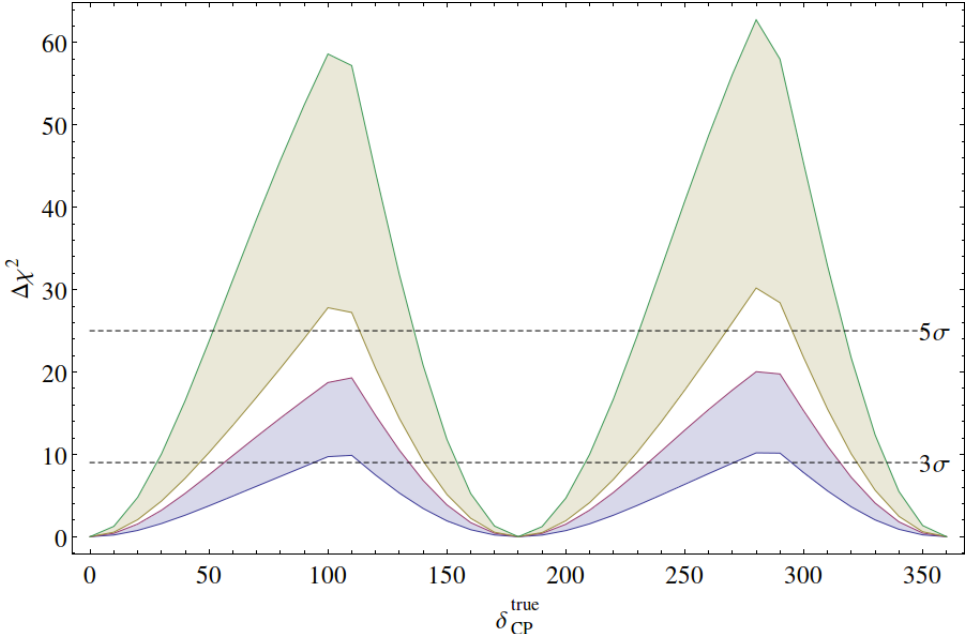


Figure 5.18: The same setup as figure 5.17, but with 5 year running times for $\nu/\bar{\nu}$.

in figure 5.17. Clearly increasing the mass of the detector gives the greatest increase in sensitivity to δ_{CP} , whilst varying the errors on signal and background normalisation along with beamline improvements also provide significant increases. These sensitivities can be further increased by increasing the run time of the experiment. LBNE is expected to have a lifetime of between 6 and 10 years in both its initial and final states. Simulations thus far have assumed 3 years of running for both neutrinos and anti-neutrinos, however by increasing this to 5 years for $\nu/\bar{\nu}$ the maximum sensitivity can be found. Plots of this can be found in figure 5.18.

From these plots it can be found that for the minimum setup with the greatest errors, LBNE will provide confirmation of CPV to 2σ for around 30% of true values of δ_{CP} . This is not particularly impressive, and leads to the position which the field is in now: δ_{CP} can take any value at 3σ . The outlook is far better with the final setup, allowing for 3σ confirmation for $\sim 70\%$ of the true values and 5σ confirmation for around 50% of the true values.

5.4.4 Study of the Octant of θ_{23}

As discussed in section 2.4, determining the value of θ_{23} is primarily going to be through disappearance channels, however for these simulations, both the disappearance and appearance channels have been used for increased sensitivities. Simulations in this section and the following two sections are done assuming 50% ν and 50% $\bar{\nu}$.

To analyse the octant determination, the general GLoBES χ^2 is used. For each true value of θ_{23} , a χ^2 for each test value in the wrong octant is determined, and the minimum of these is taken to be the χ^2 for the true θ_{23} . This means that for each true θ_{23} in the lower octant (higher octant), the test values run over the higher octant (lower octant). This has the effect of finding to what sensitivity LBNE can rule out the wrong octant for all possible values of θ_{23}^{true} .

Figure 5.19 shows a typical experiment with no systematics. This idealistic simulation shows that for the initial setup, for $\theta_{23} \lesssim 42$ or $\theta_{23} \gtrsim 50$, LBNE can determine rule out the wrong octant to 3σ .

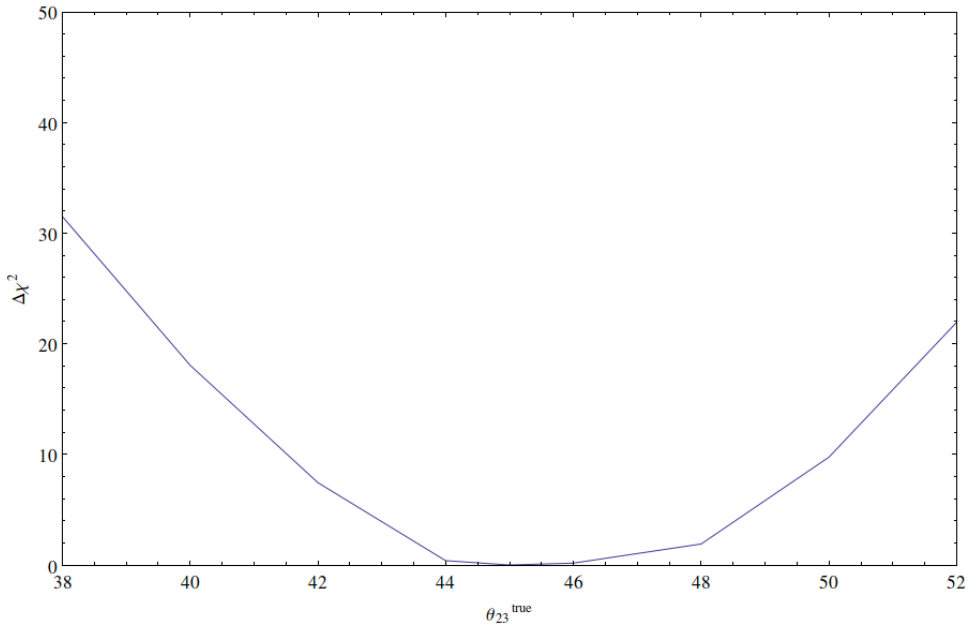


Figure 5.19: A typical study of octant determination with no priors. The significance for each θ_{23}^{true} determines to what significance the wrong hierarchy can be ruled out. This simulation is performed with systematics only.

As previously discussed in section 2.4.3, θ_{23} is highly dependant upon what precision θ_{13} is known to. This is demonstrated in figure 5.20. Allowing even a 10% uncertainty in the knowledge of θ_{13} leads to drastic consequences for determining the mass hierarchy. This further reinforces the need for smaller constraints on θ_{13} .

Figure 5.21a shows how sensitivities can be altered by beamline upgrades, reduction in error and changes in the fiducial mass of the detector for both mass hierarchies. LBNE

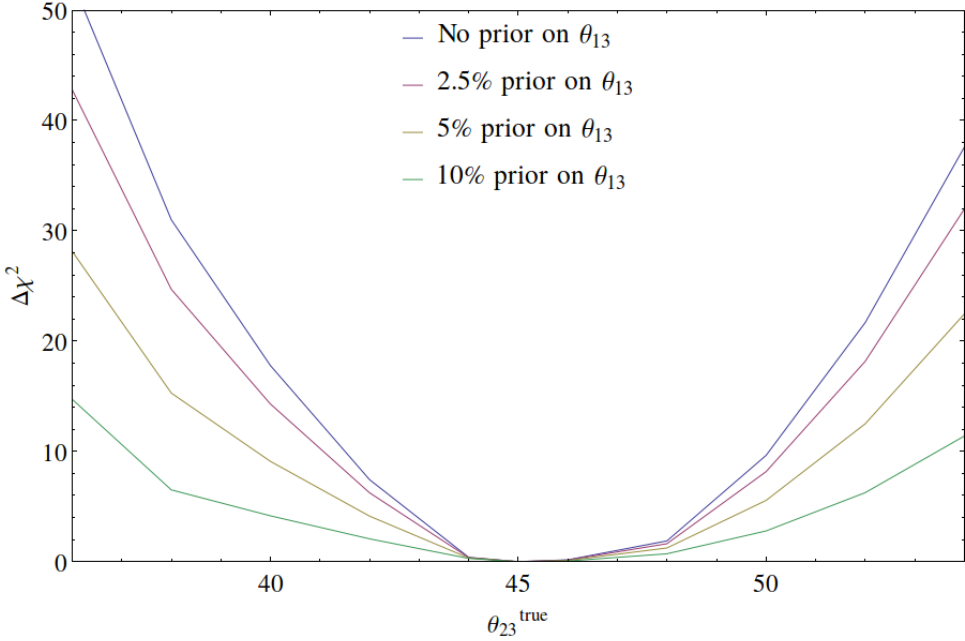


Figure 5.20: The effect of knowledge of θ_{13} on the determination of the octant of θ_{23} . No priors are used other than those placed upon θ_{13} .

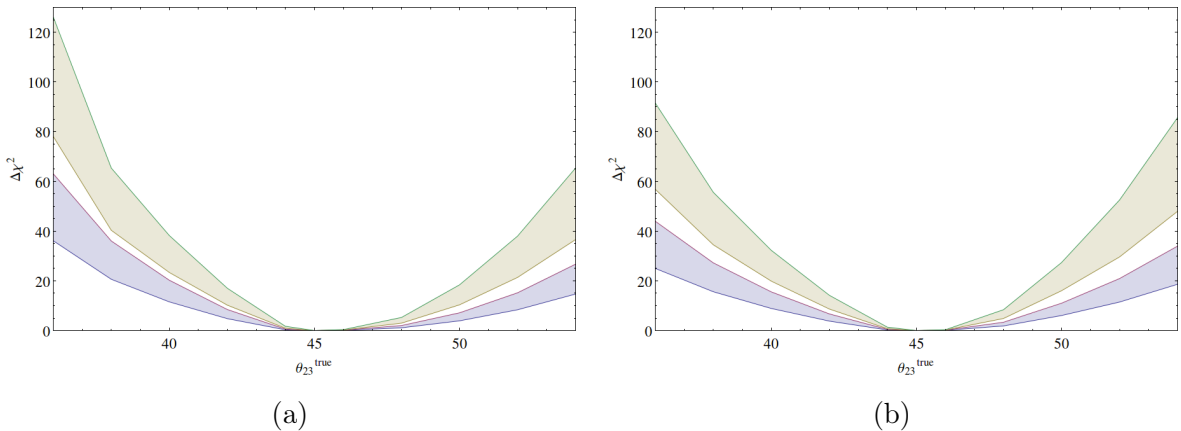


Figure 5.21: Sensitivities for octant sensitivity in (a) the normal hierarchy and (b) the inverted hierarchy. Each band represents variation in the beamline design and signal and background normalisation errors. The top band is for the 35 kt detector and the bottom band is for the initial 10 kt detector.

— like all experiments — will be more able to remove the wrong hierarchy if the true mixing angle is far from maximal. For the current best fit values, 42.2° and 49.4° in the lower and higher octants respectively, the wrong octant should be able to be ruled out with greater than 3σ precision. This is expected to be improved with an extension from a 6 year to 10 year running time.

The importance of simulations within neutrino oscillation physics cannot be over-

emphasised, and this is particularly important for upcoming experiments such as LBNE. GLoBES simulations can be used to predict the physics reach of experiments with different setups within a relatively short time, and so test how effective different setups would be to discovering the mass hierarchy, CPV, the octant of θ_{23} and constraining the values of the oscillation parameters.

Further to standard neutrino oscillation physics, LBNE, along with other future oscillation experiments, is expected to be in a position to probe BSM physics including GUT theories and the existence of so-called sterile neutrinos. Recent fits of cosmological data have a slight preference to the existence of more than three neutrinos, and this may help to explain the electron appearance anomalies at LSND [59], MiniBOONE [60] and other SBL experiments [61]. Analysis of the ability of LBNE to detect such sterile neutrinos has recently been carried out in [62], where it is found that without further constraint of δ_{CP} , there are certain scenarios in which a sterile neutrino cannot be differentiated from the sterile neutrinos.

Chapter 6

Summary and Conclusions

Neutrino oscillations mark a hugely important milestone in the history of physics. They are understood to be the first sign of physics beyond the Standard Model and have implications in many areas of research. This dissertation has surveyed the theoretical and experimental status of neutrino oscillations, and as such can be roughly split in to two parts. The first part of this dissertation focused on the theory of neutrino oscillations under several levels of rigour in both vacuum and matter, finding that the phenomena have mathematical descriptions even using quantum field theory. They are mathematically robust, seeming to hold up under close scrutiny from Quantum Field Theory. The “stepped” approach to studying oscillations, $2\nu^{vac} \rightarrow 3\nu^{vac} \rightarrow 2\nu^{mat} \rightarrow 3\nu^{mat}$, has been used so that the theory is accessible. The second part analysed neutrino oscillation experiments, studying each species value in determining the different oscillation parameters and providing a simulation of the future *Long Baseline Neutrino Experiment* complete with a statistical overview of the field. The aim of this, and indeed, the aim of the field at large is to answer the three big questions of neutrino physics:

- i What is the true mass hierarchy?
- ii Is CP violation manifest in the leptonic sector?
- iii What is the octant of the θ_{23} ?

This means that, to be reductionist, the current main aim of the community is the last of the above questions: is CP violated? This is not without good reason; revelation of CPV in the leptonic sector would have consequences throughout high energy physics, and in particular it could provide a leading explanation for the baryon asymmetry of the universe through leptogenesis. The next generation of neutrino oscillations, including LBNE, seem poised to constrain the value of the δ_{CP} and could provide evidence of CPV

for the largest values of δ_{CP} .

Simulations of LBNE suggest that even for the initial beamline setup with the lowest mass detector it should be able to give guidance on the true mass hierarchy and true octant of θ_{23} . Should funding for the final setup be found, these sensitivities should be increased such that the Mass hierarchy should be confirmed to greater than 99.9996% accuracy [45], and the octant could be confirmed to different sensitivities dependant upon the true value of θ_{23} . These results, along with results from simulations of other future long baseline experiments suggest that the eight-fold degeneracy could be lifted within the next generation of neutrino oscillation experiments.

Appendix A

Finite Normalisation Volume Method

In order to have orthonormal massive neutrino states, a finite normalisation volume can be defined. In practice, the normalisation volume can be kept constant throughout the calculation, and then the limit to infinity can be taken upon completion.

For convenience, the volume is assumed to be $V = L^3$, where L is the length of one of its sides. Periodic boundary condition can then be imposed upon the system, and (in analogy with a particle in a box) this implies that the momentum \vec{p} is quantised [27],

$$\vec{p} = \frac{2\pi}{L} \vec{n}, \quad (\text{A.1})$$

with $\vec{n} = (n_1, n_2, n_3)$ and $n_i = 0, \pm 1, \pm 2, \dots$. Within quantum field theory, a field may be Fourier expanded such as

$$\psi(x) = \int \frac{d^3 p}{(2\pi)^3} \frac{1}{\sqrt{2E}} \sum_h (a_p^h u^h(p) e^{-ip \cdot x} + b_p^{h\dagger} v^h(p) e^{ip \cdot x}), \quad (\text{A.2})$$

where the creation and annihilation relations obey the anti-commutation relations,

$$\{a_p^h, a_q^{s\dagger}\} = \{b_p^h, b_q^{s\dagger}\} = (2\pi)^3 \delta^{(3)}(p - q) \delta^{hs}. \quad (\text{A.3})$$

The discrete form of this equation can be obtained by using the replacements

$$\int \frac{d^3 p}{(2\pi)^3} \rightarrow \frac{1}{\sqrt{V}} \sum_{\vec{p}}, \quad (2\pi)^3 \delta^{(3)}(p - q) \rightarrow V \delta^{pq}, \quad (\text{A.4})$$

which gives the Fourier expansion for the field and anti-commutation relations,

$$\psi(x) = \frac{1}{\sqrt{V}} \sum_p \frac{1}{\sqrt{2E_p}} \sum_h (a_p^h u^h(p) e^{-ip \cdot x} + b_p^{h\dagger} v^h(p) e^{ip \cdot x}), \quad (\text{A.5})$$

$$\{a_p^h, a_q^{s\dagger}\} = \{b_p^h, b_q^{s\dagger}\} = 2EV \delta^{pq} \delta^{rs}. \quad (\text{A.6})$$

Because the volume has been chosen to be finite, single particle states can be defined

$$|f(p, h)\rangle = \frac{1}{\sqrt{2EV}} a_p^{h\dagger} |0\rangle, \quad |\bar{f}(p, h)\rangle = \frac{1}{\sqrt{2EV}} b_p^{h\dagger} |0\rangle, \quad (\text{A.7})$$

and by taking an inner product, these states can be seen to be properly normalised to one,

$$\langle f(p, h) | f(q, s) \rangle = \langle \bar{f}(p, h) | \bar{f}(q, s) \rangle = \delta^{hs} \delta^{pq}. \quad (\text{A.8})$$

Appendix B

Probability Calculations

B.1 One Mass-Squared Dominance

For studying the case of octant degeneracy, it is enough to use the one mass-squared dominance (OMSD) case, which effectively means dropping any dependence upon the smaller mass-squared difference, Δm_{21}^2 . This can be done so long as two conditions are met:

- i One mass squared splitting is much larger than the others. In the three neutrino case $\Delta m_{21}^2 \ll \Delta m_{31}^2$ is satisfied as there is a difference of two orders of magnitude between the values.
- ii $\frac{\Delta m_{21}^2 L}{E} \ll 1$. This equates to $L/E \ll 10^4$ km/GeV, which is satisfied for a large majority of neutrinos.

To approximately remove dependence on the smaller mass-squared difference, equation 2.16 must first be split in to contributions from the dominant term and the sub-dominant terms,

$$P_{\nu_\alpha \rightarrow \nu_\beta}(t) = \left| \sum_{j=1,2} U_{\alpha j}^* U_{\beta j} \exp\left(-i \frac{\Delta m_{j1}^2 L}{2E}\right) + U_{\alpha 3}^* U_{\beta 3} \exp\left(-i \frac{\Delta m_{31}^2 L}{2E}\right) \right|^2. \quad (\text{B.1})$$

The phases of the first term can be neglected due to the OMSD approximation,

$$P_{\nu_\alpha \rightarrow \nu_\beta}(t) = \left| \sum_{j=1,2} U_{\alpha j}^* U_{\beta j} + U_{\alpha 3}^* U_{\beta 3} \exp\left(-i \frac{\Delta m_{31}^2 L}{2E}\right) \right|^2. \quad (\text{B.2})$$

Now, by using the unitarity of the mixing matrix, $\sum_j U_{\alpha j}^* U_{\beta j} = \delta_{\alpha\beta}$, and rearranging such that

$$\sum_{j=1,2} U_{\alpha j}^* U_{\beta j} + U_{\alpha 3}^* U_{\beta 3} = \delta_{\alpha\beta}, \quad (\text{B.3})$$

then equation B.2 can be rearranged as such:

$$P_{\nu_\alpha \rightarrow \nu_\beta}(t) = \left| \delta_{\alpha\beta} - U_{\alpha 3}^* U_{\beta 3} \left[1 - \exp \left(-i \frac{\Delta m_{31}^2 L}{2E} \right) \right] \right|^2, \quad (\text{B.4})$$

neglecting the case in which $\alpha = \beta$, then this can be rewritten as

$$P_{\nu_\alpha \rightarrow \nu_\beta}(t) = |U_{\alpha 3}^* U_{\beta 3}|^2 \left| -1 + \exp \left(-i \frac{\Delta m_{31}^2 L}{2E} \right) \right|^2, \quad (\text{B.5})$$

and by Eulars formula and trigonometric identities, this can be given as

$$P_{\nu_\alpha \rightarrow \nu_\beta}(t) = 4|U_{\alpha 3}^* U_{\beta 3}|^2 \sin^2 \left(\frac{\Delta m_{31}^2 L}{4E} \right). \quad (\text{B.6})$$

As the assumption that $\alpha \neq \beta$ has been made, the oscillation probability for $\nu_\mu \rightarrow \nu_\mu$ i.e. the survival probability, must be determined by

$$P_{\nu_\mu \rightarrow \nu_\mu} = 1 - (P_{\nu_\mu \rightarrow \nu_e} + P_{\nu_\mu \rightarrow \nu_\tau}) \quad (\text{B.7})$$

$$= 1 - \left(4|U_{\mu 3}^* U_{e3}|^2 \sin^2 \left(\frac{\Delta m_{31}^2 L}{4E} \right) + 4|U_{\mu 3}^* U_{\tau 3}|^2 \sin^2 \left(\frac{\Delta m_{31}^2 L}{4E} \right) \right) \quad (\text{B.8})$$

$$= 1 - 4(|U_{\mu 3}^* U_{e3}|^2 + |U_{\mu 3}^* U_{\tau 3}|^2) \sin^2 \left(\frac{\Delta m_{31}^2 L}{4E} \right) \quad (\text{B.9})$$

$$= 1 - c_{13}^2 \sin^2(2\theta_{23}) \sin^2 \left(\frac{\Delta m_{31}^2 L}{4E} \right) - s_{23}^4 \sin^2(2\theta_{13}) \sin^2 \left(\frac{\Delta m_{31}^2 L}{4E} \right). \quad (\text{B.10})$$

B.2 Asano-Minakata Probability

The Cervera et al. probability from reference [37] can be further improved upon by expanding in the small parameters (including θ_{13}) as done in reference [33]. This approach is called $\sqrt{\epsilon}$ perturbation theory as the ansatz

$$s_{13} \simeq \sqrt{\epsilon}, \quad \epsilon \equiv \frac{\Delta m_{21}^2}{\Delta m_{31}^2} \simeq 0.03, \quad (\text{B.11})$$

is made. To begin, it is useful to define some notation: $r_A \equiv a/\Delta m_{31}^2$, where $a \equiv 2\sqrt{2}G_F N_e E$, $\Delta \equiv \Delta_{31} = \Delta m_{31}^2/2E$, and $r_\Delta = \frac{\Delta m_{21}^2}{\Delta m_{31}^2}$. In analogy with reference [33], the

S -matrix formulation will be used, i.e.

$$\nu_\alpha(L) = S_{\alpha\beta}\nu_\beta(0), \quad (\text{B.12})$$

and this indicates that, as before, the probability can be found by the square of the amplitude which accompanies ν_β ,

$$P_{\nu_\alpha \rightarrow \nu_\beta} = |S_{\alpha\beta}|^2. \quad (\text{B.13})$$

Provided that the evolution of the neutrino state is governed by the Schrödinger equation, as is assumed through this work, then the S -matrix can be formalised as

$$S = T \exp \left[-i \int_0^L dx \mathcal{H}(x) \right], \quad (\text{B.14})$$

where the T refers to time ordering (or in this case, space ordering, as the time dependence is removed, as done earlier). The right hand side can also be written as $\exp[-i\mathcal{H}L]$. For notational convenience it is useful to denote the S -matrix in a similar way to the PMNS matrix,

$$S = \begin{pmatrix} S_{ee} & S_{e\mu} & S_{e\tau} \\ S_{\mu e} & S_{\mu\mu} & S_{\mu\tau} \\ S_{\tau e} & S_{\tau\mu} & S_{\tau\tau} \end{pmatrix}, \quad (\text{B.15})$$

and define a second basis, the tilde basis in this case, such that

$$\mathcal{H} = U_{23}^\dagger \tilde{\mathcal{H}} U_{23}, \quad (\text{B.16})$$

which implies that

$$S = U_{23} \tilde{S} U_{23}^\dagger. \quad (\text{B.17})$$

This means that the new tilde basis does not contain θ_{23} . In this new basis, the S -matrix can be parametrised as in reference [65],

$$\begin{pmatrix} \tilde{S}_{ee} & c_{23}\tilde{S}_{e\mu} + s_{23}\tilde{S}_{e\tau} & -s_{23}\tilde{S}_{e\mu} + c_{23}\tilde{S}_{e\tau} \\ c_{23}\tilde{S}_{\mu e} + s_{23}\tilde{S}_{\tau e} & c_{23}^2\tilde{S}_{\mu\mu} + s_{23}^2\tilde{S}_{\tau\tau} + c_{23}s_{23}(\tilde{S}_{\mu\tau} + \tilde{S}_{\tau\mu}) & c_{23}^2\tilde{S}_{\mu\tau} - s_{23}^2\tilde{S}_{\tau\mu} + c_{23}s_{23}(\tilde{S}_{\tau\tau} - \tilde{S}_{\mu\mu}) \\ -s_{23}\tilde{S}_{\mu e} + c_{23}\tilde{S}_{\tau e} & c_{23}^2\tilde{S}_{\tau\mu} - s_{23}^2\tilde{S}_{\mu\tau} + c_{23}s_{23}(\tilde{S}_{\mu\tau} - \tilde{S}_{\tau\mu}) & s_{23}^2\tilde{S}_{\mu\tau} - c_{23}^2\tilde{S}_{\tau\mu} + c_{23}s_{23}(\tilde{S}_{\mu\tau} - \tilde{S}_{\tau\mu}) \end{pmatrix}. \quad (\text{B.18})$$

As in the calculation of the Cervera et al. probability performed in section 2.3.3, \mathcal{H}

is given as

$$\mathcal{H} = \frac{1}{2E} \left[U \begin{pmatrix} 0 & 0 & 0 \\ 0 & \Delta m_{21}^2 & 0 \\ 0 & 0 & \Delta m_{31}^2 \end{pmatrix} U^\dagger + \begin{pmatrix} a & 0 & 0 \\ 0 & 0 & 0 \\ 0 & 0 & 0 \end{pmatrix} \right], \quad (\text{B.19})$$

where $a = 2EV_{cc}$ has been used in analogy with the paper. Now, by changing to the tilde basis and splitting the Hamiltonian in to its unperturbed state, \mathcal{H}_0 , plus perturbations, \mathcal{H}_1 , it can be written:

$$\tilde{\mathcal{H}}_0 = \Delta_{31} \begin{pmatrix} r_A 0 & 0 & 0 \\ 0 & 0 & 0 \\ 0 & 0 & 1 \end{pmatrix}, \quad (\text{B.20})$$

$$\begin{aligned} \tilde{\mathcal{H}}_1 = & \Delta_{31} \begin{pmatrix} 0 & 0 & s_{13}e^{-i\delta} \\ 0 & 0 & 0 \\ s_{13}e^{-\delta} & 0 & 0 \end{pmatrix} + \Delta_{31} \begin{pmatrix} r_\Delta s_{12}^2 + s_{13}^2 & r_\Delta c_{12}s_{12} & 0 \\ r_\Delta c_{12}s_{12} & r_\Delta c_{12}^2 & 0 \\ 0 & 0 & -s_{13}^2 \end{pmatrix} \\ & - \Delta_{31} \begin{pmatrix} 0 & 0 & (r_\Delta s_{12}^2 + \frac{1}{2}s_{13}^2)s_{13}e^{-i\delta} \\ 0 & 0 & r_\Delta c_{12}s_{12}s_{13}e^{-i\delta} \\ (r_\Delta s_{12}^2 + \frac{1}{2}s_{13}^2)s_{13}e^{i\delta} & r_\Delta c_{12}s_{12}s_{13}e^{i\delta} & 0 \end{pmatrix}, \\ & - \Delta r_\Delta \begin{pmatrix} s_{12}^2 s_{13}^2 & \frac{1}{2}c_{12}s_{12}s_{13}^2 & 0 \\ \frac{1}{2}c_{12}s_{12}s_{13}^2 & 0 & 0 \\ 0 & 0 & -s_{12}^2 s_{13}^2 \end{pmatrix}, \end{aligned} \quad (\text{B.21})$$

where the notation defined at the start of this section has been used. Each term of $\tilde{\mathcal{H}}_1$ is increasing in order of ϵ . The first term is $\mathcal{O}(\epsilon^{\frac{1}{2}})$, followed by $\mathcal{O}(\epsilon^1), \mathcal{O}(\epsilon^{\frac{3}{2}})$ and $\mathcal{O}(\epsilon^2)$ respectively. By methods outlined in B.2.1, the \tilde{S} -matrix elements can be calculated, and so the probability can be found. For example, the probability for the $\nu_e \rightarrow \nu_\mu$ transition can be found to be

$$\begin{aligned} P_{\nu_e \rightarrow \nu_\mu} = |S_{\mu e}|^2 = & s_{23}^2 |\tilde{S}_{e\tau}^{1/2}(-\delta)|^2 + 2c_{23}s_{23} \operatorname{Re} \left[\tilde{S}_{e\tau}^{1/2}(-\delta) \tilde{S}_{e\mu}^1(-\delta) \right] \\ & + c_{23}^2 |\tilde{S}_{e\mu}^1(-\delta)|^2 + 2s_{23}^2 \operatorname{Re} \left[\tilde{S}_{e\tau}^{1/2}(-\delta) \tilde{S}_{e\tau}^{3/2}(-\delta) \right] \end{aligned} \quad (\text{B.22})$$

By plugging in the values of the \tilde{S} -matrix elements, the probability can be found to be

$$\begin{aligned}
P_{\nu_e \rightarrow \nu_\mu} = & 4s_{23}^2 s_{13} \frac{1}{(1 - r_A)^2} \sin^2 \left(\frac{(1 - r_A)\Delta_{31}L}{2} \right) \\
& + 8J_r \frac{r_\Delta}{r_A(1 - r_A)} \cos \left(\delta - \frac{\Delta_{31}L}{2} \right) \sin \left(\frac{r_A\Delta_{31}L}{2} \right) \sin \left(\frac{(1 - r_A)\Delta_{31}L}{2} \right) \\
& + 4c_{23}^2 c_{12}^2 s_{12}^2 \left(\frac{r_\Delta}{r_A} \right)^2 \sin^2 \left(\frac{r_A\Delta_{31}L}{2} \right) \\
& - 4s_{23}^2 \left[s_{13}^2 \frac{(1 + r_A)^2}{(1 - r_A)^4} - 2s_{12}^2 s_{13}^2 \frac{r_\Delta r_A}{(1 - r_A)^3} \right] \sin^2 \left(\frac{(1 - r_A)\Delta_{31}L}{2} \right) \\
& + 2s_{23}^2 \left[2s_{13}^4 \frac{r_A}{(1 - r_A)^3} - s_{12}^2 s_{13}^2 \frac{r_\Delta}{(1 - r_A)^2} \right] \Delta_{31}L \sin((1 - r_A)\Delta_{31}L),
\end{aligned} \tag{B.23}$$

where J_r is the reduced Jarlskog coefficient, $J_r = c_{12}s_{12}c_{23}s_{23}s_{13}$.

It has been found that even in the limit where θ_{13} is relatively large (around the Chooz limit, $\simeq 10^\circ$), the Asano-Minakata probability provides a closer approximation than the Cervera et al. probability [33].

B.2.1 Example Calculation of an S-Matrix Element

To calculate \tilde{S} -matrix elements perturbatively,

$$\Omega(x) = e^{i\tilde{\mathcal{H}}_0} \tilde{S}(x), \tag{B.24}$$

is defined, which obeys the evolution equation, given as

$$i \frac{d}{dx} \Omega(x) = \mathcal{H}_1 \Omega(x), \tag{B.25}$$

where \mathcal{H}_1 is related to the Hamiltonian in the tilde basis by

$$\mathcal{H}_1 = e^{i\tilde{\mathcal{H}}_0 x} \tilde{\mathcal{H}}_1 e^{-i\tilde{\mathcal{H}}_0 x}. \tag{B.26}$$

\tilde{S} can then be calculated by

$$\tilde{S}(x) = e^{-i\tilde{\mathcal{H}}_0 x} \Omega(x), \tag{B.27}$$

where $\Omega(x)$ can be calculated perturbatively by

$$\begin{aligned}\Omega(x) = & 1 + (-i) \int_0^x dx' \mathcal{H}_1(x') + (-i)^2 \int_0^x dx' \mathcal{H}_1(x') \int_0^{x'} dx'' \mathcal{H}_1(x'') \\ & + (-i)^2 \int_0^x dx' \mathcal{H}_1(x') \int_0^{x'} dx'' \mathcal{H}_1(x'') \int_0^{x''} dx''' \mathcal{H}_1(x''') + \mathcal{O}(\epsilon^4)\end{aligned}. \quad (\text{B.28})$$

For the purpose of illustrating the calculation of each element of the \tilde{S} -matrix, $\tilde{S}_{e\tau}^{1/2}$ will now be calculated. In this case, only the $\mathcal{O}(\epsilon^{1/2})$ need be taken in to account, which corresponds to the first second term in $\Omega(x)$.

$$\Omega^{1/2}(x) = -i \int_0^x dx' \mathcal{H}_1(x'), \quad (\text{B.29})$$

$$= -i \int_0^x dx' e^{i\tilde{\mathcal{H}}_0 x'} \tilde{\mathcal{H}}_1 e^{-i\tilde{\mathcal{H}}_0 x'}, \quad (\text{B.30})$$

$$= -i \Delta_{31} s_{13} \int_0^x dx' \begin{pmatrix} 0 & 0 & e^{-i\delta} e^{-i(1-r_A)\Delta_{31}x'} \\ 0 & 0 & 0 \\ e^{i\delta} e^{i(1-r_A)\Delta_{31}x'} & 0 & 0 \end{pmatrix}, \quad (\text{B.31})$$

$$= \begin{pmatrix} 0 & 0 & \frac{s_{13}e^{-i\delta}}{1-r_A} (e^{-i(1-r_A)\Delta_{31}x} - 1) \\ 0 & 0 & 0 \\ -\frac{s_{13}e^{i\delta}}{1-r_A} (e^{i(1-r_A)\Delta_{31}x} - 1) & 0 & 0 \end{pmatrix}, \quad (\text{B.32})$$

$$= \begin{pmatrix} 0 & 0 & \frac{s_{13}e^{-i\delta}}{1-r_A} (e^{-i\Delta_{31}x} - e^{-ir_A\Delta_{31}x}) \times \\ 0 & 0 & 0 \\ \frac{s_{13}e^{i\delta}}{1-r_A} (e^{-i\Delta_{31}x} e^{-ir_A\Delta_{31}x}) \times & 0 & 0 \end{pmatrix}, \quad (\text{B.33})$$

$$= e^{i\tilde{\mathcal{H}}_0 x} \begin{pmatrix} 0 & 0 & \frac{s_{13}e^{-i\delta}}{1-r_A} (e^{-i\Delta_{31}x} - e^{-ir_A\Delta_{31}x}) \\ 0 & 0 & 0 \\ \frac{s_{13}e^{i\delta}}{1-r_A} (e^{-i\Delta_{31}x} e^{-ir_A\Delta_{31}x}) & 0 & 0 \end{pmatrix}, \quad (\text{B.34})$$

where in the third line, the exponentials have been used on the unperturbed Hamiltonian, and the matrix multiplication has been carried out. The important point to note here is that $e^{i\tilde{\mathcal{H}}_0 x}$ has been pulled out of the matrix in the last step. This means that when we calculate the \tilde{S} -matrix element using equation B.27, the phases will cancel. By looking at the parametrisation of the S -matrix earlier, it can be seen that for $\tilde{S}_{e\tau}$, only the top

right element of the matrix needs to be considered, and so the final matrix element is given by

$$\tilde{S}_{e\tau}^{1/2} = s_{13} e^{-i\delta} \frac{1}{(1 - r_A)} (e^{-i\Delta_{31}x} - e^{-ir_A\Delta_{31}x}) \quad (\text{B.35})$$

It is also worth noting that $\tilde{S}_{e\tau}^{1/2}$ and $\tilde{S}_{\tau e}^{1/2}$ are related by a transformation of $\delta \rightarrow -\delta$. This is not peculiar, all T conjugate probabilities can be found by sending $\tilde{S}_{\alpha\beta}(\delta) \rightarrow \tilde{S}_{\beta\alpha}(-\delta)$

Appendix C

GLoBES Statistics

In this appendix, the statistics of GLoBES simulations will be discussed. To produce χ^2 plots, GLoBES takes three main pieces of information. AEDL files contain a **description of the experiment** currently being simulated, including information such as the fiducial mass of the detector, the run time of the experiment, and the energy range over which the detector is sensitive. The AEDL file calls several other files which contain information on the **neutrino flux** and **neutrino-nucleon cross-sections** for both NC and CC interactions.

By defining a vector of “true” parameters, which are understood to be as nature has chosen, GLoBES can produce a simulated number of events over a spectrum of energy. This energy spectrum is split into a number of bins, and each bin is assigned a number of events which is representative of the interval. This data represents the data that would be expected in the real experiment. A vector of hypothesised parameters can then be defined, and the process is repeated so that there are two binned energy spectra, such as in figure C.1.

As discussed in section 4, the test statistic implemented by GLoBES is given by equation C.1,

$$\Delta\chi^2 = -2 \ln(\lambda) = 2 \sum_i^{\#bins} y_i - n_i + n_i \ln\left(\frac{n_i}{y_i}\right). \quad (\text{C.1})$$

This asymptotically takes the form of a chi-squared distribution (and so is given the label $\Delta\chi^2$) and this is a result of *Wilks theorem*.

To further improve the accuracy of GLoBES simulations, nuisance parameters called *pulls* are introduced to simulate the effects of systematic uncertainties [63]. These pulls are taken to be random variables treated with simple Gaussian statistics, which vary

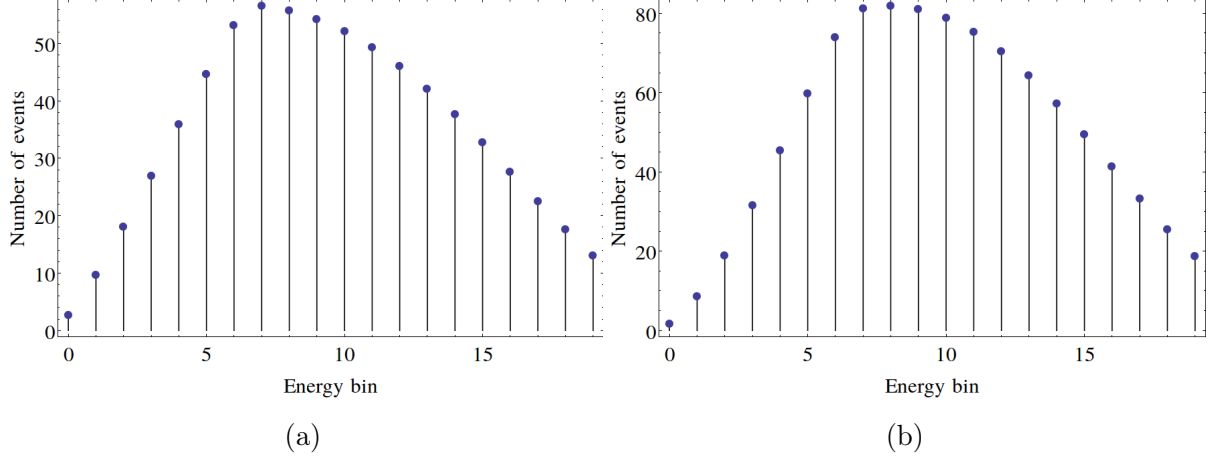


Figure C.1: Plots showing number of events against binned energy data for the true parameters (a) and hypothesised parameters with a different value of δ_{CP} (b).

about zero with some standard deviation σ . For example, the total number of events in the i^{th} bin, n_i , can be split in to background rates, n_i^b , and signal rates, n_i^s , and the pulls for the background and signal rates (ζ^b and ζ^s , respectively) act on these as shown in equation C.2,

$$n_i(\zeta^s, \zeta^b) = n_i^s(1 + \zeta^s) + n_i^b(1 + \zeta^b). \quad (\text{C.2})$$

To ensure that values of the pulls far from their peak value are disfavoured, an extra term must be included in the $\Delta\chi^2$,

$$\Delta\chi^2_{Pulls} = \left(\frac{\zeta^s}{\sigma^s}\right)^2 + \left(\frac{\zeta^b}{\sigma^b}\right)^2. \quad (\text{C.3})$$

The equation provided in the GLoBES manual [64] lists the $\Delta\chi^2$ as

$$\Delta\chi^2 = \sum_{i=1}^{\#bins} \sum_{d=N,F} \frac{(O_{d,i} - (1 + a_R + a_d)T_{d,i})^2}{O_{d,i}} + \frac{a_R^2}{\sigma_R^2} + \frac{a_N^2}{\sigma_N^2} + \frac{a_F^2}{\sigma_F^2}, \quad (\text{C.4})$$

where $O_{N,i}$ and $O_{F,i}$ are the true event rates for the near and far detector in the i^{th} bin and T is the event rates for the parameters currently being tested. The a_R , a_N , and a_F terms act as the pulls here, with inclusion in the chi squared term plus the penalty terms.

The final improvement made by GLoBES to the standard $\Delta\chi^2$ is to include information from other experiments by adding Gaussian *priors*, as discussed in section 4. These essentially provide the likelihood that our oscillation parameters θ_i take values θ_i^0 , and are included by adding another term,

$$\Delta\chi^2_{Priors} = \sum_i^{\#priors} \left(\frac{\theta_i - \theta_i^0}{\sigma_{\theta_i}} \right)^2. \quad (\text{C.5})$$

By minimising over all of the nuisance parameters in order to introduce an error to the overall signal normalisation, the final $\Delta\chi^2$ is seen to be

$$\Delta\chi^2 = \min_{\{\zeta_i\}} (\Delta\chi^2_{Bins}(\zeta^s, \zeta^b) + \Delta\chi^2_{Pulls}) + \Delta\chi^2_{Priors}. \quad (\text{C.6})$$

The value $\Delta\chi^2$ is a measure of the goodness of fit of the hypothesis, the closer to zero the value, the better the fit. By computing this over a range of values of a parameter of interest, and minimising over the rest of the parameters, confidence level ranges may be constructed. For the example from figure C.1, the χ^2 distribution shown in C.2 may be constructed. This is to be read as "If the true value of δ_{CP} lies at 90° , then the experiment will be able to determine to 3σ that the value lies between $78^\circ - 100^\circ$ ".

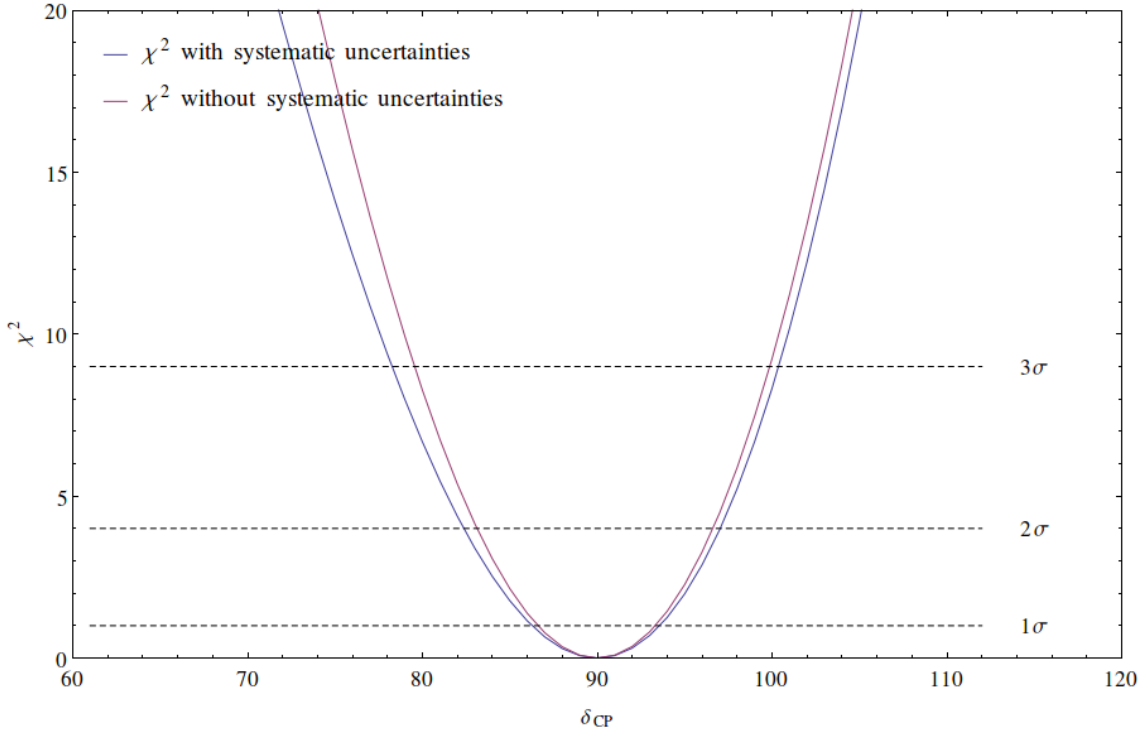


Figure C.2: χ^2 distribution for $\delta_{CP}^{True} = \frac{\pi}{2}$ for both a Neyman's χ^2 , labelled as "without systematic uncertainties", and the full $\Delta\chi^2$. As can be seen, a 3σ allowed region for delta can be constructed between $\delta_{CP} \approx 78^\circ$ and $\delta_{CP} \approx 100^\circ$.

Bibliography

- [1] W. Pauli, Offener brief an die gruppe der radioaktiven bei der gauverins-tagung zu Tübingen, 1930.
- [2] E. Fermi, Il Nuovo Cimento 11 (1934) 1.
- [3] H. Bethe and R. Peierls, Nature 133 (1934) 532.
- [4] F. Reines and C. Cowan, Physical Review 92 (1953) 84.
- [5] K. Kodama et al., Physics Letters B 504 (2001) 218.
- [6] . ALPHI Collaboration et al., Physics Reports 427 (2006) 257.
- [7] C.S. Wu et al., Physical Review 105 (1957) 1413.
- [8] J.N. Bahcall and R. Davis, Science (New York, N.Y.) 191 (1976) 264.
- [9] M. Gonzalez-Garcia, Nuclear Physics B - Proceedings Supplements 81 (2000) 113.
- [10] M. Gell-Mann and A. Pais, Physical Review 97 (1955) 1387.
- [11] Y. Fukuda, T. Hayakawa and E. Ichihara, Physical Review Letters 81 (1998) 1, 9807003v2.
- [12] Q. Ahmad et al., Physical Review Letters 89 (2002) 6, 0204008v2.
- [13] B.T. Cleveland et al., The Astrophysical Journal 496 (1998) 505.
- [14] M.C. Gonzalez-Garcia et al., Journal of High Energy Physics 123 (2012), arXiv:1209.3023v3.
- [15] P. Minkowski and H. Fritsch, Physics Letters B 62 (1976) 72.
- [16] S. Eliezer and A. Swift, Nuclear Physics B 105 (1976) 45.
- [17] S. Bilenky and B. Pontecorvo, Physics Letters B 61 (1976) 2.

- [18] Z. Maki, M. Nakagawa and S. Sakata, Progress of Theoretical ... 28 (1962) 870.
- [19] B. Pontecorvo, Sov. Phys. JETP 26 (1968) 984.
- [20] . Planck Collaboration, arXiv preprint (2014) 1, arXiv:1303.5076v3.
- [21] C. Giunti, C.W. Kim and U.W. Lee, Physical Review D 45 (1992).
- [22] M. Blasone, G. Vitiello and G. Collegato, Journal of Physics A: Mathematical and Theoretical 33 (1995) 1369, 9501263v1.
- [23] C. Giunti, Journal of Physics G: Nuclear and Particle Physics 34 (2007) R93.
- [24] S. Bilenky and C. Giunti, International Journal of Modern Physics A (2001), 0102320v1.
- [25] C. Giunti, C. Kim and U. Lee, Physical Review D 44 (1991) 3635.
- [26] B. Kayser, Physical Review D 24 (1981) 110.
- [27] C. Giunti and C.W. Kim, Fundamentals of neutrino physics and astrophysics (Oxford University Press, 2007).
- [28] C. Giunti, Journal of High Energy Physics 2002 (2002) 17, 0205014v2.
- [29] M. Beuthe, Physics Reports 375 (2003) 105, 0109119v2.
- [30] C. Giunti et al., AIP Conference Proceedings Vol. 1026, pp. 3–19, AIP, 2008, arXiv:0801.0653v1.
- [31] T. Katori, arXiv preprint (2014) 1, arXiv:1206.6915v3.
- [32] H. Nunokawa, S. Parke and R.D. Janeiro, Progress in Particle and Nuclear Physics 60 (2007) 338, arXiv:0710.0554v2.
- [33] K. Asano and H. Minakata, Journal of High Energy Physics 2011 (2011) 22, arXiv:1103.4387v3.
- [34] L. Wolfenstein, Physical Review D 17 (1978) 2369.
- [35] S.P. Mikheyev and A.Y. Smirnov, Il Nuovo Cimento C 9 (1986) 17.
- [36] B. Autin, A. Blondel and J. Ellis, PROSPECTIVE STUDY OF MUON STORAGE RINGS AT CERN 99-02, 1999.
- [37] A. Cervera et al., Nuclear Physics B 579 (2000) 17.

- [38] P. Huber, M. Lindner and W. Winter, Computer Physics Communications 167 (2005) 195, 0407333v1.
- [39] P. Huber et al., Computer Physics Communications 177 (2007) 432, 0701187v2.
- [40] S. Pascoli, Nuclear Physics B 237-238 (2013) 141.
- [41] . LAGUNA-LBNO Collaboration, arXiv preprint (2014), arXiv:1312.6520v3.
- [42] V. Barger, D. Marfatia and K. Whisnant, Physical Review D 65 (2002), 0112119.
- [43] J.L. Hewett et al., Workshop on Fundamental Physics at the Intensity Frontier No. December, p. 229, 2012, 1205.2671.
- [44] S. Rigolin, 1 (2004) 7, 0407009.
- [45] C. Adams, D. Adams and T. Akiri, arXiv preprint (2014), arXiv:1307.7335v3.
- [46] J. Kisiel et al., PoS, pp. 1–4, 2009.
- [47] . Super-Kamiokande Collaboration, Physical Review Letters 81 (1998) 1158, 9805021.
- [48] . Borexino Collaboaration, Nuclear Physics B - Proceedings Supplements 28 (1992) 486.
- [49] . RENO Collaboration, (2010) 126, 1003.1391.
- [50] . Daya Bay Collaboration, ICHEP 2008, p. 4, 2008, 0810.0807.
- [51] L. De Braeckeleer, Nuclear Physics B - Proceedings Supplements 87 (2000) 312.
- [52] R.J. Abrams et al., preprint October (2011), 1112.2853.
- [53] P. Huber, M. Lindner and W. Winter, Nuclear Physics B 645 (2002) 3, 0204352.
- [54] S. Baker and R. Cousins, Nuclear Instruments and Methods in Physics . . . 221 (1984) 437.
- [55] M. Blennow et al., Journal of High Energy Physics 2014 (2014) 28, 1311.1822.
- [56] L. collaboration, preprint October (2012).
- [57] B. Baller et al., Journal of Instrumentation 9 (2014) T05005, arXiv:1307.8166v3.
- [58] P. Coloma et al., Journal of High Energy Physics 2012 (2012) 73, arXiv:1203.5651v2.

- [59] A. Aguilar et al., Physical Review D 64 (2001) 112007, 0104049v3.
- [60] A. Aguilar-Arevalo et al., Physical Review Letters 102 (2009) 101802, arXiv:0812.2243v2.
- [61] G. Mention et al., Physical Review D 83 (2011) 073006, arXiv:1101.2755v4.
- [62] D. Hollander and I. Mocioiu, (2014) 14, 1408.1749.
- [63] P.A. Ballet, Probing leptonic flavour with future long-baseline neutrino oscillation experiments, PhD thesis, Durham University, 2013.
- [64] P. Huber, M. Lindner and W. Winter, (2004) 9, 0407333.
- [65] T. Kikuchi, H. Minakata and S. Uchinami, Journal of High Energy Physics 2009 (2009) 114, arXiv:0809.3312v2.